

A CARBON NANOTUBE MICROELECTRODE ARRAY FOR NEURAL STIMULATION

A DISSERTATION SUBMITTED TO
THE DEPARTMENT OF APPLIED PHYSICS
AND THE COMMITTEE ON GRADUATE STUDIES
OF STANFORD UNIVERSITY
IN PARTIAL FULFILLMENT OF THE REQUIREMENTS
FOR THE DEGREE OF
DOCTOR OF PHILOSOPHY

Ke Wang

June 2006

© Copyright 2006 by Ke Wang
All Rights Reserved

I certify that I have read this dissertation and that, in my opinion, it is fully adequate in scope and quality as a dissertation for the degree of Doctor of Philosophy.

Dr. James S. Harris, Principal Advisor

I certify that I have read this dissertation and that, in my opinion, it is fully adequate in scope and quality as a dissertation for the degree of Doctor of Philosophy.

Dr. Harvey A. Fishman

I certify that I have read this dissertation and that, in my opinion, it is fully adequate in scope and quality as a dissertation for the degree of Doctor of Philosophy.

Dr. Krishna Shenoy

Approved for the University Committee on Graduate Studies:

Abstract

Electrical stimulation of nerve cells is widely employed in neural prostheses (for hearing, vision, and limb movement restoration), clinical therapies (treating Parkinson's disease, dystonia and chronic pain), as well as in basic neuroscience studies. In all these applications, an implanted microelectrode array transmits electrical signals to the neurons and modulates their behavior. These stimulating electrodes need to be biocompatible, stable, micro-scaled, and capable of delivering high current while remaining electrochemically safe.

This work presents a novel neural interface using multi-walled carbon nanotubes (CNT) as microelectrodes. We synthesized self-assembled CNTs by thermal chemical vapor deposition. The CNTs formed pillars of controllable height projecting orthogonally from the surface. Using conventional silicon-based micro-fabrication processes, these CNT ensembles were integrated onto pre-patterned microcircuitry. The geometry and location of the CNT microelectrodes could be precisely defined.

The electrochemical properties of the CNT microelectrode array were characterized by cyclic voltammetry, impedance spectroscopy, and potential transient measurements. Compared to platinum and iridium oxide neural electrodes, these CNT microelectrodes had a wide electrochemical operational window, competitive charge injection limit, and operated capacitively without faradic reactions. These properties have become increasingly important, as applications in the central nervous system require a significant reduction in electrode size. Different surface modification techniques, such as thermal

oxidation and non-covalent binding, were investigated to functionalize the CNT electrodes and the active interfacial area was considerably increased.

The biocompatibility of CNTs was assessed by *in vitro* neuronal culture. Retinal ganglion cells and hippocampal neurons were cultured on CNT substrates, and showed comparable viability and neurite outgrowth to cultures on Petri dish controls. *In vitro* stimulation of primary neurons with the CNT microelectrode array was demonstrated for the first time. Neurons could be repeatedly stimulated, indicating good cell excitability and electrode condition.

In conclusion, a prototype CNT microelectrode array has been developed. Several critical aspects of CNTs as neural stimulating electrodes were investigated. The advantageous electrochemical, mechanical, and chemical properties of CNTs suggest that they are capable of providing a safer and more efficacious solution for neural stimulation.

Acknowledgments

It has been a long, but fortunately not lone journey towards the degree of Ph.D. I feel grateful to have known and worked with so many wonderful people, who helped me one way or another during all these years.

I would first like to thank my advisor, Professor James Harris, a.k.a. “Coach”. He gave me plenty of room to grow freely, while he was always there to provide guidance and help whenever I needed. From him, I learned how to think and plan independently, how to handle stressful situations, as well as how to maintain a balanced life and personality in graduate school. I believe all of these skills will continue to be tremendously helpful after my graduation from Stanford.

Dr. Harvey Fishman initiated and co-advised this project. I am deeply impressed by his enthusiasm, energy, creativity and broad range of knowledge. I truly appreciate that Harvey gave me this great opportunity to work on this very interesting project, and continued supervising the progress even after he had moved on with his career.

I benefited greatly from Professor Hongjie Dai’s profound knowledge of carbon nanotubes. Over the past years, Hongjie has always been willing to discuss the experimental results and answer my questions. His advice on the nanotube part was invaluable for this project.

I would like to thank Professors Mark Blumenkranz, Michael Marmor and Daniel Palanker in the Department of Ophthalmology, for their guidance and support. The

discussions with Daniel on various aspects of the project have been exceptionally helpful and inspiring.

I would like to thank Professor Krishna Shenoy for serving on my reading committee. I will never forget that he came to my oral defense only hours after his new baby was born, and I am truly grateful. I also thank Professor Stephen Smith and Professor Mark Schnitzer for being on my oral defense committee.

It would be impossible to list the entire Harris group (over 50 names) here. However, I do enjoy the friendship with every group member. In particular, I learnt a lot from Evan Thrush and Ofer Levi, with whom I worked for the first two years on a fluorescence sensor project.

It has been a pleasant experience working in the Ophthalmology Department, with a multi-disciplinary group with highly diverse background: Neville Mehenti, Christina Lee, Mark Peterman, Jaan Noolandi, Roopa Dalal, Boris Stanzel, Philip Huie, Alexander Vankov, Alexander Butterwick, Ted Leng, Fanni Molnar, and many others. I would especially like to thank Neville for his help with the cellular experiments.

Due to the interdisciplinary nature of this project, I had the privilege to work in many different labs, “outsourcing” for both equipments and expertise. I synthesized the nanotubes in Dai lab, and I greatly appreciate all the help I have received, especially from Yiming Li, Nadine Wong Shi Kam, Guangyu Zhang, and David Mann. Professor Rainer Fasching taught me electrochemistry, helped me with the measurements, and discussed the results with me. People in McIntyre group and Chidsey group also kindly allowed me to perform some of the electrochemical measurements using their facilities.

I spent many long days and long nights in the Stanford Nanofabrication Facility (SNF). The staff has been exceptionally friendly, lively, responsive and ready to help; the lab users were always willing to share their knowledge, experience, as well as the lab space. It has been a real pleasure to work in this large facility full of smiling users!

I would also like to thank Paula Perron, Claire Nicholas, Gail Chun-Creech, and Steve Unyi, for soothing away many anxieties in my graduate life. They have helped tremendously in almost every aspect, from pay checks to organizing the defense committee.

I feel fortunate to have the friendship of some wonderful people during these years in the bay area, where people often move in and out too frequently to really know each other. The moments with friends made my American experience much more balanced and colorful.

This is a fulfillment of a multi-year dream of my parents. I would like to dedicate this dissertation to them, to thank for all the support and trust they have put in me. I should also thank my grandmother. Every time after she asked me when my “magic” chip would be available on the market, I felt greatly motivated to keep on working.

And finally, my husband Luigi. We met each other in Harris group during our first year (another reason to thank Coach, for taking both of us!). We walked through the entire long graduate life together, from the qualifying exam to the commencement. Looking back, I can not imagine how these years could have been without him. He is the most precious gift I have got from Stanford, and will take along with me when I leave.

This project was generously funded by the Stanford Ophthalmology Departmental Endowment. The experiments were also partially supported by the Stanford Center for Integrated Systems research grant, and by VISX, Inc.

Table of Contents

Abstract.....	v
Acknowledgments.....	vii
Table of Contents.....	xi
List of Tables.....	xv
List of Figures.....	xvii
Chapter 1 Introduction.....	1
1.1 Neural Interface.....	1
1.2 Retinal Prostheses: an Example.....	2
1.3 Stimulating Neural Electrodes.....	5
1.3.1 General Considerations.....	5
1.3.2 Current Neural Electrodes.....	7
1.4 Carbon Nanotubes.....	8
1.5 Organization of the Thesis.....	9
Chapter 2 Microelectrode Design and Fabrication.....	11
2.1 Design of the CNT Microelectrode Array.....	11
2.1.1 Basic Scheme.....	11
2.1.2 Material Selection.....	14
2.1.2.1 Substrate.....	15
2.1.2.2 Insulating Layer.....	15
2.1.2.3 Interconnects.....	16

2.1.2.4	Contact Pads	18
2.1.3	Layout	18
2.2	Carbon Nanotube Synthesis	20
2.2.1	Arc-Discharge and Laser Ablation.....	20
2.2.2	Chemical Vapor Deposition	21
2.2.3	Synthesis and Results.....	22
2.2.4	X-ray Photoelectron Spectroscopy (XPS)	27
2.3	Device Fabrication	30
2.3.1	Processing	30
2.3.1.1	Poly-Silicon Deposition and Patterning.....	31
2.3.1.2	Passivation Deposition and Patterning	32
2.3.1.3	Metal Deposition and Patterning.....	33
2.3.2	Packaging.....	34
2.4	Parasitics: Calculation and Measurement.....	36
2.4.1	Passivation Capacitance.....	37
2.4.2	Crosstalk Capacitance	38
2.4.3	Interconnect Resistance	39
2.4.4	CNT resistance	40
2.5	Summary.....	41
Chapter 3	Electrochemistry of the CNT Electrodes	43
3.1	The Electrode-Electrolyte Interface	43
3.1.1	Double-Layer Capacitance	45
3.1.1.1	The Gouy-Chapman-Stern (GCS) Model.....	45
3.1.1.2	Estimate of Double-Layer Capacitance	48
3.1.2	Charge Transfer and Warburg Impedance.....	49
3.1.3	Spreading Resistance	51
3.2	Electrochemical Guidelines for Neural Stimulation	52
3.3	Cyclic Voltammetry	54
3.4	Surface Modification	57
3.4.1	Thermal Oxidation	59

3.4.2	Non-covalent Functionalization.....	60
3.5	Impedance Spectroscopy.....	64
3.5.1	Equivalent Circuit.....	65
3.5.2	Effect of Surface Modification	66
3.5.3	Data Analysis.....	67
3.6	Potential Transient Measurement	70
3.7	Summary	74
Chapter 4. In Vitro Neuronal Culture on CNT		75
4.1	Overview of Adherent Neuronal Culture.....	75
4.2	Cell Preparation	77
4.2.1.1	Retinal Ganglion Cell.....	78
4.2.1.2	Hippocampal Neuron	79
4.3	Substrate Preparation	80
4.3.1.1	Sterilization.....	80
4.3.1.2	Surface modification	81
4.4	Results.....	83
4.4.1.1	Live/Dead Stain	83
4.4.1.2	SEM Images.....	88
4.4.1.3	Statistical Results.....	89
4.5	Summary	92
Chapter 5. Neural Stimulation		93
5.1	Neural Stimulation Theory.....	93
5.1.1	Ionic basis.....	94
5.1.1.1	Resting Potential.....	95
5.1.1.2	Action Potential	96
5.1.2	Extracellular stimulation	98
5.1.2.1	Cell Response in an Electrical Field.....	98
5.1.2.2	Field Distribution of Cylindrical Electrodes.....	102
5.2	Detection of the Action Potential	105

5.3	Experimental Methods.....	107
5.3.1	Device treatment.....	107
5.3.2	Cell Culture on the Device	108
5.3.3	Fluorescent Dye Loading.....	109
5.3.4	Microscopy and imaging	110
5.4	Stimulation Results.....	112
5.4.1	Chemical Stimulation.....	112
5.4.2	Electrical Stimulation.....	114
5.5	Summary.....	120
Chapter 6 Conclusions and Future Perspectives.....		121
Appendix A. Fluorescein Tagging.....		127
Appendix B. RGC Panning Protocol		128
Appendix C. Preparation of Rat Hippocampal Neurons.....		136
Appendix D. Loading Fluorescent Dyes.....		138
Appendix E. Preparing Cell Culture Samples for SEM.....		140
Appendix F. Integrating CNTs with PDMS		142
References		145

List of Tables

Table 2-1 Device surface composition after CNT growth cycle.....	30
Table 2-2 Values of the circuit parasitics.....	37
Table 3-1 Characteristic Thickness of the Diffuse Layer	46
Table 3-2 Electrochemical properties of several neural electrode materials	73
Table 5-1 Ionic concentrations in mammalian skeletal muscle.....	95
Table 5-2 Typical values of the physiological parameters of a neuron	101

List of Figures

Figure 1.1 Structure of the human eye and the retina.....	3
Figure 1.2 Conceptual drawing of an example of retinal prostheses.....	4
Figure 1.3 Limitations on the stimulation current.....	6
Figure 1.4 Atomic structures of carbon nanotubes.....	8
Figure 2.1 Schematic drawing of a CNT microelectrode array.....	12
Figure 2.2 Planar implants versus protruding implants in the retina.....	13
Figure 2.3 Circuit elements of a microelectrode array in conductive solution.....	14
Figure 2.4 Cross-sectional structure of a CNT electrode.....	15
Figure 2.5 SEM images of the device surface after thermal cycles.....	16
Figure 2.6 Leakage current through the insulation layer.....	17
Figure 2.7 Layout of a 6×6 microelectrode array.....	19
Figure 2.8 Mask design for the electrode.....	20
Figure 2.9 Illustration of CVD nanotube growth (base mode).....	22
Figure 2.10 Schematic drawing of a catalytic thermal CVD system.....	23
Figure 2.11 SEM images of MWCNTs on silicon substrates.....	24
Figure 2.12 Growth rate of CNT pillars.....	25
Figure 2.13 Temperature dependence of CNT growth.....	26
Figure 2.14 Substrate selectivity of CNT growth.....	27
Figure 2.15 XPS analysis of as-grown CNT surface.....	28
Figure 2.16 XPS analysis of quartz surface after growth.....	29
Figure 2.17 Fabrication process of the CNT microelectrode array.....	31
Figure 2.18 SEM images of CNT microelectrodes.....	34

Figure 2.19 A CNT microelectrode array with bonded chamber.	35
Figure 2.20 Two-part connector.	36
Figure 2.21 Measurement of passivation capacitance.	38
Figure 2.22 Test structure for interconnect resistance measurement.....	39
Figure 2.23 A trapezoid strip of interconnect.....	40
Figure 3.1 The electrode-electrolyte interface.	44
Figure 3.2 Double-layer capacitance based on the GCS model.....	48
Figure 3.3 Equivalent circuit model of the electrode-electrolyte interface.	52
Figure 3.4 Basic principle of cyclic voltammetry.....	54
Figure 3.5 Cyclic voltammogram of a CNT electrode in PBS..	55
Figure 3.6 Cyclic voltammogram of platinum and activated iridium oxide.....	56
Figure 3.7 Thermal treatment of CNTs..	60
Figure 3.8 Visual evaluation of the hydrophilicity of the CNT pillars..	61
Figure 3.9 Binding PEG-PL conjugates to CNT.....	62
Figure 3.10 Confocal images of CNTs with FITC-labelled PEG-PL.....	63
Figure 3.11 CNT double-layer capacitance measured from cyclic voltammogram.	64
Figure 3.12 EIS of a CNT electrode..	66
Figure 3.13 Bode plot: effect of surface treatments.....	67
Figure 3.14 Capacitance of untreated CNT electrodes of different sizes.	68
Figure 3.15 Capacitance of thermally oxidized CNT electrodes of different sizes.	69
Figure 3.16 The sidewall and the top of a CNT pillar (SEM).....	69
Figure 3.17 Spreading resistance for electrodes of different sizes.	70
Figure 3.18 Potential transient of a CNT electrode	71
Figure 3.19 Charge injection limit and durability.....	72
Figure 4.1 NG108-15 cells cultured on Petri dishes..	78
Figure 4.2 CNT substrates for in vitro cell culture.	80
Figure 4.3 Confocal images of CNT pillars with FITC-labeled molecules.....	82
Figure 4.4 The absorption and emission spectra of LIVE/DEAD dyes..	84

Figure 4.5 Live/dead stain of hippocampal neurons on CNT substrates with different sterilization..	85
Figure 4.6 Live/dead stain of hippocampal neurons on CNT substrates with different coating.	86
Figure 4.7 Continual growth of retinal ganglion cells on CNT substrates	87
Figure 4.8 RGCs cultured on a silicon substrate with CNT pillar arrays.	88
Figure 4.9 SEM images of RGC cultures on CNT substrates.	89
Figure 4.10 Statistical results of hippocampal neuronal culture on CNT mats.	91
Figure 5.1 Schematic of an action potential showing different phases.	96
Figure 5.2 Cell polarization under an extracellular electrical field.	99
Figure 5.3 Simulation of the electrical field of cylindrical electrodes.	104
Figure 5.4 Hippocampal neurons cultured on a CNT microelectrode array.	109
Figure 5.5 Experimental setup for cell stimulation and detection.	111
Figure 5.6 The spectra of Fluo-4 and the filter set.	112
Figure 5.7 Chemical stimulation of hippocampal cells.	113
Figure 5.8 Hippocampal cell stimulation with CNT microelectrode arrays.	115
Figure 5.9 Repeated cell stimulation with a CNT electrode.	116
Figure 5.10 Discharge of a CNT electrode.	117
Figure 5.11 Strength-duration curve of the stimulation threshold	118
Figure 6.1 Schematic drawing of a CNT microelectrode array with sidewall insulation.	123
Figure 6.2 SEM images of CNTs transferred onto a thin PDMS membrane.	125
Figure F.1 PDMS spin curve	143

Chapter 1

Introduction

1.1 Neural Interface

Electrical stimulation and recording of nerve cells have been used in basic neuroscience studies for over a century. The concept of applications in neural prostheses and clinical therapies has also been developed for decades [1], but has only recently come into realization, facilitated by sophisticated modern microfabrication technology and advances in material sciences. For example, cardiac pacemakers are already widely used to improve the life of millions of patients. Some other applications (many of which are still under development) are: cochlear implants, to recover hearing [2]; visual prostheses, to restore vision [3]; neuromuscular prostheses, to reanimate paralyzed limbs in patients who survived from stroke and spinal cord injuries [4]; and deep brain stimulation, which has been found very useful in treating the Parkinson's disease, essential tremor, epilepsy, dystonia, depression, as well as chronic pain [5]. In all these applications, an essential part in common is the neural interface (or sometimes called the brain-computer interface), where an implantable microelectrode array communicates between the electronics and the nerve cells. The microelectrodes either transmit electrical signals to the neurons and modulate their behavior, or sense neural signals and use them to control an electronic device or even other nerve cells. In the following paragraphs, retinal prostheses will be used as an example to explain the concept of neuroprosthetics and the role of the microelectrode array.

1.2 Retinal Prostheses: an Example

The structure of the human eye is illustrated in Figure 1.1a. Light rays are first focused by the cornea and the lens, and then pass the vitreous humour before finally reaching the retina at the back of the eyeball. The retina is a delicate membrane, less than 0.5 mm thick. Yet it has a highly complex structure consisting of ten distinct cell layers. These include three layers of cell bodies (Figure 1.1b): (i) the *outer nuclear layer* (cell bodies of photoreceptors, i.e., rods and cones); (ii) the *inner nuclear layer* (bipolar cells, amacrine cells, and horizontal cells); and (iii) the ganglion cell layer. The synapses between these cell types are made in the outer and inner plexiform layers. Counter-intuitively, light needs to pass through all the other cell layers (which are transparent) before being absorbed by the photosensitive molecules in the photoreceptors. The photoreceptors transduce light into electrical signals via a cascade of biochemical reactions. The signals are passed on to the cells in the inner nuclear layer, and then on to the ganglion cells. The axons of the ganglion cells form the optic nerve, and carry the signals to the visual cortex where vision is formed. There are over one hundred million photoreceptors in a human retina, but only about one million ganglion cells. The retina is thus more than an optoelectronic transducer. It is also a signal processor, with a compression ratio of 100:1.

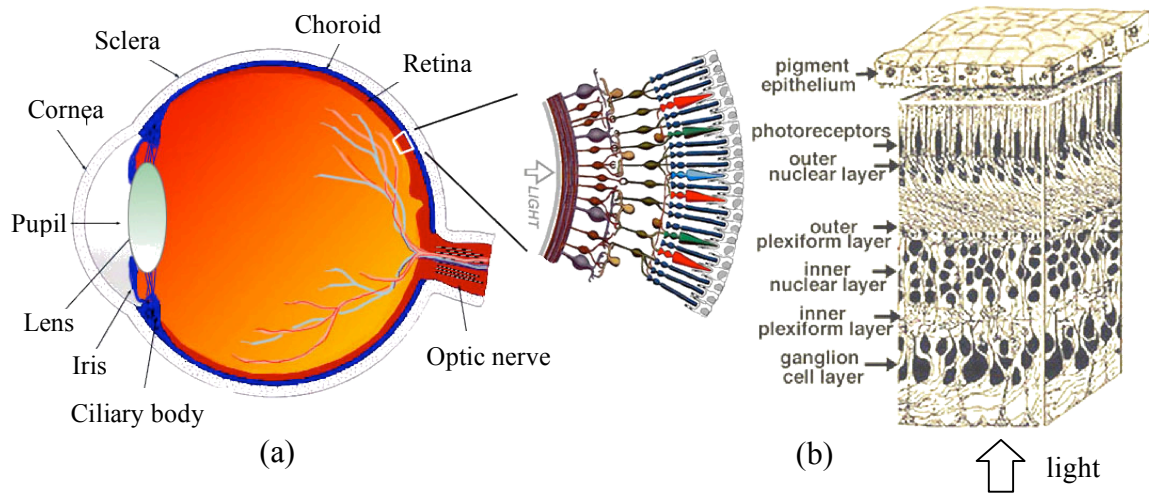


Figure 1.1 Structure of the human eye and the retina. (a) The vertical section through an adult human eye, with a schematic enlargement of the basic structure of the retina. (b) A 3D block of a portion of the retina, showing the nerve cell body layers and the synapses layers. *Images adapted from Webvision, by Kolb, Fernandez, and Nelson.*

More than 50% of all blindness is caused by retinal diseases. Among them, age-related macular degeneration (AMD) and retinitis pigmentosa (RP) are two leading causes of blindness in the United States. There are currently no known treatments for these diseases. In both types of patients, the photoreceptors in either the central retina (AMD patients) or the peripheral retina (RP patients) progressively degenerate and are finally lost. However, it was found that up to 70-90% of the rest of the visual pathway remained intact [6]. Pioneering experiments have demonstrated that by providing the visual cortex with artificial electrical stimuli, the subject could have a sensation of light spots, called phosphenes [7, 8]. These discoveries inspired the development of retinal prostheses, aiming at the restoration of vision in these patients by recovering the lost input to the retina.

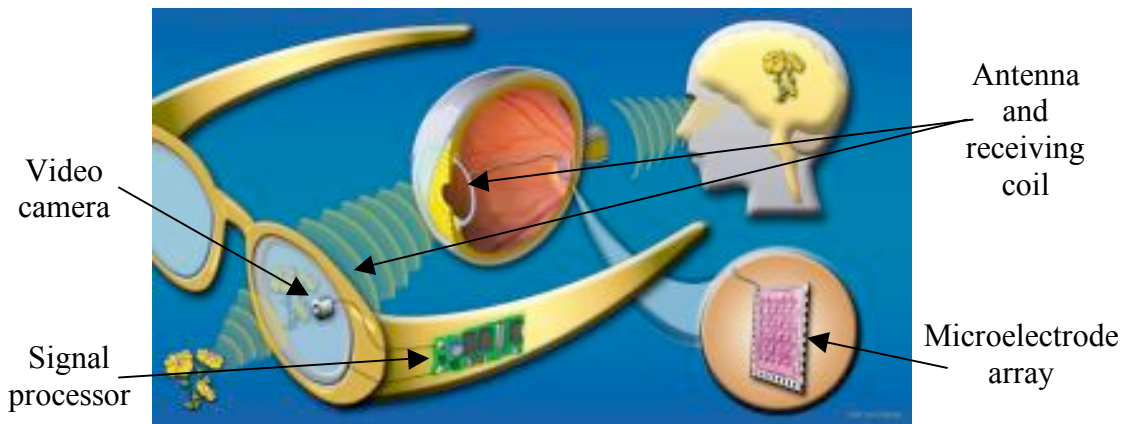


Figure 1.2 Conceptual drawing of an example of retinal prostheses. The system has an external part (video camera, signal processor and antenna), and an implanted part (receiving coil, microelectrode array). *Image adapted from the website of Department of Energy.*

The design of retinal prostheses varies, but the basic concept can be explained by Figure 1.2. The patient wears a special pair of glasses, which incorporate a miniature video camera embedded in the lens, plus image processors in the frame and an antenna. Images are captured by the camera, transduced into patterned electrical signals, and then transmitted through radio frequency to a receiving coil implanted in the eye. The coil is connected with a thin wire to a microelectrode array implant on the retina (either subretinally, i.e., on the photoreceptor side; or epiretinally, i.e., on the ganglion cell side). The microelectrode array stimulates the remaining retinal neurons with electrical pulses, just like the photoreceptors stimulate the cells in the inner nuclear layer. With the input recovered and the rest of the visual pathway still functioning, it is anticipated that visual perception can be restored at the cortex.

Alternatively, the interfacial microelectrode array can also be implanted on the visual cortex. The advantage of cortical implants is that a larger range of blind patients (not only those with retinal diseases) can benefit. Retinal implants rely more on the

preservation of the visual pathway, but consequently can maximize the use of natural signal processing in the nervous system, which is a neuroscience subject still far from being fully understood.

1.3 Stimulating Neural Electrodes

An essential part of the retinal prosthetic system, as well as other neuroprosthetics, is the implanted microelectrode array. To date, building a stable, biocompatible microelectrode array which is capable of long term safe stimulation is still one of the most challenging problems. General considerations in the design are discussed below. The pros and cons of current neural electrode materials are also overviewed.

1.3.1 General Considerations

The stimulating neural electrodes need to be both efficacious and safe. For efficacy, the electrode must be able to deliver enough charge to exceed the stimulation threshold of nerve cells. Furthermore, many applications require high-resolution stimulation, in which the electrodes need to be small, densely packed, and able to produce localized excitation. For safety, the microelectrode must not cause adverse effects to the tissue during prolonged implantation and stimulation. The major safety issues are: (i) Biocompatibility. The materials used in the implanted array should not be cytotoxic, nor should they cause extensive foreign body or immune response; (ii) Stability. The chemical, electrical and mechanical properties of the material should be stable *in vivo* during the implanted period, which could last decades for chronic human body implants; (iii) Mechanical safety. The implant needs to have enough mechanical flexibility to avoid causing damage from small relative movements between the device and the tissue; (iv) Electrochemical safety. The stimulation current should not cause corrosion of the electrode, nor should it generate reaction products intolerable to the tissue.

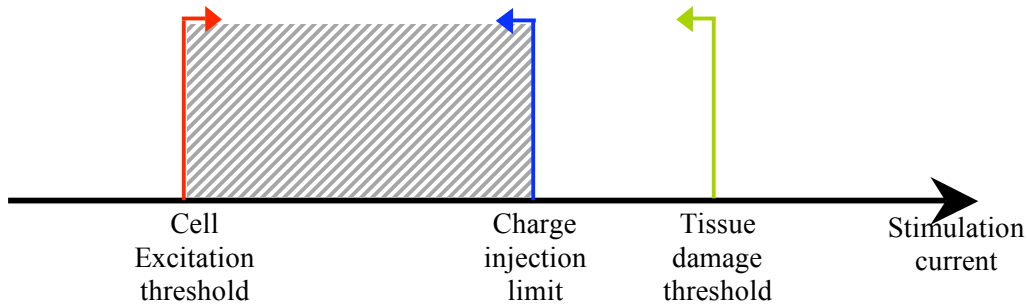


Figure 1.3 Limitations on the stimulation current. The current (density) needs to be higher than cell excitation limit, but should not exceed the electrode charge injection limit or tissue damage threshold, whichever is lower. Shaded region indicates the window of the current that can be used in neural stimulation.

In general, efficacy requires a high stimulation current, while safety considerations need to keep the current low. The limitations are illustrated in Figure 1.3. The excitation threshold is the minimum current needed to generate proper response in the cell and convey the signal. The required current is dependent on the cell type, cell size, the distance between the cell and the electrode, as well as stimulation protocols. The tissue damage threshold is the maximum current that can be used before causing any neural injury. It is also a variable of stimulation protocols [9]. A third constraint is the charge injection limit of the electrode. It is defined as the maximum amount of charge an electrode can deliver before the onset of “unsafe” electrochemical reactions or electrode breakdown. The charge injection limit is determined by the structure and the material of the electrode. It is also proportional to the size of the electrode.

To be both efficacious and safe, the stimulation current must be higher than the cell excitation threshold, while it must not exceed the tissue damage threshold or the charge injection limit, whichever is lower. Obviously, the design of a neural interface should attempt to lower the excitation threshold (usually by reducing the electrode-cell distance), and increase the charge injection limit (by developing better electrodes), in order to

widen the working window. Although the tissue damage threshold is generally less flexible, it can still be adjusted by optimizing the stimulation protocol.

The charge injection ability has become a limiting factor in sophisticated applications such as retinal prostheses, in which a significant reduction in the electrode size is required. Auditory prostheses have already been realized and used in patients, since only 8 to 24 electrodes are required for functional hearing restoration. Each electrode is several hundred micrometers in size and works at a low current density. However, visual information is parallel and far more complex. Simulations have shown that at least 1,000 pixels are required to generate a recognizable image. The physical size of a retinal implant is also much more constrained. The human macular region is only 3 mm across (in diameter). So a retinal prosthesis requires much smaller ($\sim 10 \mu\text{m}$) and densely packed electrodes, setting a demand for much higher charge injection abilities.

1.3.2 Current Neural Electrodes

A variety of metals and metal alloys have been fabricated into electrodes for neural stimulation. Noble metals, such as platinum have a long history as neural electrodes. However, the charge injection ability of bare platinum is low (100-300 $\mu\text{C}/\text{cm}^2$ of geometrical area) [10], hence only large electrodes with low current density can be used safely. This has greatly limited the use of platinum, as well as many other metal electrodes in the central nervous system, where small electrodes and high currents are required. Activated iridium oxide offers a significant improvement in charge injection ability (2-3 mC/cm^2 geom.) with a reversible faradic reaction ($\text{Ir}^{3+} \rightleftharpoons \text{Ir}^{4+} + \text{e}^-$) [11], therefore it has been one of the most popular neural electrode materials. Yet it has been reported that activated iridium oxide suffers delamination under high current pulsing, and deposits particles into the surrounding tissue [12]. Capacitor electrodes that operate more safely by avoiding harmful electrochemical effects have also been developed based on tantalum oxide, titanium oxide, [13] or silicon transistors [14]. Nevertheless, because of

the low capacitance, their charge injection abilities (before electrode breakdown) were not comparable to iridium oxide.

1.4 Carbon Nanotubes

Carbon nanotubes (CNT) were first discovered in early 1990's [15, 16]. A single-walled CNT (SWCNT) can be viewed as a graphite sheet wrapped seamlessly into a cylinder. The diameter is less than ten nanometers. Multi-walled CNTs (MWCNT) consist of several concentric cylindrical layers, with an interlayer distance of 0.34 nm. MWCNTs are usually 30 to 50 nm in diameter. (Figure 1.4)

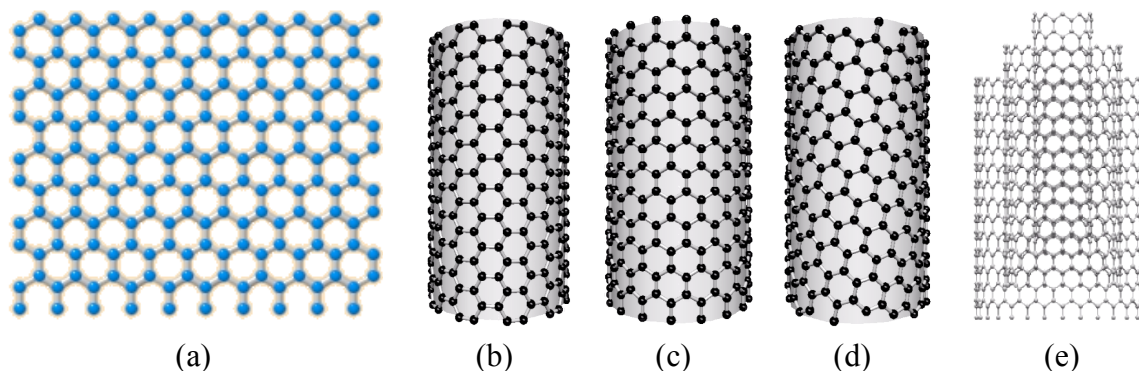


Figure 1.4 Atomic structures of carbon nanotubes. CNTs are graphene sheets (a) rolled into cylinders. (b)-(d): examples of single-walled NTs with different helicity. (b): armchair, (c): zig-zag, (d): chiral. (e): a multi-walled CNT. *Source of images: Ahwahnee Technology.*

We were motivated to study the possibility of using CNTs for neural stimulation because of their intriguing mechanical, chemical and electrochemical properties. Taking advantage of these properties, CNTs have already been used in a variety of applications, such as composite materials, probes and fuel cells. CNTs are among the strongest known molecular materials. Their Young's modulus exceeds 1Tpa [17], about five times stronger than steel. Yet CNTs are flexible: both simulations and experiments show that they can be bent and twisted into large angles without breaking [18, 19]. This

combination of strength and flexibility is highly desirable in neural prostheses. CNTs inherently have very large surface area, and are chemically inert. Both properties are electrochemically advantageous for neural stimulation.

We chose to use MWCNT as the material for the neural electrode for two reasons. First of all, the electronic properties of a SWCNT are very sensitive to its atomic structure. Depending on the helicity (i.e., rolling angle, see Figure 1.4) and diameter, a SWCNT can be either metallic, or semiconductive. Currently, there is still relatively little control of these parameters in CNT synthesis. The bandgap of a nanotube is inversely proportional to the diameter. Because of their large diameters, MWCNTs are predominantly electrically conductive. The second reason is also related to the size of the nanotubes. Although undesired for this application, uptake of SWCNTs by the cells is being explored to decide whether SWCNTs can be used as transporters in drug delivery [20]. On the other hand, MWCNTs are much larger than the cell membrane channels, and are much less likely to be transported into the cells. To our knowledge, there is still no report of any membrane permeability of MWCNTs.

1.5 Organization of the Thesis

This thesis presents the design, fabrication and testing of a CNT microelectrode array for neural stimulation. We believe it has the potential to offer a safer and more efficacious solution for applications such as the retinal prostheses. Some necessary background of this work has been provided in the first chapter. We start with a description of the scenario and basic concepts of neural prostheses. Then general guidelines for designing stimulating neural electrodes are explained, followed by a brief review of currently used neural electrodes. Finally, the rationales for choosing CNT, especially MWCNT, are addressed.

In chapter 2, the design and fabrication process of the CNT microelectrode array, including the synthesis of CNTs, will be described in detail. Some most basic properties of the device, such as the circuit parasitics, are closely related to the design and

fabrication process. Therefore the testing of these features will also be included in this chapter.

Electrochemical properties and biocompatibility are the most important issues of any neural electrode. These two aspects of the CNT microelectrode array are discussed in chapter 3 and chapter 4, respectively. Chapter 3 will start with the theory of electrode-electrolyte interaction with a focus on applicability to this device. Then characterization of the electrochemical properties of CNT microelectrodes will be presented. Chapter 4 is devoted to the biocompatibility of CNT, which was assessed by in vitro cell culture on CNT substrates. The growth of retinal ganglion cells and hippocampal neurons on CNT will be compared to cultures on Petri dish controls.

Chapter 5 reports the results of neural stimulation with the CNT microelectrode array. It begins with the basic theory of extracellular neural stimulation, followed by a description of experimental methods. Then continuous stimulation of hippocampal neurons with the CNT microelectrodes will be demonstrated.

The thesis will conclude with a summary of the different aspects of CNTs as microelectrodes for neural stimulation. A perspective for the future directions will also be discussed, along with some preliminary experimental results.

Chapter 2

Microelectrode Design and Fabrication

Many aspects need to be considered when developing an interface between the electronics and living nerve cells. All the materials must be biocompatible. The device needs to perform electrical functions in a physiological aqueous environment, and be resistant to a variety of physiochemical processes, such as corrosion and encapsulation. To simplify the situation, the CNT microelectrode array was designed for in vitro experiments, in which the requirements for the overall chip size, mechanical durability and packaging are less rigorous. The goal is to understand the basic properties (such as electrochemistry and biocompatibility) of the device through in vitro tests, and decide the feasibility of using CNT as a new neural electrode material.

2.1 Design of the CNT Microelectrode Array

The design of the CNT microelectrode array follows the general guidelines described in Chapter 1. In addition, practical issues also need to be taken into account. The final design is a compromise between device performance, and the restrictions of microfabrication capability, integration with CNT, packaging, as well as testing facilities.

2.1.1 Basic Scheme

A schematic drawing of the basic design of a CNT microelectrode array is shown in Figure 2.1. Each electrode is an ensemble of millions of multi-walled CNTs, which form a pillar protruding orthogonally from the substrate. The CNT pillars are integrated onto a

substrate with pre-patterned microcircuitry. Each pillar is individually electrically addressable. Since the chip will be immersed in a conductive solution (such as the body fluid), the entire chip is embedded in insulating layers, leaving only the CNT electrodes exposed for cell stimulation, and contact pads exposed for connection to external units.

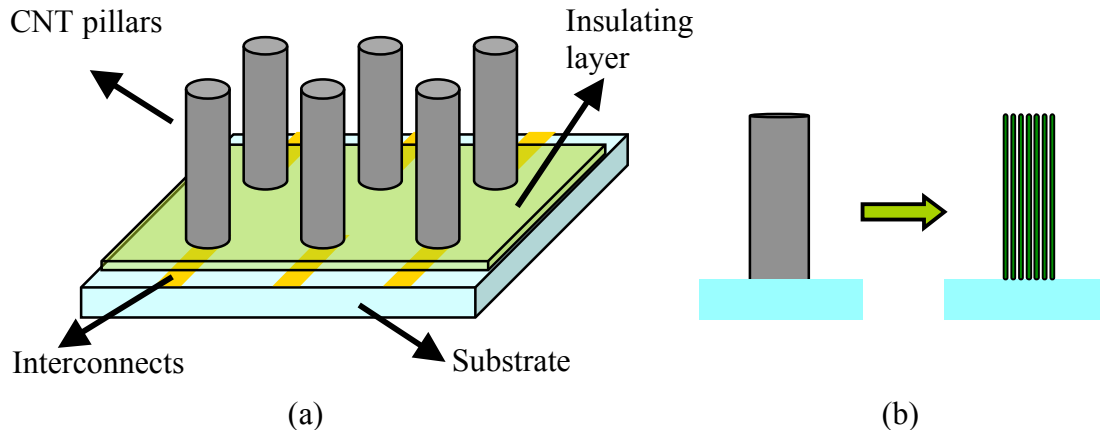


Figure 2.1 Schematic drawing of a CNT microelectrode array. (a) A 3D view of the chip showing the four main components: the substrate, the embedded leads that connect each electrode to a contact pad, the top insulation that isolates the circuit from conductive solutions, and the CNT pillar electrodes. (b): A side view illustrating that each electrode is actually an ensemble of millions of vertically aligned MWCNTs.

The protruding geometry is advantageous in layered tissues, such as the retina and the cortex. This can be explained still using the retina as an example. There are typically two surgically accessible locations for a retinal implant [21]: either on the ganglion cell side of a retina (called *epi-retinal*), next to the inner limiting membrane; or alternatively, inserted into the photoreceptor side (called *sub-retinal*). In both cases, a planar implant is typically placed about a hundred micrometers or farther from the target neurons (bipolar or ganglion cells) (Figure 2.2a). The large distance between the electrode and the cells requires a higher current for excitation. The high current risks causing injury to tissue adjacent to the electrode, as well as forcing an increase in the electrode size in order to stay electrochemically safe. The high current also requires a larger distance between

neighboring electrodes, to avoid cross-talk from the overlapping of their electrical field. In comparison, protruding electrodes can be inserted into the tissue, or nerve cells can grow conformally into the 3D device [22], achieving better proximity between the electrodes and the targets (Figure 2.2b). Proximity is the key for safer and more efficacious neural stimulation because less current is required [23]. This allows the use of smaller electrodes at higher density, localizes the stimulation, reduces tissue injury, as well as lowers power consumption and heat dissipation.

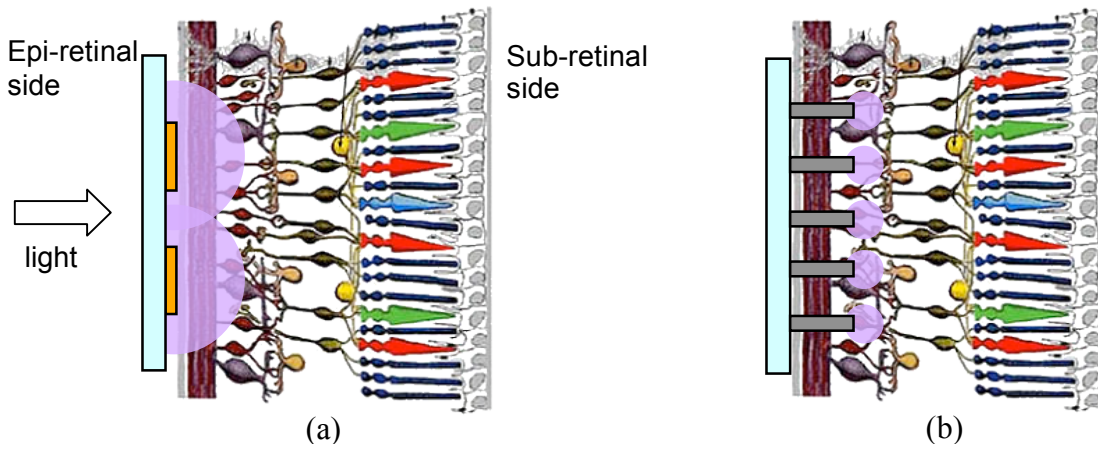


Figure 2.2 Planar implants versus protruding implants in the retina. (a) Planar implants require higher current and larger electrodes. The field (represented by the semi-circles) of neighboring electrodes overlaps. (b) Much smaller electrodes can be used in a protruding geometry, with more localized field distribution.

The basic circuit of a microelectrode array in electrolyte is depicted in Figure 2.3. Z^* is the impedance at the electrode-electrolyte interface. It will be discussed in great detail in chapter 3. R_i is the resistance of the interconnects and R_e is the resistance of CNTs. The parasitics include the capacitance between the interconnect and the electrolyte (C_p), the capacitance between neighboring interconnect traces (C_c), and the capacitance between the interconnects and the substrate (C_s). A quantitative description of these parasitics will be given in Section 2.4.

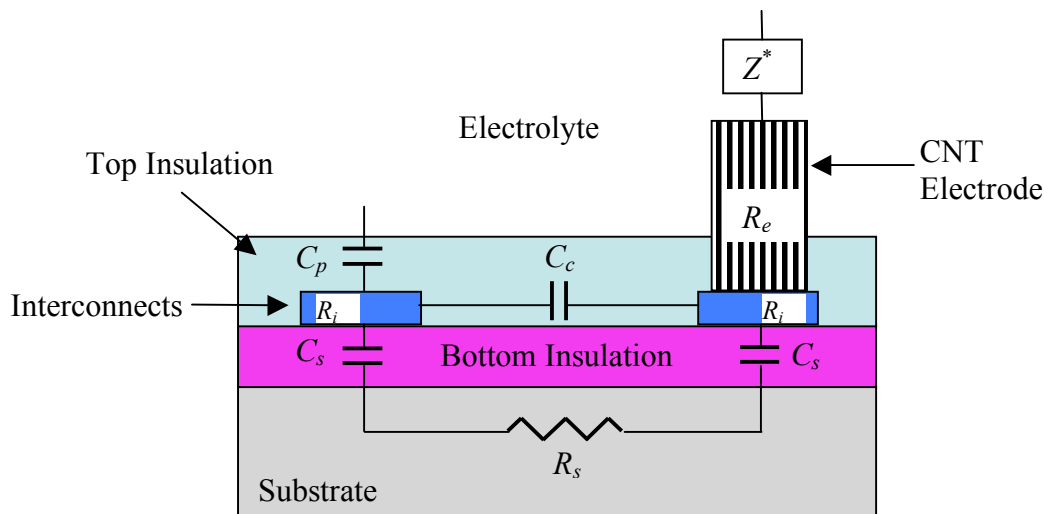


Figure 2.3 Circuit elements of a microelectrode array in conductive solution.

2.1.2 Material Selection

There are three major concerns regarding the selection of materials for this microelectrode array. First of all, the materials need to be thermally stable, since the carbon nanotube synthesis requires very high temperature (700°C, see Section 2.2.3 for more details). Second, they need to be biocompatible. They should not have records of being cytotoxic or causing immune response in vivo. Finally, the undesired effects of circuit parasitics should be minimized. A cross-sectional schematic of the device structure (not to scale) is illustrated in Figure 2.4.

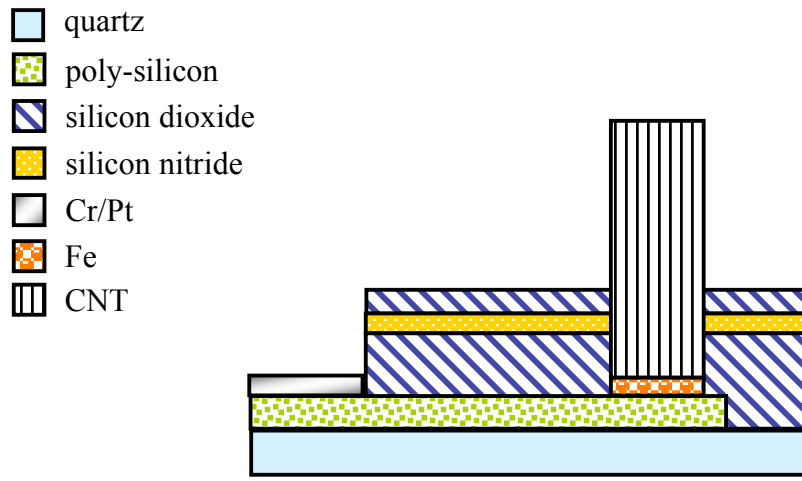


Figure 2.4 Schematic of the cross section of a CNT electrode (not to scale). Conductive layer: 5000Å of phosphate doped poly silicon; insulation layers: 2µm of silicon dioxide, 1000Å of silicon nitride, and 1500Å of silicon dioxide; catalyst layer: 20Å of iron; contact pads: 60Å of chromium and 500Å of platinum.

2.1.2.1 Substrate

Quartz is used as the substrate for the following reasons: (i) It is optically transparent, allowing the use of inverted microscopy in cell experiments. (ii) It has excellent thermal stability. (iii) It is electrically insulating, thus eliminating some parasitic circuit elements which would have resulted from a silicon substrate, such as C_s . However, the device can also be fabricated on silicon substrates. The process is almost identical for silicon, except that an additional oxide needs to be deposited as bottom insulation.

2.1.2.2 Insulating Layer

An oxide-nitride-oxide sandwich structure serves as top insulation. Both materials are stable at the high temperatures required for nanotube growth. Since silicon dioxide has a lower relative permittivity ($\epsilon_r = 3.9$) than nitride ($\epsilon_r = 7.5$), a thick silicon dioxide layer effectively reduces the capacitive current between the interconnects and the electrolyte. However, silicon dioxide is permeable to sodium ions, thus a dense silicon nitride layer is needed to block the ionic current flow. The final thin top oxide layer provides a

hydrophilic surface for cell adhesion. In comparison, silicon nitride is more hydrophobic and is less suitable for cell culture.

2.1.2.3 Interconnects

One of the most important decisions in material selection was to use doped amorphous silicon as the interconnect material instead of standard metals. Initially, platinum was used, with titanium as an adhesion layer to the silicon dioxide. After the CNT growth, microscopic cracks and hillocks in the top insulation layers were found where underlying metal leads were present (Figure 2.5). As a result, leakage current through the insulation layers increased by three orders of magnitude after the growth cycle (Figure 2.6a).

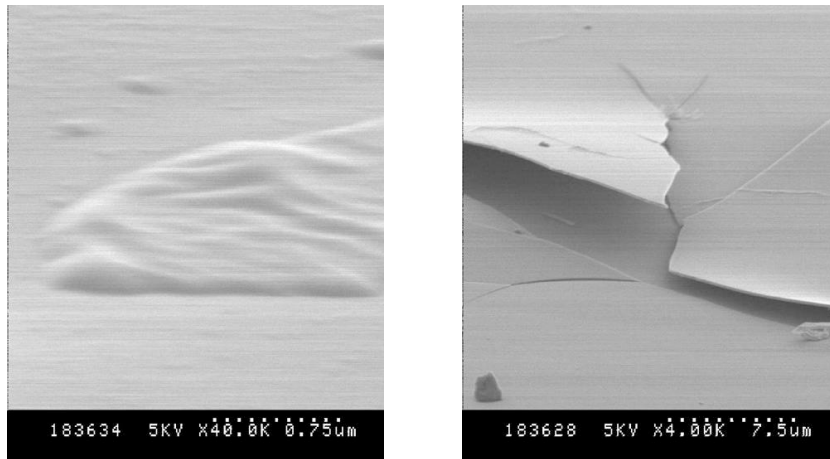


Figure 2.5 SEM images of the device surface after thermal cycles, with Ti/Pt interconnects.

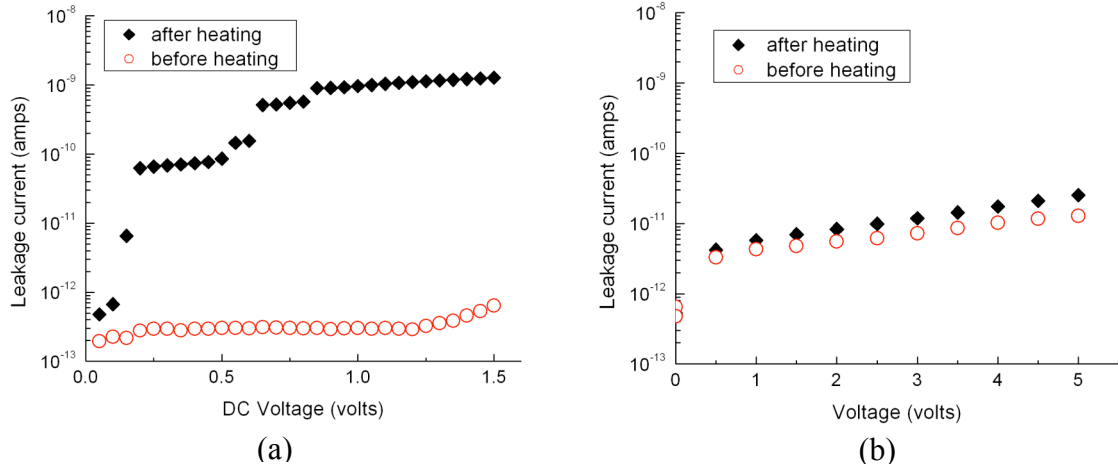


Figure 2.6 Leakage current through the insulation layer, before and after CNT growth. (a) With Ti/Pt interconnects, the leakage current increased by three orders of magnitude after the device was heated. (b) With poly-silicon interconnects, there was little increase in leakage current after the thermal cycle.

After excluding other possibilities, such as poor adhesion and nitride outgassing, we believe that the mismatch of the thermal expansion coefficients was the major cause for this insulation failure. The thermal expansion coefficients of Ti and Pt (Pt: $8.8 \times 10^6 \text{ K}^{-1}$, Ti: $8.6 \times 10^6 \text{ K}^{-1}$) are much higher than those of silicon dioxide and nitride (SiO_2 : $0.5 \times 10^6 \text{ K}^{-1}$, Si_3N_4 : $3.3 \times 10^6 \text{ K}^{-1}$). During the thermal cycle, the metal layers expand and contract much more than the oxide/nitride layers and pull the latter apart. Another possible cause was that Ti and Pt may have formed alloys with a much lower melting point during the thermal cycle.

This problem was solved by replacing Ti/Pt with heavily doped amorphous silicon. The good interface between silicon and silicon dioxide significantly reduces the thermal stress. The surface is smooth and the leakage current remains low after CNT growth cycles (Figure 2.6b). In addition, amorphous silicon serves as a better substrate for CNT growth. Compared to standard metals, it also offers higher optical transparency at visible wavelengths, which is convenient for inverted microscopy. Practically, the use of doped

silicon instead of platinum made the entire processing more compatible with the microfabrication facilities. The wafers could be processed in batches. It also enabled deposition of silicon dioxide and silicon nitride of higher quality (LPCVD instead of PECVD, see Section 2.3.1.2 for more details).

A drawback of doped silicon is its relatively high electrical resistance. This was minimized by increasing the dopant concentration and film thickness, reducing the interconnect length and increasing the width. A more quantitative description of the interconnect resistance can be found in Section 2.4.

2.1.2.4 Contact Pads

The contact pads were coated with Ti/Pt, to protect the doped amorphous silicon from exposure to air and consequent formation of native oxide layer. Platinum is chemically stable and is not easily oxidized. The thermal expansion coefficient mismatch is not a problem here, because the Ti/Pt layer is not sandwiched between two oxide layers, and can expand or contract freely.

2.1.3 Layout

The basic layout of the microelectrode array is shown in Figure 2.7. The chip size is 24 mm × 24 mm, with a total of 36 electrodes (6×6 array) and 4 large return electrodes. The relatively large chip size ensures enough volume of the chamber, which is a plastic ring bonded onto the chip after fabrication (see Section 2.3.2). A large chamber volume is beneficial in both electrochemical and cell experiments. There are 10 contact pads on each side of the chip. The pads are 1 mm wide and 3 mm long, with 0.5 mm intervals.

Transparency masks printed at 3600 dpi (MediaMorphosis Inc., CA) were used for photolithography in fabrication. This is a quick and low-cost solution allowing convenient change of the design. The resolution of the printer limits the minimal feature size to 10 μm. Features smaller than 20 μm are not well defined, and circular features are usually less smooth than rectangular ones. Because of this resolution issue, the smallest

electrode is chosen to be $30\ \mu\text{m} \times 30\ \mu\text{m}$ in size. Other arrays have large electrodes of $50\ \mu\text{m} \times 50\ \mu\text{m}$, $100\ \mu\text{m} \times 100\ \mu\text{m}$, and $160\ \mu\text{m} \times 160\ \mu\text{m}$. Some of the arrays have eight different electrode sizes, ranging from $30\ \mu\text{m} \times 30\ \mu\text{m}$ to $180\ \mu\text{m} \times 180\ \mu\text{m}$. The return electrodes are $500\ \mu\text{m} \times 500\ \mu\text{m}$.

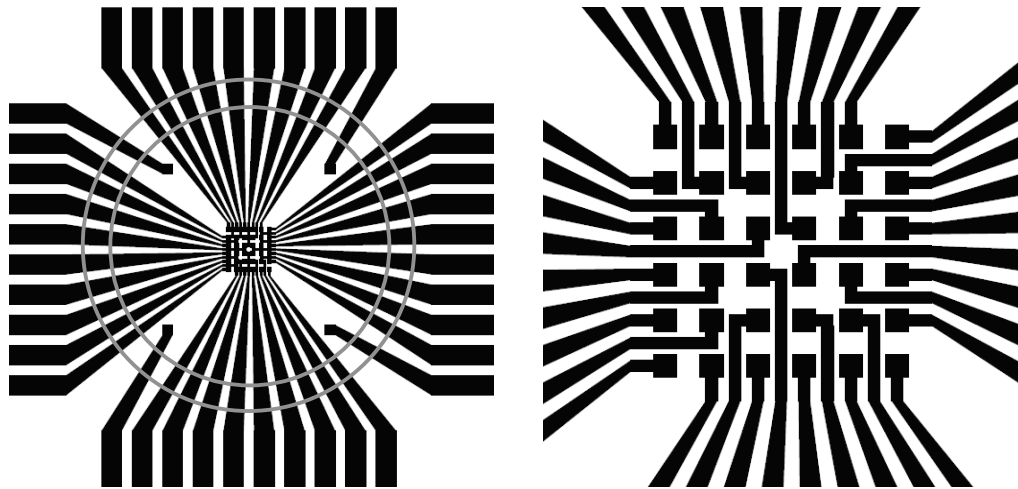


Figure 2.7 Layout of a 6×6 microelectrode array. Dark lines are the pattern of doped polysilicon interconnects. Grey circles mark the inner wall and outer wall of the chamber.

Because of the lower resolution of transparency masks ($10\ \mu\text{m}$), the design needs to incorporate better tolerance in misalignment. This is illustrated in Figure 2.8. The underlying poly-silicon pad is larger than the etched open via, which defines the active electrode area. The pad is $200\ \mu\text{m} \times 200\ \mu\text{m}$, to fit the largest electrodes ($180\ \mu\text{m} \times 180\ \mu\text{m}$). The pad size is uniform for convenience and consistency. The catalyst pad is $10\ \mu\text{m}$ larger than the via on each side (for example, a $100\ \mu\text{m} \times 100\ \mu\text{m}$ via will have a $120\ \mu\text{m} \times 120\ \mu\text{m}$ catalyst pad), to ensure that the nanotubes cover the entire via. The separation between neighboring poly-silicon pads is $200\ \mu\text{m}$. The interconnect is $100\ \mu\text{m}$ in width at the electrodes. This provides a good balance between reducing the

interconnect resistance R_i and reducing the capacitance C_c between neighboring interconnect traces.

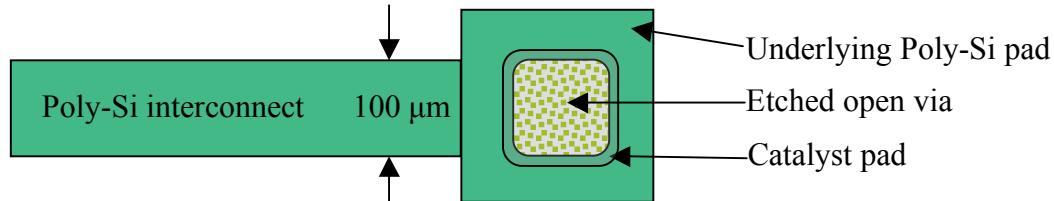


Figure 2.8 The underlying poly-silicon pad is $200\ \mu\text{m} \times 200\ \mu\text{m}$. The catalyst pad is $10\ \mu\text{m}$ larger than the via on each side, to ensure that the nanotubes covers the entire via. The interconnect is $100\ \mu\text{m}$ in width.

2.2 Carbon Nanotube Synthesis

There are three major approaches to the production of carbon nanotubes: arc discharge [15], laser ablation [24] and chemical vapor deposition (CVD) [25]. Arc-discharge has been successful in producing high quality bulk SWNTs and MWNTs at very large scale (tons-a-day capability) for commercial use. Laser ablation can synthesize SWNTs with very high quality (nearly defect free) at gram scales. CVD has been used to make carbon fibers and filaments for decades. It is now extensively used in CNT syntheses because it enables patterned growth on substrates, which is required in applications like field emission, nanoelectronics, and biosensors. In this work, multi-walled CNTs were synthesized using a catalytic thermal chemical vapor deposition system.

2.2.1 Arc-Discharge and Laser Ablation

The first observation of multi-walled carbon nanotubes was made by arc-discharge in 1991 [15]. Both arc-discharge and laser ablation involve evaporating solid carbon sources at very high temperatures ($3000\text{-}4000^\circ\text{C}$). In arc-discharge, carbon electrodes are evaporated by a helium plasma generated by high current. In laser ablation, laser pulses

vaporize the carbon target [24]. Both processes have a high by-product level (metal particles, amorphous carbon, fullerenes), and purification processes are usually needed.

2.2.2 Chemical Vapor Deposition

There are many different recipes for CVD nanotube growth, though all involve heating up catalyst particles under hydrocarbon gas flow. The catalysts are typically transition metal nanoparticles, such as iron, cobalt or nickel. Various hydrocarbon gases have been used, including methane, ethylene, acetylene and carbon monoxide. The growth temperature is usually 550-750°C for MWNTs, and 850-1000°C for SWNTs.

Although the growth mechanism of nanotubes in CVD synthesis is still not fully understood, it is agreed in the CNT community that the catalysts play an essential role. The catalysts are deposited either as nanoparticles, or form nanoparticles under high temperature. Feedstock hydrocarbon molecules adsorb on the catalytic particles. Upon catalytic dehydrogenation, hydrocarbon loses its hydrogen and breaks the carbon bonds. The free carbon atoms dissolve and diffuse into the catalyst particles. Due to the limited solubility of carbon in these metals (Fe, Ni, Co) at high temperature, they quickly saturate and carbon solids start to form. The formation takes a tubular shape because it contains no dangling bonds and is in a favorable low energy form. The tube diameter is the same as the size of the nanoparticle.

Depending on the interaction between the catalyst particles and the substrate, the growth can be divided into two categories: base growth mode and tip growth mode. If the catalyst adheres to the surface strongly, then carbon precipitates from the top surface of the particle and the particle remains at the root of the tube. This is called base growth mode. If the adhesion is weak, then the particle will be pushed up to the tip of the tube, and is called tip growth mode. The process of base-mode growth with ethylene as the precursor is illustrated in Figure 2.9.

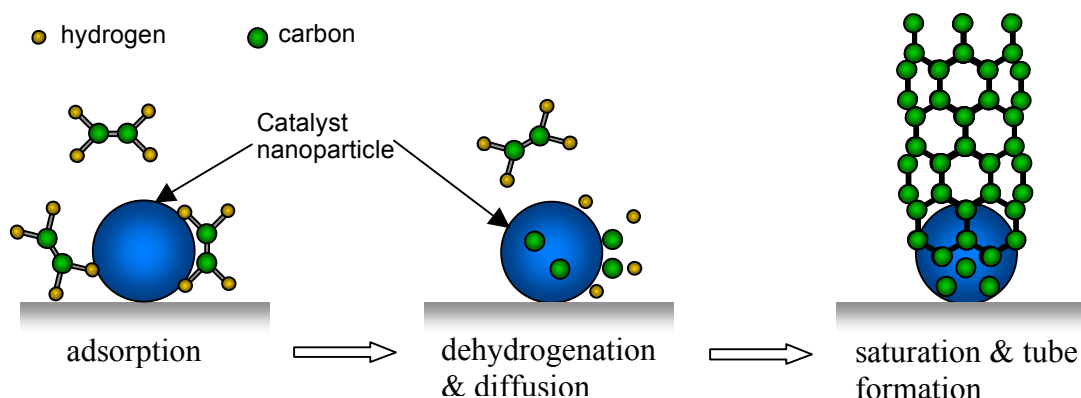


Figure 2.9 Illustration of CVD nanotube growth (base mode). Step 1: the hydrocarbon precursor molecules adsorb onto the catalyst nanoparticle. Step 2: the chemical bonds break under catalytic dehydrogenation. Carbon atoms dissolve and diffuse into the nanoparticle. Step 3: upon saturation, nanotube starts to form. The cylindrical structure minimizes the surface energy.

2.2.3 Synthesis and Results

A schematic of the catalytic thermal CVD system used for MWCNT growth [25] in this work is shown in Figure 2.10. A continuous film of 20 Å iron was evaporated onto silicon substrates as catalyst. The substrates were then transferred into a 2-inch quartz tube housed in a tube furnace. Argon (99.998% oxygen-free, Praxair Inc., CA) flows through the quartz tube at 1000 sccm for 10 minutes as a purge to remove the air inside. The temperature is then ramped up to 700°C in flowing argon. After the temperature is stabilized, the gas is switched to hydrogen (Praxair Inc., CA) which flows for a few minutes. Precursor ethylene gas (500 sccm, 99.9%, Praxair Inc., CA) carried by 500 sccm hydrogen was then fed into the tube for 1 to 10 minutes. The carrier gas greatly reduced the formation of pyrolytic amorphous carbon, which will be discussed in more detail in Section 2.2.4. When the desired growth time was reached, the ethylene was switched off and the chamber was purged with a mixture of hydrogen and argon gases for 5 minutes while keeping the temperature at 700°C. Holding the temperature high during the purge step prevents any remaining ethylene from forming other bi-products at lower

temperatures. Then the chamber temperature was ramped down in flowing hydrogen/argon. Hydrogen reacted with any oxygen traces from either air leakage or impurities in argon. The use of hydrogen protects the nanotubes from being damaged by oxygen at high temperature. Slow ramping ensured that the device did not go through a sudden temperature change, which could result in cracks due to thermal stress.

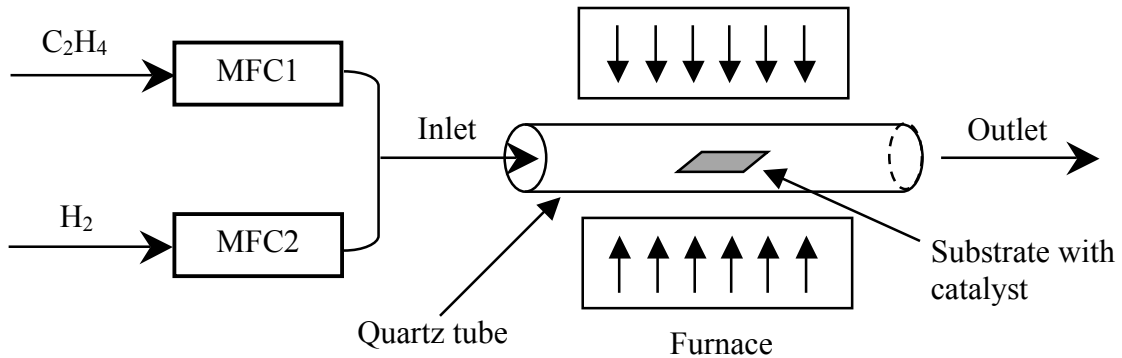


Figure 2.10 Schematic drawing of a catalytic thermal CVD system used for MWNT synthesis. MFC stands for mass flow controller.

Through van der Waals interaction, the nanotubes self-assembled into pillars projecting orthogonally from the surface (Figure 2.11). The CNT pillars were uniform, aligned and have high aspect ratio (up to 9:1). The size, geometry and location of the CNT pillars could be precisely defined with standard lithographic patterning of the catalyst. Pillars have been grown at a variety of base sizes ranging from 10 μm to 250 μm . The height of the pillars could be controlled by growth time. Growth rate was constant for at least the first 10 minutes at about 15 μm per minute (Figure 2.12), and was independent of the pillar size. The synthesis had very high yield and was exceptionally robust. Similar results were obtained using a wide range of catalyst thicknesses (20-50 \AA) and on a variety of substrates (doped and undoped silicon, silicon dioxide, quartz, and platinum).

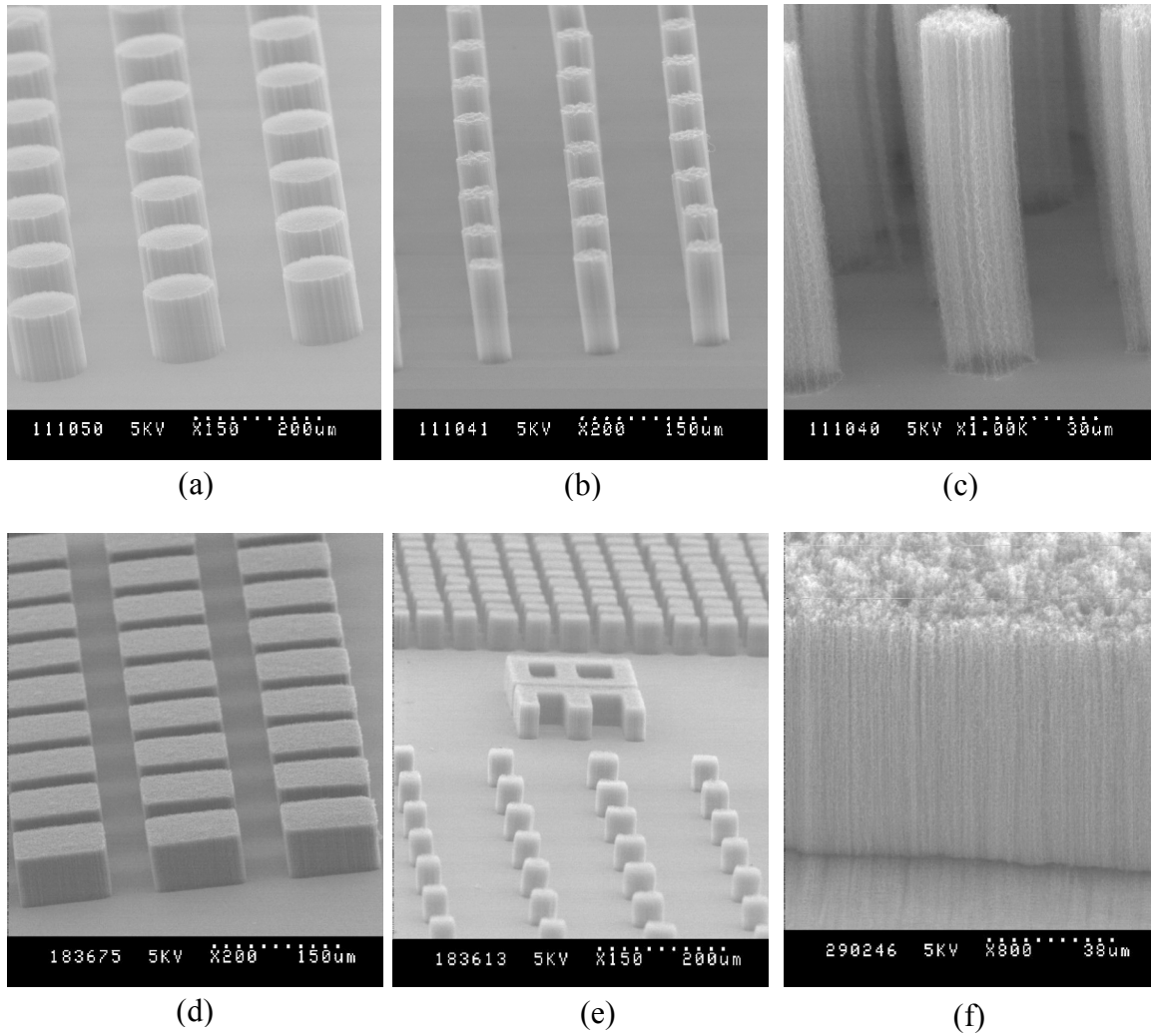


Figure 2.11 SEM images of MWCNTs on silicon substrates grown at 700°C, with 500sccm C₂H₄/500sccm H₂. (a) Pillars of 100 μm in diameter. (b) Array of 40 μm pillars. (c) A 20 μm pillar. (d) 100 μm×100 μm blocks. (e) 38 μm×38 μm pillar arrays with different spacing. (f) Aligned CNTs at the edge of a block.

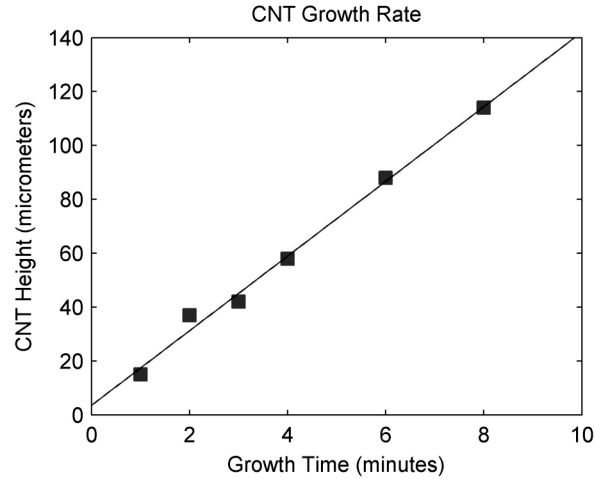


Figure 2.12 Growth rate of CNT pillars. The growth rate was about 15 μm per minute and was independent of the geometry and size of the pillars. The height of the pillars was estimated from SEM images.

Temperature has a strong impact on CNT synthesis. At lower temperatures, CNTs are not dense enough to self-assemble by van der Waals force and form entangled quasi-planar mats instead (Figure 2.13a). This structure can be useful for some applications in which planar electrodes are preferred. At higher temperatures, ethylene decomposes much faster. There is a significant increase in the nanotube diameter, as well as pyrolytic byproduct formation (Figure 2.13b). One consequence is the location sensitivity of the synthesis. Due to the temperature gradient inside the chamber, samples placed closer to the gas outlet form taller pillars with better alignment, while samples placed near the inlet form shorter pillars or quasi-planar mats with no self-alignment.

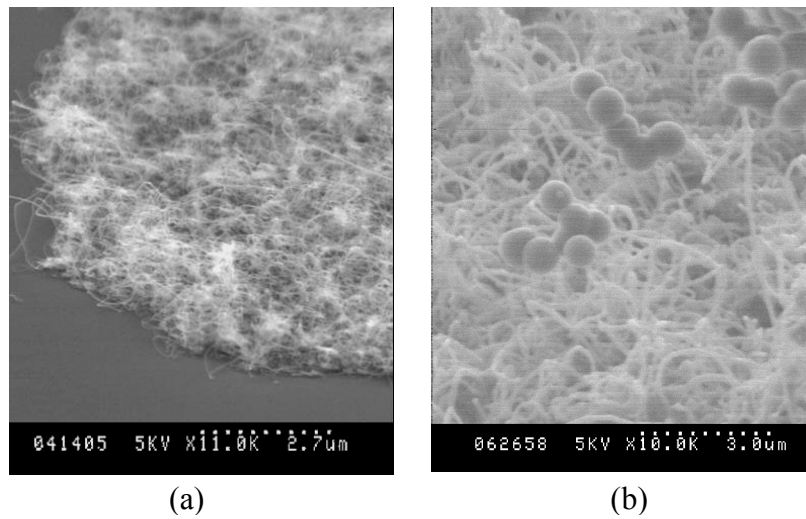


Figure 2.13 Temperature dependence of CNT growth. (a) Entangled quasi-planar pads grown at 670°C. (b) Formation of oil particles and nanotubes of larger diameter at 800°C.

Although CNT pillars could be synthesized with this method on silicon, as well as on silicon dioxide or Ti/Pt films deposited on silicon substrates, we observed that no growth occurred on Si/SiO₂/Ti/Pt multi-layers. In a control test, Ti/Pt islands were patterned on silicon substrates with a layer of oxide. Then a uniform film of iron was deposited covering the entire substrate. After growth, CNT formed everywhere except at the Ti/Pt islands (Figure 2.14). The reason is still not understood, but may be associated to silicide formation. By inserting a poly-silicon layer between Ti/Pt and SiO₂, the CNT growth was restored.

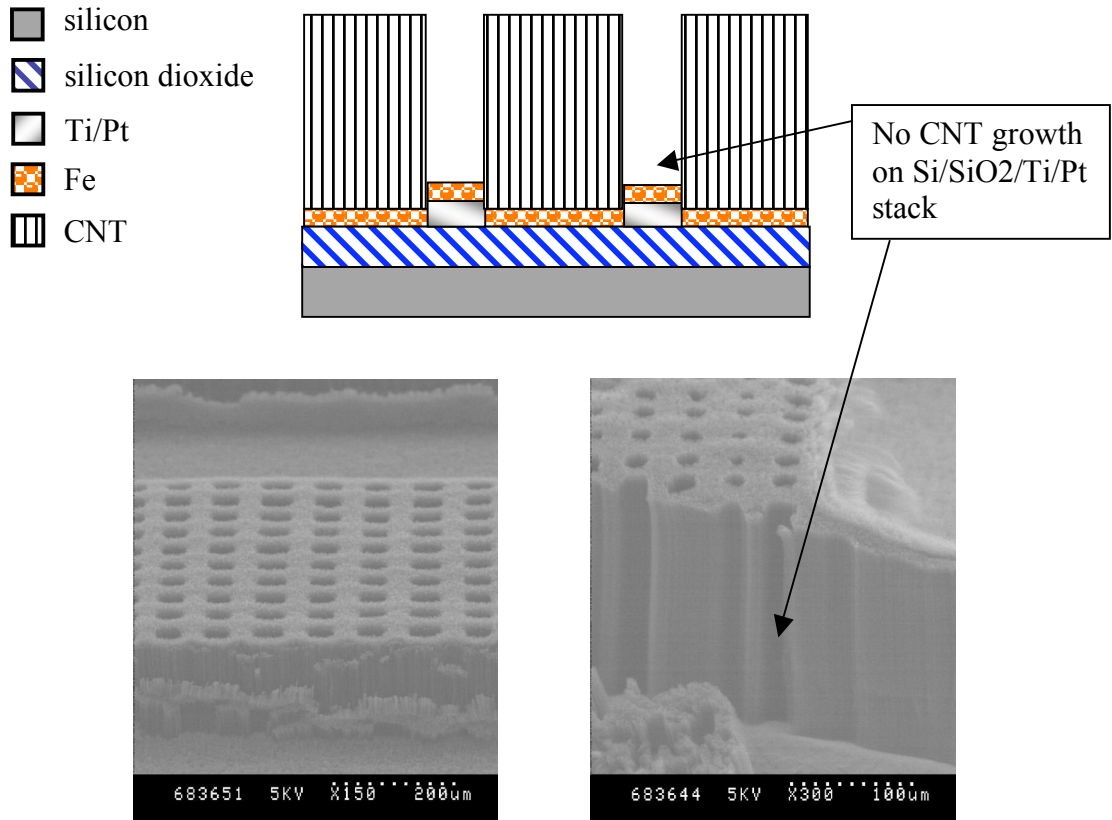


Figure 2.14 Substrate selectivity of CNT growth. The schematic drawing shows a cross section view of the test chip. SEM images: holey structure formed by selective growth of CNT on the test chip. Tunnels of very high aspect ratio formed through a CNT mat.

2.2.4 X-ray Photoelectron Spectroscopy (XPS)

Since the device is to be used in biological applications, its surface chemical composition is of special importance. One major concern is the location of the iron catalyst particles after CNT growth. Unfortunately, iron is known to be toxic to the nervous system [26, 27]. In order to locate the iron particles, surface analysis of CNT carpets from unpatterned growth was done using X-ray Photoelectron Spectroscopy (XPS). The only signals (see Figure 2.15) were a strong carbon peak, and a small oxygen peak which is

due to adsorbed oxygen on the carbon surface after growth. The characteristic spectrum of iron and its compounds (from 706.5eV to 713.5eV) was scanned at high resolution. No trace of iron, or any of its compounds was found. This indicated that the synthesis followed a base-growth mode, in which the catalyst particles adhered strongly to the substrate, at the root of the nanotubes. TEM images further confirmed that most of the iron nanoparticles were impregnated in the carbon nanotubes, and were not at the surface (data not shown here). Since there is no iron or other chemically toxic substances at the surface, the CNTs are chemically safe to interface the nervous system.

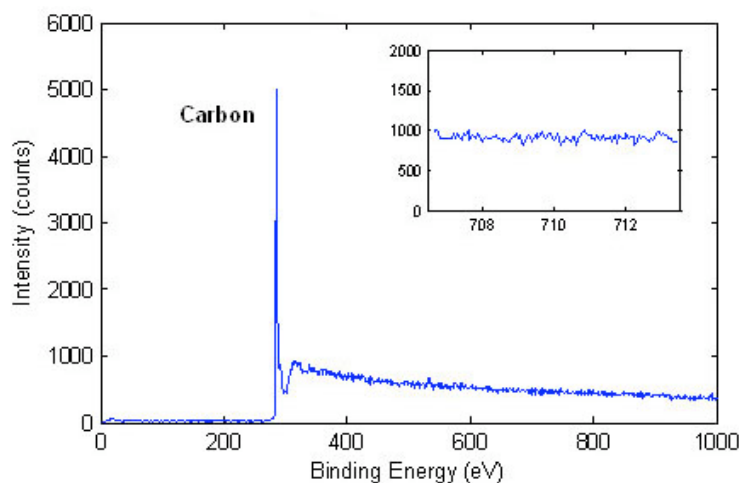


Figure 2.15 XPS spectrum of as-grown CNT surface. Inset is a scan from 706.5eV to 713.5eV, in the characteristic range of iron and its compounds. No traces of iron or compounds were detected.

The substrate surface not covered by CNT (where there was no catalyst) was also examined with XPS. It was found that the formation of pyrolytic amorphous carbon and other ethylene decomposition bi-products was significantly affected by the gases used in the synthesis. Initially, we employed pure ethylene without any carrier gas for the CNT growth. Resulting nanotube pillars were similar to the ones shown in Figure 2.11, but the entire device was coated with a uniform layer of amorphous carbon due to the thermal decomposition of ethylene (Figure 2.16a and Table 2-1). In addition, the atomic oxygen

to silicon ratio was higher than 2 (Table 2-1), as what would be for SiO_2 . The extra oxygen component indicated that other organic compounds were present on the surface, due to the thermal decomposition of ethylene. These substances not only changed the surface property of the device (making it hydrophobic), but could have also electrically shorted the nanotube microelectrodes. Furthermore, excess amorphous carbon impaired the electrochemical performance of the device (as will be discussed in Chapter 3).

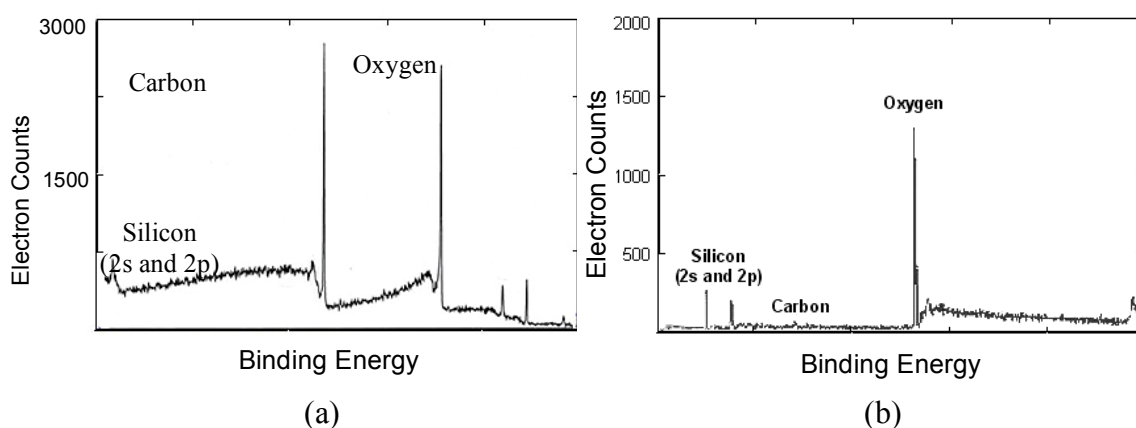


Figure 2.16 XPS of quartz substrate with no catalyst after growth. The carbon signal was from amorphous carbon instead of CNT. (a) Synthesis with pure ethylene (1000 sccm). There was large amount of amorphous carbon formation. (b) Synthesis with 500 sccm ethylene and 500 sccm hydrogen. Amorphous carbon formation was minimal. Other growth condition and sample preparation were identical in these two cases.

The first attempt to remove the amorphous carbon was intensive gas-phase oxidation after synthesis. The substrates were heated in ambient air at 550°C for an hour. It is known that amorphous carbon (as well as other carbon not in the form of nanotubes) burns at lower temperatures than nanotubes do. This method has been used for purifying nanotubes produced by arc-discharge. From the XPS data, it was obvious that the amorphous carbon had been completely removed. Comparing TEM images of nanotubes before and after the oxidation, no obvious damage to the nanotubes was observed. Unfortunately, the adhesion of nanotube pillars to the substrate was also weakened by

this oxidation process. In fact, most of the oxidized nanotube pillars detached from the substrate when they were immersed in water.

A more successful approach was to dilute the ethylene precursor with some carrier gas (hydrogen or argon). By reducing both the amount of hydrocarbon molecules and the time they stayed in the chamber, pyrolytic amorphous carbon formation was minimized (Figure 2.16b and Table 2-1). Adding hydrogen also produced longer nanotubes with better alignment, presumably because of its reaction with oxygen traces.

Table 2-1 Device surface composition after CNT growth cycle

Signal	Atom (%) (1000 sccm C ₂ H ₄)	Atom (%) (500 sccm C ₂ H ₄ + 500 sccm H ₂)
O 1s	22.0	64.3
Si 2s	9.7	32.6
C 1s	68.3	3.1

2.3 Device Fabrication

The microelectrode array was made using conventional silicon-based micro-fabrication processing. Substrates were patterned with interconnect and passivation layers, and then diced into chips before continuing with CNT synthesis. First generation devices used 500 μm thick 4-inch <100> silicon wafers. The second generation used quartz wafers instead.

2.3.1 Processing

The process flow for a device on quartz substrate is illustrated in Figure 2.17. The processes for silicon substrates were almost identical, except that a 1 μm -thick layer of thermal oxide (1000°C, wet oxidation) was first formed as bottom insulation.

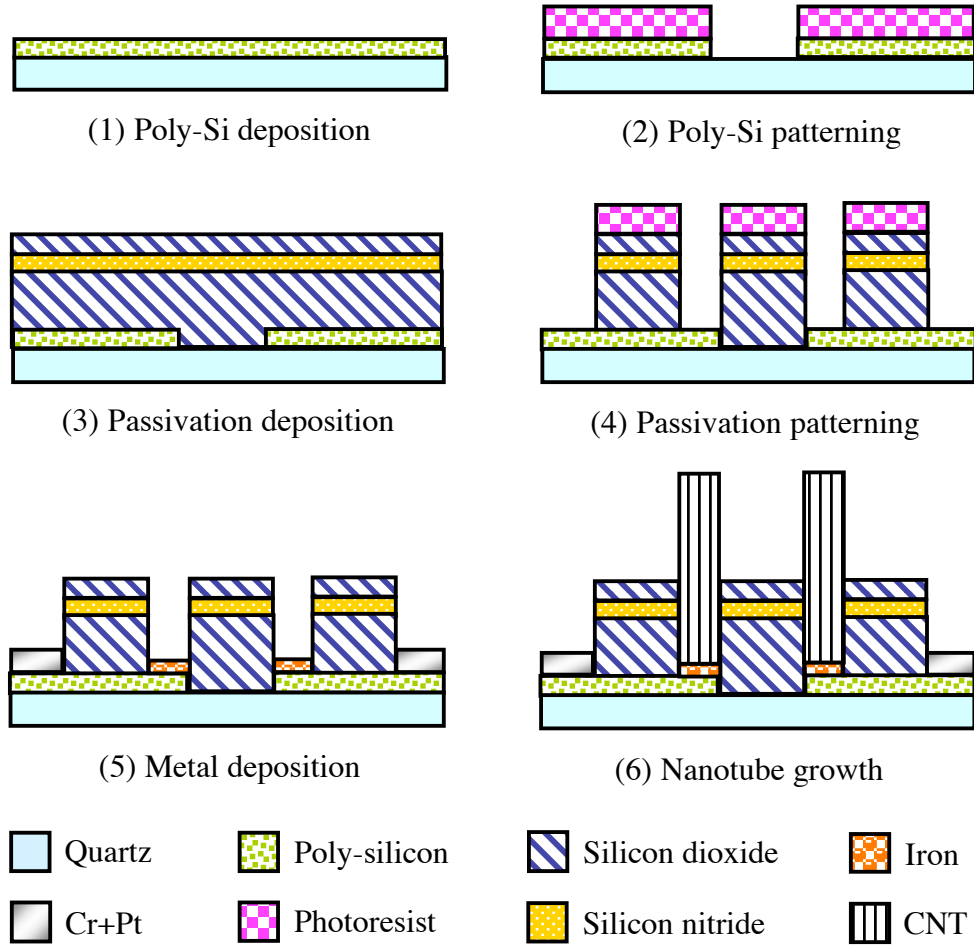


Figure 2.17 Fabrication process of the CNT microelectrode array.

2.3.1.1 Poly-Silicon Deposition and Patterning

For the conductive layer, 5000Å of in-situ phosphorous doped amorphous silicon was deposited using LPCVD (Low Pressure CVD) at 580°C (400mT, SiH₄ 200, PH₃ 3.0). To activate the dopants, the wafers were annealed in N₂ at 1000°C for 30 minutes. The resulting sheet resistance was ~10Ω/square. The resistivity was then:

$$\rho = \rho_s \cdot d = 10\Omega \cdot 0.5\mu m = 5 \times 10^{-4} \Omega \cdot cm \quad (2.1)$$

Therefore, the dopant concentration was 10^{20} cm^{-3} or higher. Diffusion doping at 800°C was initially used, but there was difficulty in achieving such high dopant concentration uniformly across the 5000\AA -thick layer. The diffusion-doped poly-silicon surface was also less smooth, likely due to the formation of large grains.

Standard UV lithography ($1\mu\text{m}$ SPR3612) defined the layout of electrodes, interconnects and contact pads. Doped-Si in undesired areas was removed by plasma etching ($\text{SF}_6/\text{CHClF}_3$, 400W, 150mTorr). The photoresist was then stripped by oxygen plasma at high temperature, followed by 20 minutes in 90% sulfuric acid/10% hydrogen peroxide at 120°C . For quartz devices, the doped silicon layer on the backside of the wafers was also etched away for higher optical transparency.

2.3.1.2 Passivation Deposition and Patterning

Passivation was accomplished by depositing sandwich layers consisting of $2\mu\text{m}$ -thick low-temperature silicon dioxide (LTO) (LPCVD, SiH_4/O_2 , 400°C), 1000\AA low-stress silicon nitride (LPCVD, $\text{SiH}_2\text{Cl}_2/\text{NH}_3$, 780°C), and 1500\AA LTO. To etch away the sandwich layers at the electrodes and contact pads, a layer of $1.6\mu\text{m}$ -thick photoresist (SPR3612) was patterned and hardened by 15 minutes UV exposure followed by one hour oven bake at 110°C , as a protection against the long plasma etch in CHF_3/O_2 . The high $\text{CHF}_3:\text{O}_2$ ratio (85:6) gave high selectivity of oxide to silicon, as well as excellent anisotropy in the etched profile. The CHF_3/O_2 plasma was also used to etch silicon nitride. The nitride layer on the backside of the wafer was also removed for better optical transparency. To compensate for the poor uniformity of oxide thickness and plasma etch rate, the wafers were rotated and shuffled several times during the etching process, and then immersed in 20:1 buffered oxide etch to ensure that oxide was completely removed. The photoresist was then stripped in a Gasonic Asher and the polymer deposited during the plasma etching step. Afterwards, the wafers were dipped shortly in 50:1HF to remove the oxide formed during ashing.

If Pt (or other metal) was used for the conductive layer, then the passivation layers could only be deposited by PECVD (Plasma Enhanced CVD) at 350°C due to material compatibility issues of the deposition equipments. Oxide and nitride films deposited by PECVD at such low temperature usually incorporate H₂, O₂ and N₂, which can result in outgassing, peeling or cracking during subsequent processing (such as CNT growth). By replacing Pt with doped polysilicon, the oxide and nitride films could be deposited by LPCVD, which produced films of superior quality compared to PECVD.

2.3.1.3 Metal Deposition and Patterning

Metal contact pads and catalysts were both patterned with a lift-off technique. A thick layer of resist (7µm SPR220-7) was used in order to cover the etched wafer uniformly. After photolithography, possible resist residues were cleaned up by 30-second oxygen plasma treatment. Then 60Å-thick chromium and 500Å-thick platinum layers were deposited by electron beam evaporation. Afterwards, the wafers were soaked in 1165 remover overnight, followed by 10 minutes agitation in an ultrasonic bath of fresh 1165 remover at 50°C. The remover dissolved the photoresist, and only where there was no resist, the Cr/Pt film could adhere to the substrate. After complete removal of lifted-off metal traces, the wafers were rinsed in DI water and spun dry.

At this point, the wafers were again coated with 7µm resist as a protection layer and then diced half way through (cut depth 200µm). This cut depth was shallow enough for the wafers to survive high speed spinning in the next lithography step, but sufficiently deep to break the wafers to chips later on. Dicing had to be done before iron patterning, because the extremely thin iron film could not survive the harsh dicing process.

After thorough cleaning (solvent rinse, oxygen plasma, and quick dip in 50:1 HF), 20Å Fe was deposited onto the electrode sites by e-beam evaporation and lift-off (same process as Cr/Pt patterning). Evaporation was done under high vacuum (~10⁻⁸ torr), to guarantee high CNT growth quality. The wafers were rinsed thoroughly in solvent and flowing DI water to remove any chemical traces.

The devices were then ready for nanotube growth, and could be stored in ambient air. CNT synthesis has been discussed in 2.2.3. Finished devices are shown in Figure 2.18.

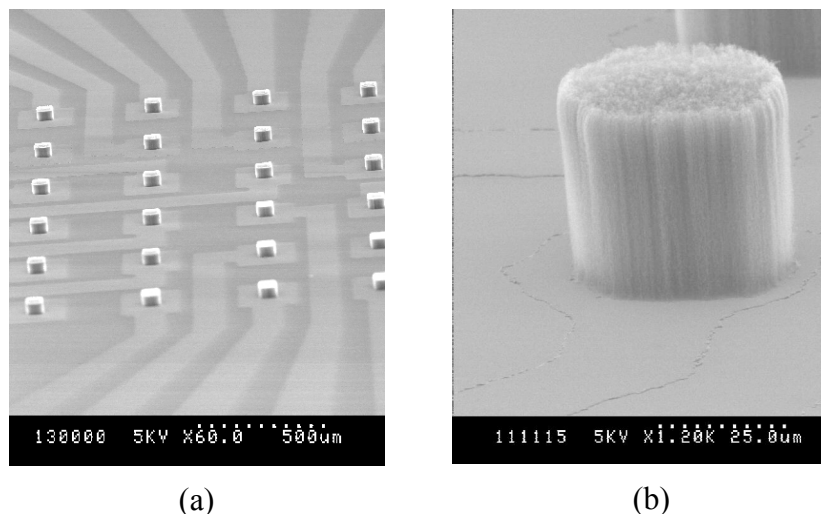


Figure 2.18 SEM images of CNT microelectrodes. (a): Array of 30 μm CNT pillar electrodes. (b) A 50 μm CNT pillar electrode. The underlying interconnects were barely visible since they were embedded under insulation layers.

2.3.2 Packaging

After CNT growth, a chamber for electrochemical and biological measurements was formed by bonding an acrylic ring (OD 5/8", ID 1/2", height 1/4") onto the chip with PDMS (poly(dimethylsiloxane)). The contacts were left outside the chamber for electrical connection (Figure 2.19). The chamber needed to have sufficient volume, so it could hold enough solution in the electrochemical experiments, and the culture medium would not evaporate too quickly in the cell experiments. The height of the chamber was limited by the working distance of the microscopes. The chosen ring size gave a maximum chamber volume of 800 μl . PDMS was allowed to cure at 70°C for two hours. Cured PDMS is biocompatible, and provides long-term bonding without leakage.

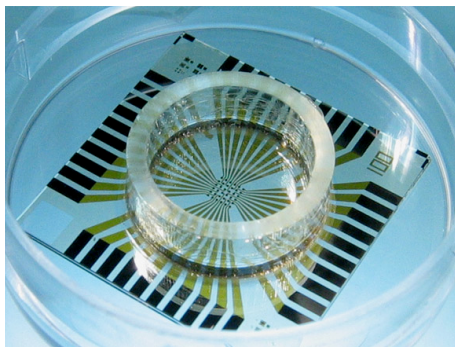


Figure 2.19 A CNT microelectrode array on quartz substrate with a bonded chamber, ready for electrochemical and cellular experiments.

A homemade connector was used for signal transmission between the device chip and the external units (Figure 2.20). The connector had two parts: a printed circuit board (PCB) and an acrylic holder. The chip fitted into the holder, and a bottom aperture in the center allowed inverted imaging. Good electrical connection between the contact pads on the PCB and the chip was achieved with low-resistance ZEBRA elastomeric connectors (Fujipoly, NJ). The ZEBRA connectors are constructed of alternating parallel layers of electrically conductive and nonconductive silicone elastomer. The electrically conductive layer is filled with silver-metal particles. With 0.1mm pitch, only coarse alignment was needed between the PCB and the chip (given that the contact pads are 1mm wide and with 0.5mm spacing). The PCB and the holder were connected with four screws, providing both alignment and sufficient clamping force to ensure a good electrical connection by slightly deforming the elastomeric connectors. Copper wires were soldered onto the end of printed interconnects on the PCB.

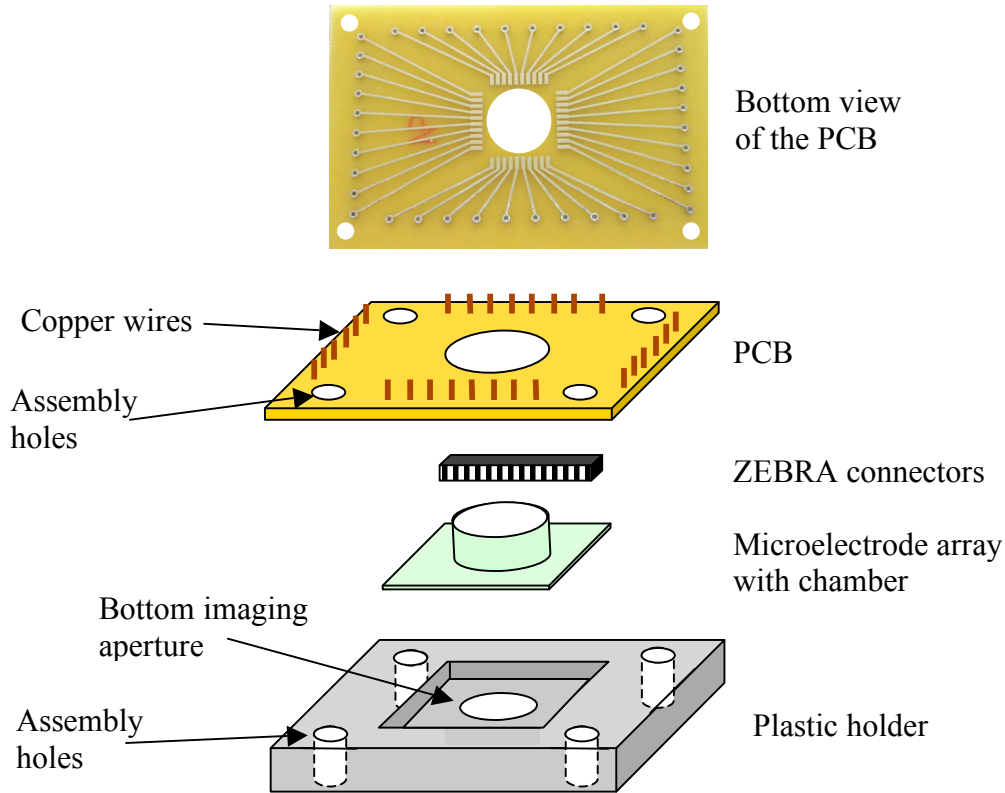


Figure 2.20 Two-part connector. The microelectrode array fits into the plastic holder. The aperture in the holder allows inverted imaging. Metal leads are printed on the bottom side of the PCB. Copper wires are soldered on the upper side for connection to external units. ZEBRA elastomeric connectors are used for electrical connection between the contact pads on the PCB and the chip. There are four assembly holes on both the PCB and the holder.

2.4 Parasitics: Calculation and Measurement

The basic circuit parasitics have been defined in section 2.1.1 (see Figure 2.3). With quartz substrates, some circuit parasitics such as C_s were eliminated. The value of the parasitics depends on the layout geometry and on the materials, and is summarized in Table 2-2. The theoretical calculation and/or experimental measurement of each are described in the following sections. All measurements were taken after the CNT growth cycle, to include any thermal effects.

Table 2-2 Values of the circuit parasitics

Parasitics	Value	Units
Passivation capacitance C_p	2.0-4.0	nF/cm ²
Crosstalk capacitance C_c	10	fF/cm
Interconnect resistance R_i	200	Ω
CNT resistance R_e	<10	Ω

2.4.1 Passivation Capacitance

The passivation capacitance C_p is determined by the passivation materials, their thicknesses, as well as the geometrical area of the interconnect. A first order approximation is given by the parallel plate capacitor model:

$$C_p = \epsilon_0 \epsilon_r \frac{LW}{d} \quad (2.2)$$

However, this simple model underestimates the passivation capacitance. A better expression is the Sakurai-Tamaru equation [28]:

$$C_p = \frac{1.15\epsilon_0\epsilon_r LW}{d} + 2.80\epsilon_0\epsilon_r L\left(\frac{t}{d}\right)^{0.222} \quad (2.3)$$

where ϵ_0 is the permittivity of space, ϵ_r is the permittivity of the passivation material, d is the thickness of the passivation layer, L , W , t are the length, the width, and the thickness of the interconnect trace, respectively.

In the sandwich passivation structure, the capacitors of the three layers are in series:

$$\frac{1}{C_p} = \frac{1}{C_{p1}} + \frac{1}{C_{p2}} + \frac{1}{C_{p3}} \quad (2.4)$$

Since the silicon nitride layer is much thinner ($d = 1000 \text{ \AA}$) and has a higher permittivity ($\epsilon_r = 7.5$) than silicon dioxide ($d = 2 \text{ \mu m}$, $\epsilon_r = 3.9$), its contribution to the total capacitance

is negligible. Using equation (2.3) ($t = 5000 \text{ \AA}$, minimum, $d = 2.15 \text{ \mu m}$, $\epsilon_r = 3.9$), the specific passivation capacitance is about 2.0 nF/cm^2 for 100 \mu m or wider traces.

C_p was measured with a test structure as shown in Figure 2.21. A strip of doped poly-silicon was entirely covered under passivation except for one contact pad. The chamber was filled with phosphate-buffered saline (PBS). A sinusoidal AC voltage was applied between a contact pad and a returning platinum wire electrode immersed in PBS. The impedance was recorded at different frequencies, and capacitance was calculated to be 4.0 nF/cm^2 . As we will see the chapter 3, the capacitive current through C_p is negligible compared to the signal current injected by the electrode.

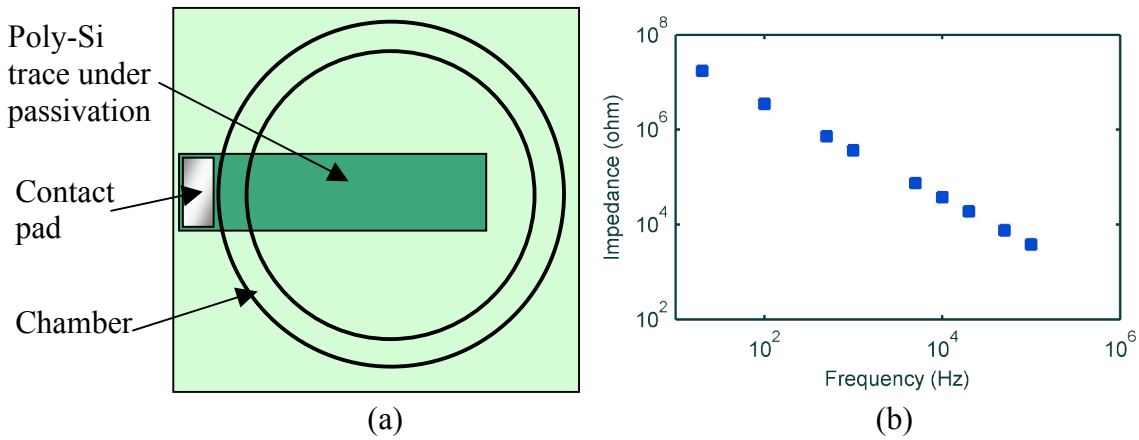


Figure 2.21 Measurement of passivation capacitance. (a) A test structure with doped poly-silicon trace embedded in passivation was immersed in PBS. The geometrical area of the trace was known (12 mm^2). (b) Measured capacitive impedance of the test structure, plotted over frequency. Zero DC bias, sinusoidal AC = 50 mV .

2.4.2 Crosstalk Capacitance

The capacitance between neighboring interconnect traces can be estimated from: [28]

$$C_c = 2\epsilon_0\epsilon_r L \left(\frac{S}{d}\right)^{-1.34} \left[0.03\left(\frac{W}{d}\right) + 0.83\left(\frac{t}{d}\right) - 0.07\left(\frac{t}{d}\right)^{0.222}\right] \quad (2.5)$$

where s is the separation between interconnects. The narrowest part of the interconnect has a width of $100\ \mu\text{m}$, and a separation of $100\ \mu\text{m}$. For the silicon dioxide layer, $d = 2.15\ \mu\text{m}$, $\epsilon_r = 3.7$, the capacitance per length is $6\ \text{fF/cm}$. For the silicon nitride layer, $d = 0.1\ \mu\text{m}$, $\epsilon_r = 7.5$, the capacitance is $4\ \text{fF/cm}$. Although s and W vary across the chip, C_c is always around that value. The crosstalk capacitors of the different layers are in parallel, hence the total C_c is $10\ \text{fF/cm}$, negligible for most applications.

2.4.3 Interconnect Resistance

The sheet resistance of the doped poly-silicon layer after annealing was about $10\ \Omega/\text{square}$ from four-point probe measurement. This was re-measured with a test structure (Figure 2.22) after CNT growth, to take into consideration any thermal effects from subsequent fabrication and synthesis steps.

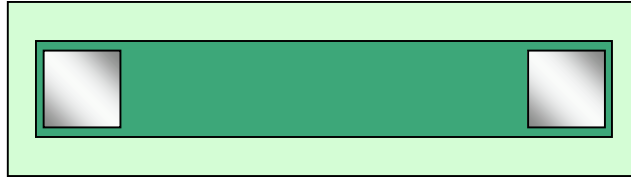


Figure 2.22 Test structure for interconnect resistance measurement. The poly-silicon stripe was $1\ \text{mm}$ by $6\ \text{mm}$, with contact pads on both ends.

The measured resistance of the test structure was $90\text{-}100\ \Omega$, and the sheet resistance was calculated to be $15\ \Omega/\text{square}$. Contact resistance may account for the small increase, and we could assume that the conductance of doped poly-silicon remained unchanged. The resistance of a trapezoid poly-silicon strip can be described as:

$$R_i = \rho_s \frac{L}{a_2 - a_1} \ln\left(\frac{a_2}{a_1}\right) \quad (2.6)$$

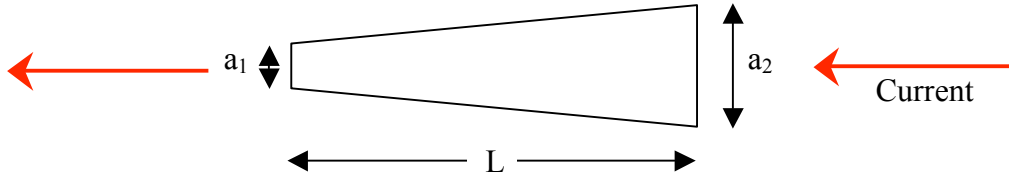


Figure 2.23 A trapezoid strip of interconnect.

where ρ_s is the sheet resistance, L is the length, a_1 , a_2 are the width of the ends. For the microelectrode array, $L = 8$ mm, $a_1 = 0.1$ mm, $a_2 = 1$ mm, therefore the resistance of the poly-silicon leads was about 200Ω .

2.4.4 CNT resistance

The resistance of an individual MWCNT has been reported to be 30-300k Ω [29-31]. The value strongly depends on the measurement method (how the contact to the nanotube is made), the diameter of the nanotube, as well as defects. For the CNT microelectrodes in this device, the individual MWCNTs can be modeled as resistors in parallel. The nanotubes are densely packed, so even in the smallest electrodes ($30 \mu\text{m} \times 30 \mu\text{m}$), the number of tubes is still on the order of 10^5 . As a result, the resistance of the CNT bundle is negligible.

$$R_e = \frac{r_e}{n} \sim \frac{300k\Omega}{10^5} = 3\Omega \quad (2.7)$$

However, this is an ideal scenario where every tube is in good ohmic contact. In reality, the contact resistance between the nanotube bundle and the underlying poly-silicon pads may need to be taken into account. The thermal CVD grown MWCNTs also contain more defects, thus will have a higher resistance, but still negligible compared to the interconnect resistance.

2.5 Summary

- Each electrode on the CNT microelectrode array is an ensemble of individual MWCNTs, which form a pillar protruding orthogonally from the substrate. The protruding geometry is advantageous in layers tissues by lowering the excitation current.
- MWCNT pillars were synthesized using a catalytic thermal chemical vapor deposition system. The growth used ethylene and hydrogen gases, at 700°C. The CNT pillars were uniform, well aligned and have high aspect ratio (up to 9:1). The synthesis followed the base-growth mode. The introduction of hydrogen gas minimized pyrolytic amorphous carbon formation.
- Prototype CNT microelectrode arrays were fabricated on quartz substrates, using conventional silicon-based micro-fabrication processes. Heavily doped poly-silicon was used for the interconnect layer, and a $\text{SiO}_2/\text{Si}_3\text{N}_4/\text{SiO}_2$ sandwich structure served as passivation.
- The parasitics of the microelectrode array were calculated, measured or estimated. The passivation capacitance is 2-4 nF/cm²; the crosstalk capacitance is 10 fF/cm²; the resistance of the poly-silicon interconnect trace is about 200 Ω ; the resistance of the CNT pillar itself is less than 10 Ω . All these parasitics are negligible in this application.

Chapter 3

Electrochemistry of the CNT Electrodes

In electrodes, charge is transported by electrons and holes. In electrolytes, charge is carried by the movement of ions. For either electrical stimulation or recording, current must flow between these two phases. The electrochemical processes at the electrode-electrolyte interface not only determine how this transition will occur, but also what impact it will bring to both the electrode and the electrolyte. Good electrochemistry is a key for safe and efficacious neural stimulation. In this chapter, we will discuss the electrochemical processes at the interface between the CNT electrodes and physiological solutions, and evaluate their efficiency and safety. We will start by introducing a theoretical model of the electrode-electrolyte interface.

3.1 The Electrode-Electrolyte Interface

When an electrode is immersed into an aqueous ionic solution, even if no bias voltage is applied, chemical reactions do take place at the interface. The simplest example is reduction and oxidation (redox) involving one-step electron transfer:



where O represents the oxidant and R is the reductant. The reaction starts towards one direction, driven by thermodynamic favorability. Soon excess charges build up on the electrode surface, and an energy barrier for the reverse reaction is reduced. As the

reactions proceed, equilibrium is reached, at which the forward reaction rate is equal to the reverse reaction, and the net current flow across the interface is zero.

There are two paths to keep a continuous net current flow across the interface (Figure 3.1). One is by capacitive current through the double-layer formed by the excess charge on the electrode surface and a space charge layer in the solution. The other is by resistive current through faradic processes, in which charges are actually transferred between the metal phase and the solution phase, and chemical species in the solution are either oxidized or reduced. Both cases are discussed below.

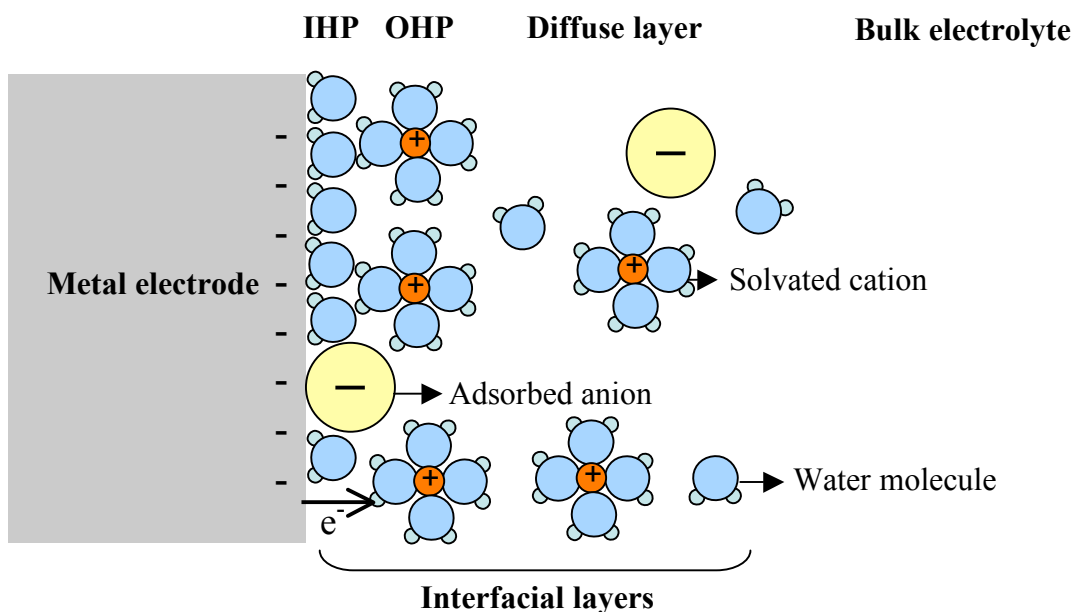


Figure 3.1 The surface layers formed when a metal electrode is immersed in an aqueous ionic solution. Double layer is formed by excess charge at the electrode surface and space charges (oriented water dipoles and ions). Electron can also be transferred directly across the interface during faradic reactions.

3.1.1 Double-Layer Capacitance

The double layer behaves like a capacitor. Although the double-layer capacitance is considered parasitic in many electrochemical experiments, it plays a critical role in this work and deserves an in-depth discussion.

The solution side of the double layer can be further divided into several sub-layers (Figure 3.1). 1) Close to the electrode, the water dipoles orient themselves and form a hydration sheath. Anions specifically adsorb onto the electrode surface. The locus of the adsorbed anions (or sometimes the locus of the water molecules) is called the *inner Helmholtz plane (IHP)*; 2) The locus of the nearest hydrated cations is called the *outer Helmholtz plane (OHP)*. These hydrated cations are separated from the electrode by the water dipoles. They are said to be nonspecifically adsorbed, because their interaction with the electrode only involves long-range electrostatic forces, and is independent on their chemical properties; 3) Thermal agitation causes the ions to distribute at a concentration gradient from the OHP to the bulk solution and form the *diffuse layer*.

3.1.1.1 The Gouy-Chapman-Stern (GCS) Model

The division of IHP, OHP and diffuse layer documents the gradual understanding of the double layer capacitance. It also reveals that the double layer is not an ideal capacitor. Instead, the capacitance is a function of the electrode potential, the electrolyte concentration and composition. The double layer was first described by Helmholtz as two sheets of charges, and the interfacial capacitance was modeled as a parallel-plate capacitor:

$$C_d = \frac{\epsilon_0 \epsilon}{d} \quad (3.2)$$

In Helmholtz's model, the double-layer capacitance was treated as a constant. However, experimental measurements contradicted this, showing that C_d was a variable of potential

and concentration. This discrepancy was explained by the Gouy-Chapman theory, which introduced the idea of a diffuse layer.

Unlike charges confined to the electrode surface (within 0.1Å) in metals, the excess charged ions in the solution distribute over a finite thickness. The thickness d results from a balance between the electrostatic attraction or repulsion by the electrode surface, and the thermal randomization. The higher the electrode potential, or the higher the solution concentration, the more compact the double layer becomes, hence the larger the capacitance. The capacitance C_d (in F/m²) was mathematically derived to be: [32]

$$C_D = \frac{\epsilon_0 \epsilon_r}{\kappa} \cosh\left(\frac{zV_0}{2V_T}\right) \quad (3.3)$$

where $1/\kappa$ is the characteristic thickness of the diffuse layer, z is charge of the ion, V_0 is the electrode potential, and $V_T = \frac{kT}{q}$ (k is Boltzmann's constant, q is the charge of the electron, and T is the temperature). The characteristic diffuse layer thickness κ for several different electrolyte concentrations is listed in Table 3-1.

Table 3-1 Characteristic thickness of the diffuse layer †

C^0 (M) ^b	$1/\kappa$ (Å)
1	3.0
10^{-1}	9.6
10^{-2}	30.4
10^{-3}	96.2
10^{-4}	304

† For a 1:1 electrolyte at 25°C in water.

For dilute aqueous solutions at 25°C, equation (3.3) can be simplified as:

$$C_d = 228z\sqrt{C^0} \cosh(19.5zV_0) \quad (3.4)$$

where C^0 is the bulk concentration of the solution. The Gouy-Chapman theory predicts the capacitance to vary with the potential in a parabolic shape. The minimum is at the *Potential of Zero Charge (PZC)*, and then C_d increases rapidly when V_0 diverges from PZC.

In reality, the double layer can not become infinitely thin. The ions have a finite size, and the water molecules (in either the hydration sheath or the hydrated ions) prevent them from approaching the electrode beyond a minimal distance. Stern's modification added the *outer Helmholtz plane (OHP)* into consideration, and separated the interfacial capacitance into two components:

$$\frac{1}{C_d} = \frac{1}{C_H} + \frac{1}{C_D} \quad (3.5)$$

C_H is the capacitance of the OHP, and C_D of the diffuse layer. The double layer now can be described as these two capacitors in series. After modification, the predicted behavior of C_d by the Gouy-Chapman-Stern (GCS) model is plotted in Figure 3.2. When the potential is near PZC, C_d is dominated by the diffuse layer and has a strong potential dependence; at larger potentials, the C_H term dominates and C_d approaches a constant, as depicted by the Helmholtz model. C_d is also dependent on the solution concentration. In concentrated electrolytes, the diffuse layer is so thin that C_d is almost constant.

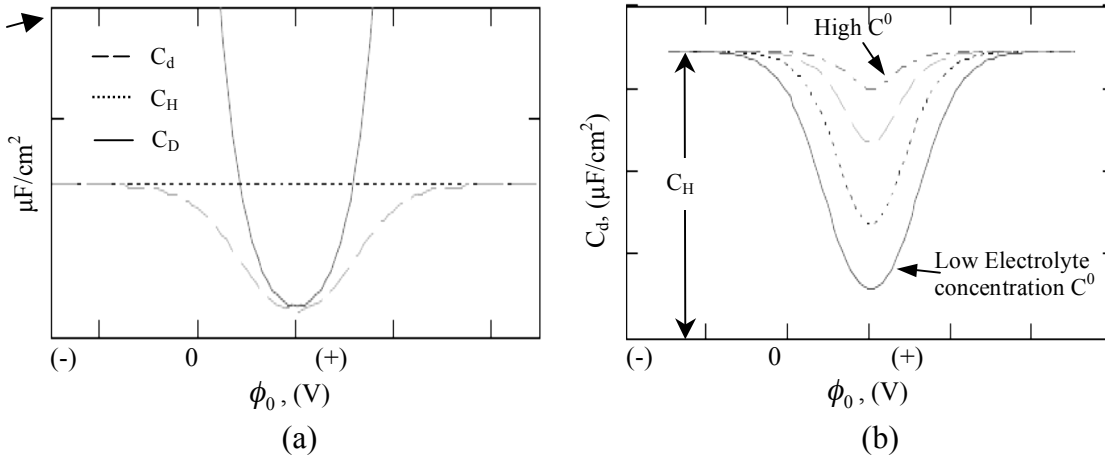


Figure 3.2 Expected behavior of the double layer capacitance based on the GCS model. (a) The two components of the total capacitance C_d : OHP capacitance C_H and diffuse layer capacitance C_D . (b) C_d with different electrolyte concentrations. The minima is at $E-E_z = 0$. After [32].

3.1.1.2 Estimate of Double-Layer Capacitance

When an electrode interfaces to biological systems, the electrolyte is usually an aqueous physiological solution. The relative permittivity of water is about 80 at 25°C, but can be as low as 6 at the interface [33]. The thickness of OHP is about 5 Å. So C_H for aqueous ionic solutions at body temperature can be calculated from equation (3.2) to be 11 $\mu\text{F}/\text{cm}^2$ (assuming $\epsilon_r = 6$). For physiological solutions such as saline, the relative permittivity of the diffuse layer is close to 80. The ion concentration is 10^{-1}M . From equation (3.4), the diffuse layer capacitance C_D is estimated to be 70 $\mu\text{F}/\text{cm}^2$ at its minimum (at $\phi_0 = 0$). Applying equation (3.5), the total double-layer capacitance C_d is dominated by C_H , and is nearly constant (Figure 3.2b, high C^0). Experimentally, the typical C_d value of bare metal electrodes is measured to be 10-40 $\mu\text{F}/\text{cm}^2$.

The double-layer capacitance of various forms of carbon (solid, powder, fiber, etc) strongly depends on the sample preparation, and ranges widely from 1-70 $\mu\text{F}/\text{cm}^2$ [34]. Electrically, graphite can be considered a semi-metal. Along the basal plane, the

electrons are delocalized and can move freely, as they do in metals. The resistivity in that direction is about $2\text{-}5 \times 10^4 \text{ } \Omega \cdot \text{cm}$. The resistivity normal to the basal plane can be 1,000 times higher, and can be considered insulating. In the electrolyte, an extra capacitive component needs to be considered for the graphite basal plane [35, 36], and the total C_d is written as:

$$\frac{1}{C_d} = \frac{1}{C_{sc}} + \frac{1}{C_H} + \frac{1}{C_D}$$

where C_{sc} is the capacitance of the space-charge layer in the semiconductor. For intrinsic semiconductors,

$$C_{sc} = (2\varepsilon_0\varepsilon_r q^2 n_i / kT)^{1/2} \quad (3.7)$$

where n_i is the intrinsic concentration of electrons and holes. C_{sc} of graphite is smaller than C_H or C_D , so the overall capacitance is dominated by C_{sc} . This accounts for the lower double-layer capacitance of the graphite basal plane compared to standard metals. The typical value of C_d in the graphite basal plane is about $5 \text{ } \mu\text{F}/\text{cm}^2$. The graphite edge plane usually has a higher capacitance, due to the contribution of the surface groups.

3.1.2 Charge Transfer and Warburg Impedance

In parallel to the double layer capacitor, there is also a resistive element across the electrode-electrolyte interface. This resistive path, though usually essential for most stimulating electrodes, is of less importance for the CNT device (as will be demonstrated later in this chapter). Therefore it will be described only briefly here. A more complete explanation can be found in the literature [32, 37].

As mentioned earlier, when an electrode is immersed in an ionic solution under zero bias, equilibrium is rapidly reached, at which the reduction current equals the oxidation current, and the net current flow across the interface is zero. The absolute value of the oxidation (or reduction) current over a unit area is referred to as the exchange current

density J_0 . When a potential is applied to the electrode and drives it away from this equilibrium, a net current starts to flow. The current density is related to the overpotential η ($\eta = V_{applied} - V_{equilibrium}$) by the Butler-Volmer equation:

$$J = J_0 (e^{((1-\alpha)z\eta/V_T)} - e^{(-\alpha z\eta/V_T)})$$

where α is the symmetry factor that measures the symmetry of the energy barriers. Therefore the transfer “resistance” is a non-linear element. In symmetric systems, α equals 0.5, and the Butler-Volmer relation is approximately exponential for large overpotentials (which is usually the case for stimulation applications):

$$J = J_0 e^{z\eta/2V_T} \quad (3.9)$$

and the transfer resistance is:

$$R_t = \frac{\partial \eta}{\partial J} = \frac{2V_T}{zJ} \quad (3.10)$$

For small overpotentials (such as in neural recording), the current-voltage curve falls into the linear region, and the transfer resistance can be written as:

$$R_t = \frac{\partial \eta}{\partial J} = \frac{V_T}{J_0 z} \quad (3.11)$$

In general, materials with larger J_0 values are preferred for stimulating electrodes, so a small voltage can produce a higher current.

When electrodes are operating at high current densities, the faradic reaction rate is fast at the electrode surface. The reactant concentration is lower at the interface than in the bulk solution, forming a concentration gradient. The limited diffusion rate of the reactant leads to the Warburg impedance Z_w , which can be modeled as a parallel R-C circuit:

$$(3.12)$$

$$\frac{1}{Z_w} = \frac{1}{R_w} + j2\pi C_w$$

Both R_w and C_w are frequency dependent:

$$R_w = \frac{1}{2\pi C_w} = \frac{V_T}{z^2 F C^0 \sqrt{\pi f D}} \quad (3.13)$$

in unit of $\Omega \cdot \text{cm}^2$. F is the Faraday's constant, C^0 is the reactant concentration in bulk solution in moles/cm³, D is the diffusion constant, and f is the ac frequency. Notice that

the impedance is related to $\frac{1}{\sqrt{f}}$. At low frequencies, the reactants need to diffuse

farther, resulting in a higher Warburg impedance. Alternatively, the Warburg impedance can also be viewed as one circuit element with a constant phase of -45° .

3.1.3 Spreading Resistance

The final element to be included in the microelectrode circuit model is the electrolyte resistance, R_s , that current encounters when spreading out between the microelectrode and a distant, large counter electrode. For a planar disk electrode of radius r , the spreading resistance can be analytically solved [38] and written as:

$$R_s = \frac{\rho}{4r} \left(\frac{x}{x+r} \right) \quad (3.14)$$

where ρ is the conductivity of the solution ($72 \Omega \cdot \text{cm}$ for saline), and x is the distance between the working electrode and the counter electrode. If the counter electrode is far away, then:

$$R_s = \rho / 4r \quad (3.15)$$

For a planar rectangular electrode with one side exposed to the electrolyte [37]:

$$(3.16)$$

$$R_s = \frac{\rho \ln(4l/w)}{\pi d}$$

where l is the length, and w is the width of the electrode. For small electrodes, spreading resistance contributes significantly to the system impedance. For example, R_s is 3.2 k Ω for a 100 $\mu\text{m} \times 100 \mu\text{m}$ square planar electrode in saline, and 10.6 k Ω for a 30 $\mu\text{m} \times 30 \mu\text{m}$ electrode.

The interfacial circuit elements described by the microelectrode theory are summarized in Figure 3.3.

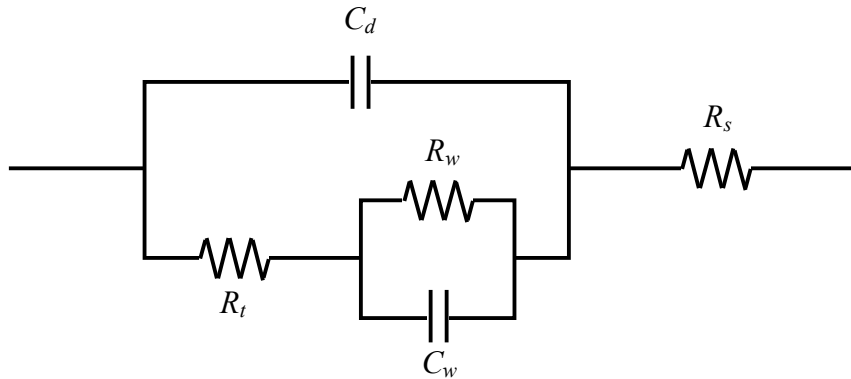


Figure 3.3 Equivalent circuit model of the electrode-electrolyte interface. C_d : double-layer capacitance; R_t : transfer resistance; R_w and C_w : Warburg impedance; R_s : spreading resistance.

3.2 Electrochemical Guidelines for Neural Stimulation

Both capacitive and faradic pathways can be used for neural stimulation. The capacitive mechanism is ideal for neural stimulation because no chemical change occurs to either the tissue or the electrode. However a major problem is that the capacitive current is usually small compared to the cell stimulation threshold. For metal electrodes, only about 20 $\mu\text{C}/\text{cm}^2$ of real electrode area can be injected by the double layer [39], before the onset of faradic reactions. The capacitive charge injection ability can be increased by

adding a thin insulating layer with high dielectric constant on the electrode surface, however, this usually is still not sufficient for applications in the central nervous system where 1 mC/cm^2 is required [13].

Since their capacitive charge injection is far from being sufficient, metal electrodes rely predominantly on faradic processes. Faradic reactions at the electrode-electrolyte interface can be further divided into two categories: reversible reactions and irreversible reactions. One example of a reversible faradic reaction is the redox of iridium oxide:

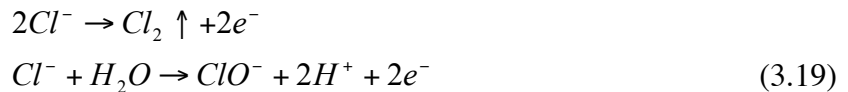


In such reactions, the change made to the electrolyte (or the electrode) can be completely undone by reversing the direction of the current. Thus reversible faradic reactions are acceptable for neural stimulation under charge balanced protocols (for example, symmetric biphasic current pulses).

Most common irreversible faradic processes include the electrolysis of water:



and the oxidation of chloride ions:



Irreversible reactions will significantly alter the chemical composition and pH of the electrolyte (i.e., the extracellular fluid), produce biologically toxic products, or corrode the electrode. This not only damages the electrodes, but also causes abnormalities in the neural function or the cell structure [40]. Therefore, irreversible faradic reactions are undesirable for neural stimulation.

3.3 Cyclic Voltammetry

To find out which charge injection mechanism(s) the CNT electrodes use, they were first characterized by cyclic voltammetry. Standard electrochemical experiments use a three-electrode cell, including a working electrode, a reference electrode (usually Ag/AgCl, or saturated calomel (SCE)), and a counter electrode. In cyclic voltammetry (CV) experiments, the potential V between the working electrode and the reference electrode is swept at a constant rate between two pre-defined values (Figure 3.4). The potential of the reference electrode is stable, so V reflects only the change of the working electrode potential. Current flows between the working and the counter electrodes, and is measured and plotted over the potential as the cyclic voltammogram.

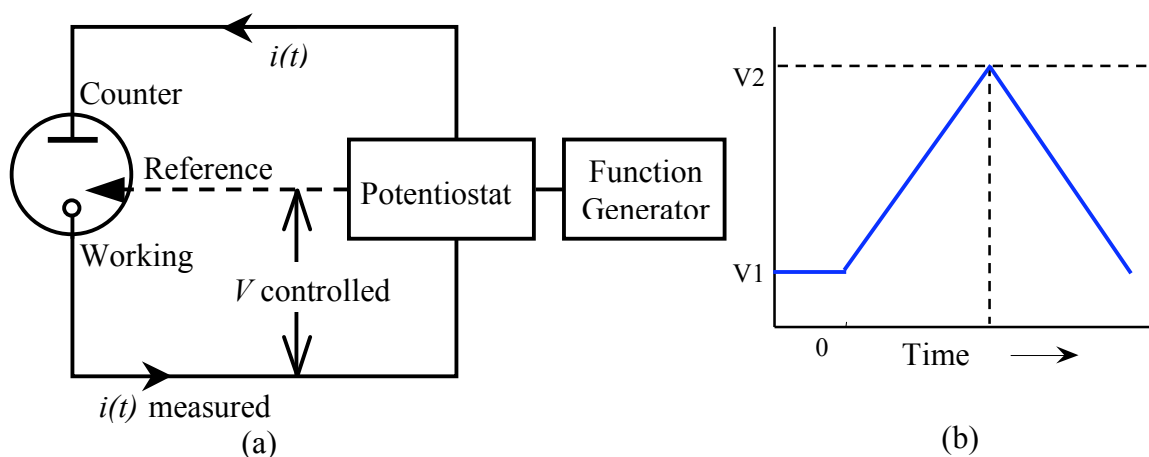


Figure 3.4 Basic principle of cyclic voltammetry. (a) The potential V between the working electrode and the reference electrode is controlled by a potentiostat. (b) V is a triangular wave between two set values V_1 and V_2 . The current between the working and counter electrode is measured.

In our experiment, a two-electrode system was used. The CNT microelectrode array served as the working electrode, a large Ag/AgCl coil as both reference and counter electrode, and phosphate-buffered saline (PBS, pH=7.4) as electrolyte. The surface area

of the Ag/AgCl coil was large enough so that the current used in the experiments would not cause appreciable potential shift at its surface. Results from a three-electrode system (with a platinum wire as counter electrode) were compared to the two-electrode system, and no difference was found. A potentiostat (Gamry FAS2 Femtostat, Gamry Instruments, PA) was used to control the potential and measure the current. Data were acquired and analyzed with Gamry software *Framework* and *Echem Analyst*.

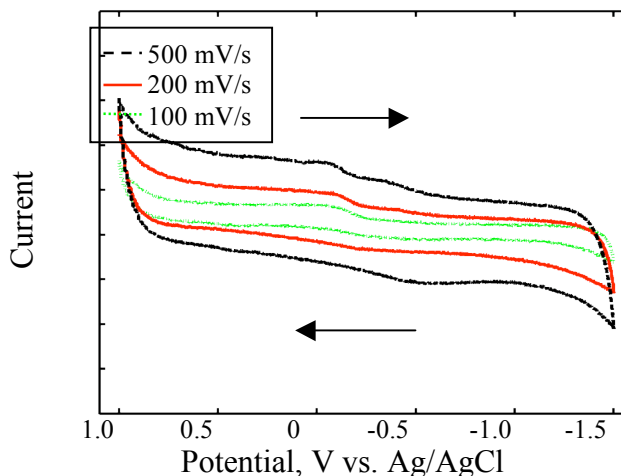


Figure 3.5 Cyclic voltammogram of a CNT electrode in PBS. Scan rate: 100, 200, and 500 mV/s. The arrows indicate the scan direction.

The cyclic voltammogram of a CNT electrode at different scan rates is shown in Figure 3.5. The sudden increase in current at +1.0V and -1.5V mark the evolution of oxygen and hydrogen, respectively. This defines the *operational potential window*. Beyond these two potentials, hydrolysis would take place and significantly alter the pH of the local electrolyte. Compared to platinum and iridium oxide (Figure 3.6), CNT has a much wider “safe” potential window to work within.

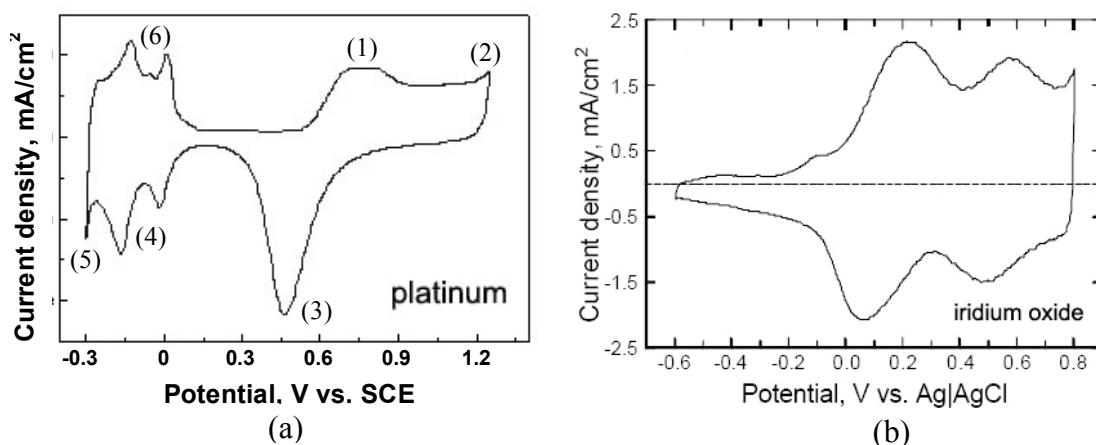


Figure 3.6 Cyclic voltammogram of platinum and activated iridium oxide. (a) Platinum. The potential window is 1.5 V wide. The marked peaks are adsorption, desorption and evolution of hydrogen and oxygen. (b) Iridium oxide. The redox reaction $Ir^{3+} \leftrightarrow Ir^{4+} + e^-$ attributes to the pair of peaks.

Like other carbon-based materials such as diamond and graphite, CNTs are electrochemically inert. The voltammogram was basically featureless in the potential window, indicating that the current was delivered primarily through charging and discharging of the interfacial double layer, instead of through faradic reactions. In comparison, both platinum and iridium oxide inject current predominantly through faradic reactions. The peaks in platinum voltammogram (Figure 3.6a) are: (1) oxide build-up; (2) oxygen evolution; (3) reduction of oxides and oxygen; (4) hydrogen adsorption; (5) hydrogen evolution; (6) hydrogen desorption. For iridium oxide, the faradic peaks are from the reduction and oxidation of iridium ions. The voltammogram of CNT was reproducible, with a small reduction peak at -0.4V. This was most likely due to the reduction of adsorbed oxygen on the nanotubes. Similar peaks were also found by other researchers [34, 41]. It was reported that samples annealed at 900°C in argon did not show this reduction peak, presumably due to desorption of oxygen and volatilization of surface oxide groups. The reduction peak reappeared when the samples were exposed to air. In another experiment, the peak current increased with oxidation time in acids, supporting the suggestion that the peak originates from reduction of surface oxides.

The CNT electrodes are appealing for neural stimulation since they behave like capacitor electrodes with no faradic reactions. Now, the question is whether they can inject enough charge to exceed the physiological response threshold within the operational window. The charge storage capacity of capacitor electrodes can be described as:

$$Q_{\max} = CV_{\max} = \epsilon_0 \epsilon_r \frac{A}{d} V_{\max} \quad (3.20)$$

It is clear that the maximum charge storage is determined by four factors: the relative permittivity ϵ_r of the dielectric material, the surface area A , the dielectric layer thickness d , and the “safe” potential range V_{\max} . From this point of view, an advantage of CNT over traditional metal/dielectric capacitor electrodes (such as Ta/Ta₂O₅) is that CNT uses the double-layer as the “dielectric”. For physiological solutions, the double layer is only about 10 Å, much thinner than the dielectric films used in most other capacitor electrodes, and there is no concern of dielectric break-down under high voltages. The relative permittivity ϵ_r of physiological solution is fairly high (~80), and CNTs also have a wide potential window (2.5 volts). In neural stimulation, it is desirable to increase Q as much as possible. For the CNT electrodes, since the values of ϵ_r , d , and V_{\max} are all determined, the only adjustable parameter will be the real surface area A . However the size of the electrode is usually restricted by the application, thus a reasonable approach is to increase the ratio of real area to geometrical area, i.e., the roughness of the electrode surface.

3.4 Surface Modification

The CNT electrode surface is inherently rough. In fact, one of the most promising applications of CNTs is energy storage [42]. They have been made into supercapacitors [43], batteries [44] and fuel cells [45], which take advantage of their large surface area. However, the surface of the CNT electrode consists primarily of the graphitic basal plane. The non-polar basal plane makes as-grown CNT highly hydrophobic, with most of its large surface area inaccessible in aqueous solutions. Obviously, the surface of these CNT

microelectrodes needs to be treated to improve their hydrophilicity, consequently increasing the real surface area and the charge storage ability. However, the treatment should not change the structure of the device or affect the electronic properties of the nanotubes. In addition, the treatment must be biocompatible.

With growing interest in the biomedical applications of CNT, great effort has been made to increase its solubility in water. One of the most commonly used methods is oxidative acid treatment. Originally developed for CNT purification, this technique has been found to stabilize the dispersion of CNTs in aqueous solutions, by generating surface oxides and defects on the nanotubes. Oxidized CNTs can be further modified by forming covalent bonds between the surface oxide groups and other molecules [46]. However, acidic oxidation usually involves extensive refluxing/sonication in concentrated acid. The experimental conditions are mechanically and chemically too harsh for the CNT microelectrode arrays. The acid would attack the catalyst particles at the root of the nanotubes and lift them off. Sonication would also dislocate the nanotubes. Furthermore, acid treatment will shorten and cut the CNTs, since the tips and the defect sites are oxidized faster. It is also known that acidic oxidation removes the outer graphene cylinders of the MWNTs successively. For CNT electrodes, this would be disastrous because the outermost layer is usually where the electrical contact is made and electron transport occurs.

The hydrophobic CNT electrodes can be wetted by organic solvents. Solvents such as ethanol or isopropyl alcohol are also miscible with water, hence can increase the wettability of the CNT electrodes. However, solvents are extremely toxic to biological cells. A significant amount of solvent molecules may be trapped between the highly porous nanotubes, even after extensive rinsing. The effect of solvent residues on cell health will be described in Chapter 4. Hence solvent wetting is also not appropriate for this application.

For the above reasons, other surface modification techniques are needed for the CNT microelectrode array. Investigated methods and their qualitative effects are described below, while the quantitative results measured electrochemically will be discussed in Sections 3.5 and 3.6.

3.4.1 Thermal Oxidation

Surface oxides, such as carbonyl and carboxyl groups, can also be formed through gas-phase reactions with agents such as O₂, CO₂ and H₂O. The amount of surface oxides increases with the oxidation temperature, and reaches a maximum at 400-500°C. At higher temperatures, the amount of surface oxides starts to decline because of increasing formation of gaseous oxides (CO and CO₂). Since amorphous carbon burns off at a lower temperature than CNTs, gas-phase oxidation can further increase the accessible surface area by removing the amorphous carbon deposited between neighboring nanotubes.

Heating the CNTs at 400°C in air for an hour effectively turned them hydrophilic. The contact angle of a small water droplet (10µl) on CNTs before and after the treatment demonstrated the transition. As-grown CNTs were so hydrophobic that the water droplet balled up on the surface, and sometimes even slid off from the substrate. The CNT surface was not wetted after the droplet was removed,. The CNT chip was then heated in air (400°C, 60 minutes) and cooled down to room temperature. The water droplet spread out immediately on the surface, and completely wetted it. Heat treatment at 250°C also improved the wettability, but the contact angle was not as small.

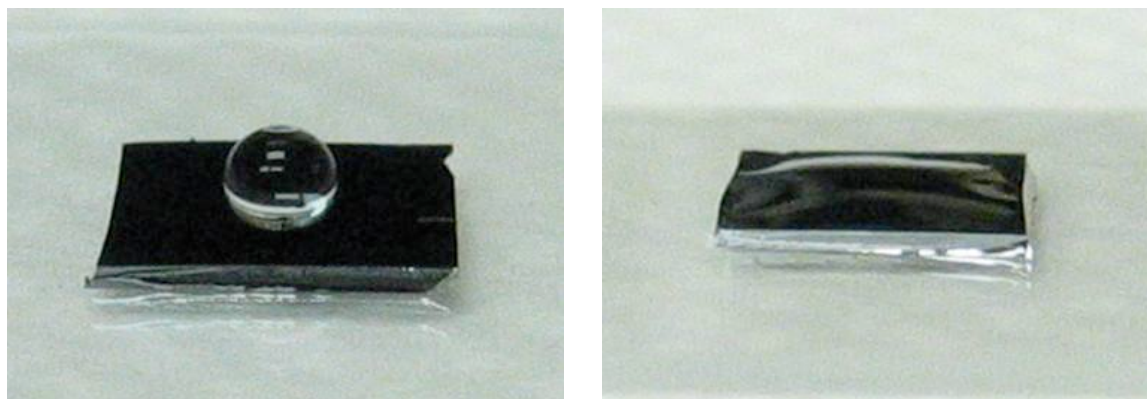


Figure 3.7 Thermal treatment of CNTs. The substrate is a silicon chip covered with vertically aligned MWCNTs. Contact angle of the water droplet demonstrated that the CNT surface changed from highly hydrophobic (left) to hydrophilic (right) after thermal oxidation.

However, the effect of thermal oxidation was not stable. At room temperature in air, the surface remained hydrophilic for one or two days, but gradually became hydrophobic again. The mechanical stability of the device was also compromised during the thermal process. Heated CNT electrodes sometimes detached from the substrate during electrochemical cycles due to weakened attachment. Another concern is that the surface oxides may change the electronic structure of CNT and reduce its electrical conductivity. The CNT electrodes can also be oxidized by alkaline solutions. The hydrophilicity can be increased by either chemical (soaking) or electrochemical (applying voltage cycles) oxidation of the electrodes in 1M NaOH. However, similar problems, such as weakened attachment to the substrate, also exist for alkaline treated CNT electrodes.

3.4.2 Non-covalent Functionalization

It is known that a variety of molecules readily adsorb onto CNT surface, through non-covalent mechanisms, such as hydrophobic interactions, π - π stacking, hydrogen bonding, electrostatic forces, and van der Waals forces. Non-covalent binding is one of the least invasive methods to modify the CNTs. In many cases, only incubation is needed. There

is no significant disturbance to either the structure or electronic properties of the CNT device.

The amphiphilic poly (ethylene glycol)-lipid conjugates (PEG-PL) (Figure 3.9) binds strongly to CNTs via Van der Waals and hydrophobic interactions between the two lipid alkyl chains and the nanotube sidewall, while the PEG chain extends into water and makes the modified CNT more soluble [20, 47]. Upon incubation with 0.1 mg/ml PEG-PL (Avanti Polar Lipids, AL) for 2-20 hours at room temperature, the CNT microelectrodes turned hydrophilic. The transition could be visualized under an optical microscope (Figure 3.8). Untreated hydrophobic CNT arrays were highly reflective when immersed into water, i.e., the pillars looked glossy. After incubation with PEG-PL, CNTs became more hydrophilic, and appeared dark in water.

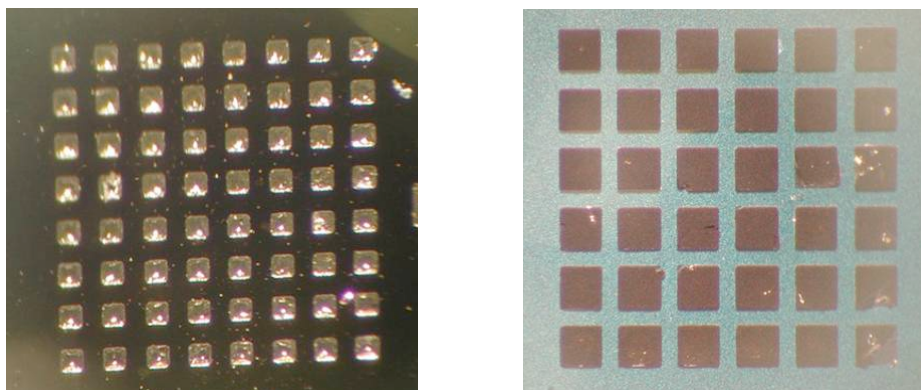


Figure 3.8 Visual evaluation of the hydrophilicity of the CNT pillars. The CNT pillars were immerse in water, and the reflection at the surface was examined. On the left, as-grown pillars were highly reflective (glossy-looking), indicative of their hydrophobicity. On the right, the pillars turned hydrophilic and appeared dark after surface modification.

To verify the adsorption, we first labeled the PEG-PL-NH₂ chains with fluorescent FITC molecules (see Appendix A) (Figure 3.9). FITC binds to the primary amine group. CNT pillars grown on silicon dioxide surface were then incubated with the PEG-PL-FITC

conjugation in dark. After incubation, the chip was thoroughly rinsed with DI water and then imaged under a confocal microscope. As shown in Figure 3.10, the CNT pillars were labeled by the fluorescent FITC molecules, indicative of the absorption of PEG-PL on the surface. Since the silicon dioxide surface was hydrophilic, the concentration of PEG-PL was much lower on the oxide surface than on the nanotubes. Confocal microscopy also provided a narrow focus plane (Z sectioning), further increasing the contrast of the image. In comparison, no fluorescent signal was detected from thermally oxidized CNT pillar samples (Figure 3.10c), further proving that the binding was based on hydrophobic interactions. The samples were imaged on a daily basis and the binding lasted for at least four days in lipid-free PBS. Two background controls were used: (1) untreated CNT pillars were imaged to determine the auto-fluorescence level; (2) CNT pillars were incubated with FITC molecules to decide signals from direct CNT-FITC interaction. No fluorescence was detected from the CNT pillars in either case (images not shown here).

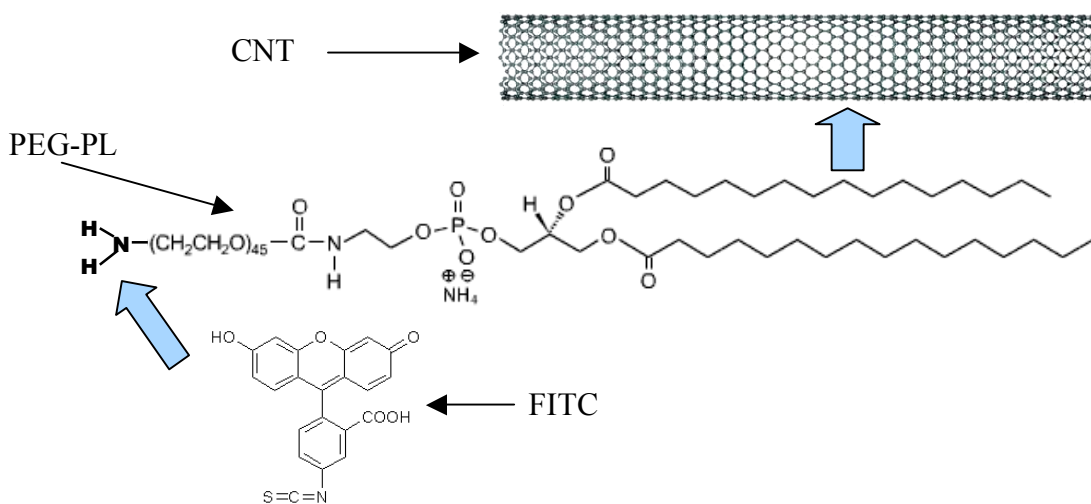


Figure 3.9 Binding the PEG-lipid conjugates (PEG-PL) to CNT. The lipid tails bind to the sidewall of CNT via hydrophobic interaction. FITC molecules can be attached to the amine group of PEG-PL and function as a fluorescent label to detect the binding process.

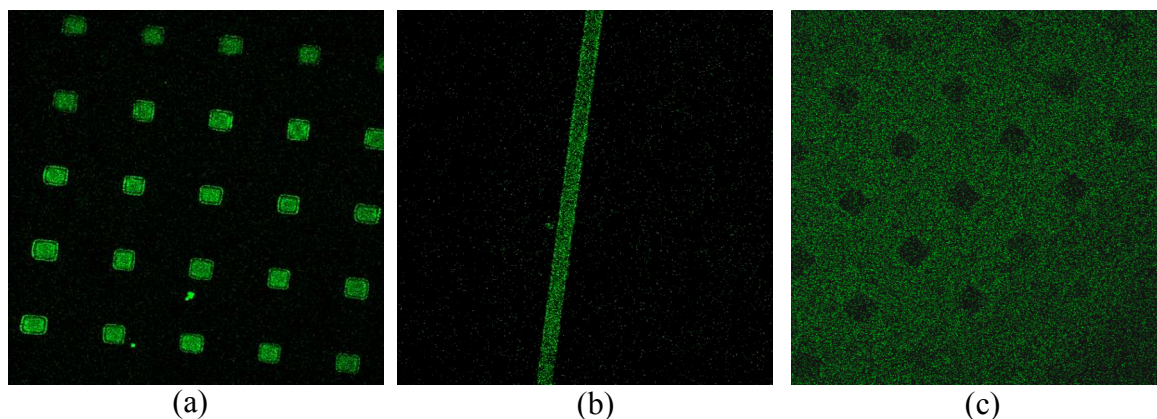


Figure 3.10 Confocal images of CNTs after incubation with FITC-labelled PEG-PL. (a) and (b): As-grown CNT pillars or stripe were highlighted by FITC after incubation, as a result of PEG-PL adsorption. (c) Thermally oxidized CNT pillars had no adsorption. The PMT (photomultiplier tube) gain was manually increased in (c), to show the location of the pillars. With the same gain as in (a) and (b), (c) would have appeared completely black.

A similar hydrophobic-to-hydrophilic transition (as Figure 3.8) was also observed after the CNT microelectrodes were incubated with cell culture media. The transition was attributed to non-specific adsorption of proteins in the culture medium to the nanotube surface, because CNT pillars incubated in protein-free basic media (such as NeuralBasal) did not exhibit such improvement in hydrophilicity. The mechanism of non-specific adsorption can be more complicated than simple hydrophobic interactions. Electrostatic interactions, hydrogen bonding, and the amino affinity of CNTs [48] may also be involved.

Non-covalent functionalization is a particularly interesting surface modification method. It holds the potential to enhance both the electrochemical performance and the biocompatibility of the CNT microelectrodes, while preserving their geometrical structures and electronic properties. The following sections will discuss how these modifications affect the electrochemical properties of the device. The impact on the biocompatibility of CNT will be shown in Chapter 4.

3.5 Impedance Spectroscopy

The real surface area of the CNT microelectrodes is not directly measurable. However, the interfacial double-layer capacitance C_d is proportional to the surface area. (In this thesis, the symbol C_d may have the unit $\mu\text{F}/\text{cm}^2$, for *specific* double-layer capacitance per geometrical area or real surface area; or the unit μF , when the surface area is taken into consideration. The unit is either specified, or is explicit in the context.) C_d can be estimated from cyclic voltammograms:

$$C_d = \frac{i}{dV/dt} \quad (3.21)$$

where dV/dt is the scan rate, and i is the capacitive current where there is no faradic peaks. However, C_d is a variable of the electrode potential (Section 3.1.1), which changes rapidly over a large range in CV measurements. In addition, the value of C_d measured from voltammograms is also dependent on the voltage scan rate used (Figure 3.11). At slower scan rates, a larger proportion of the surface area can be reached in the porous electrode, and the slower charging processes can also contribute to the capacitive current [34], hence C_d increases with decreasing scan rate.

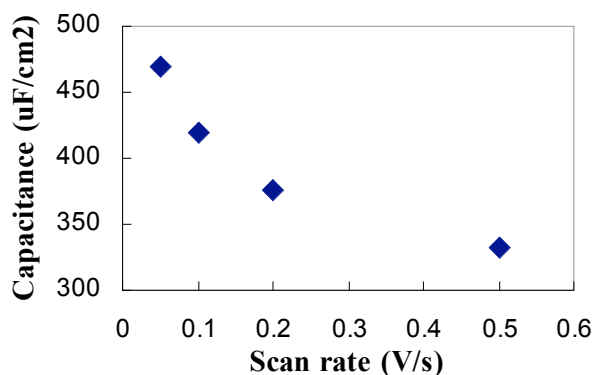


Figure 3.11 The double-layer capacitance of a CNT electrode measured from cyclic voltammogram has dependence on the voltage scan rate. The y-axis is capacitance per geometrical area.

A more suitable method to measure C_d is electrochemical impedance spectroscopy (EIS). EIS studies an electrode's complex impedance over a wide range of AC frequencies. The electrochemical cell, the data acquisition hardware and software were identical as the ones used in cyclic voltammetry experiments. In EIS, the DV bias voltage is locked at a preset value, while a small sinusoidal AC signal (typically < 50mV) is applied to the electrode at different frequencies. For most cases in this work, the bias is chosen to be zero, where the process is purely capacitive. The current and the phase were recorded, from which the impedance was derived. Results can be represented using a "Nyquist plot", in which the imaginary part of the impedance (Z_{img}) is plotted on the Y-axis vs. the real part (Z_{real}) on the X-axis. Another presentation method is the "Bode plot", where the absolute value of the impedance ($|Z|$) and the phase-shift are plotted as a function of the frequency. The spectra are usually analyzed by equivalent circuit modeling. By fitting the parameters, quantitative information of the electrochemical system (such as the double-layer capacitance, the solution resistance, and the electrode kinetics) can be extrapolated.

3.5.1 Equivalent Circuit

The EIS spectra of a representative CNT microelectrode after non-covalent surface treatment are shown in Figure 3.12. The data could be fitted into an equivalent circuit model (Figure 3.12c), where the interface is represented by a constant phase element

(CPE, with impedance $Z = \frac{1}{C_d(j\omega)^\alpha}$) in parallel with faradic impedance, Z_f , and R_s is the

spreading resistance in series. Parameter fitting for this electrode ($160 \times 160 \mu\text{m}^2$, $40 \mu\text{m}$ tall) resulted in a value of 0.97 for α , very close to an ideal capacitor in which $\alpha = 1$, and 785 nF for the interfacial capacitance C_d . So the specific double layer capacitance was $1600 \mu\text{F}/\text{cm}^2$ geom. The faradic impedance, Z_f , was $65 \text{ M}\Omega$, much higher than the capacitive impedance at all tested frequencies. Thus current predominantly took the capacitive path. The spreading resistance, R_s , was $2.9 \text{ k}\Omega$.

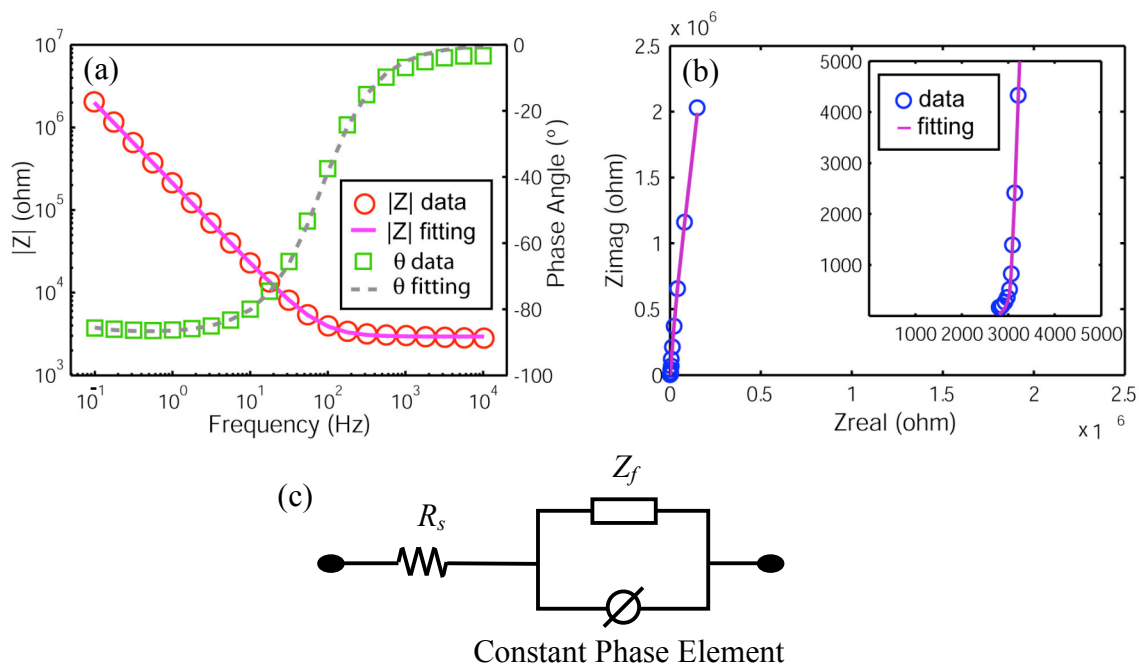


Figure 3.12 (a) Bode plot and (b) Nyquist plot of a representative CNT electrode (geometrical area = $5 \times 10^{-4} \text{ cm}^2$) in PBS, after non-covalent binding. DC bias: 0V; sinusoidal AC oscillation: 10mV, at frequencies from 0.1 Hz to 10 kHz. Data were fitted to an equivalent circuit model as illustrated in (c).

3.5.2 Effect of Surface Modification

The EIS spectra of CNT electrodes before and after different modification processes are plotted in Figure 3.13. The untreated CNT electrode behaved as a capacitor, and the Bode plot was linear on a log scale:

$$|Z| = \frac{1}{\omega C} = \frac{1}{2\pi f C} \quad (3.22)$$

$$\log |Z| = -\log(2\pi C) - \log f$$

Thermally oxidized and non-covalently modified CNT electrodes had a significant drop in the impedance (10 to 100 times) at low frequencies. Since the impedance was capacitive in this frequency range, its reduction reflected an increase in the double-layer

capacitance after surface modification. At high frequencies, the capacitive impedance became so low that the spreading resistance R_s dominated. The impedance was then resistive and independent of the frequency.

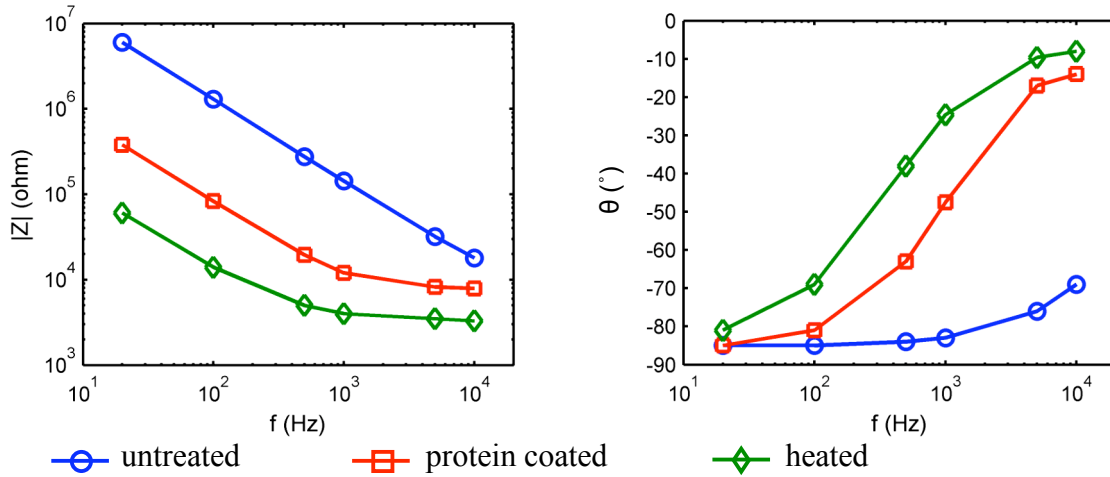


Figure 3.13 Bode plot of the impedance spectra of $70 \mu\text{m} \times 70 \mu\text{m}$ CNT electrodes in PBS at zero bias. The circles represent an untreated device; the squares are data from the same device after incubation with protein-containing culture media; the diamonds represent another device right after thermal oxidation.

3.5.3 Data Analysis

The capacitance of untreated CNT electrodes of different sizes was extrapolated from the EIS spectra (equation 3.22), and then plotted versus their geometrical area (Figure 3.14). The geometrical area was calculated, including both the top and the sidewalls of the CNT pillar. The fitted slope was $5.4 \times 10^{-14} \text{ F}/\mu\text{m}^2$, i.e., C_d was $5.4 \mu\text{F}/\text{cm}^2$ for untreated hydrophobic CNT electrodes. This is in good agreement with the capacitance of the graphite basal plane (see Section 3.1.1.2). The capacitance was proportional to the total geometrical area, indicating that in hydrophobic CNT electrodes, both the top and the sidewall contributed to the capacitive current in a similar way.

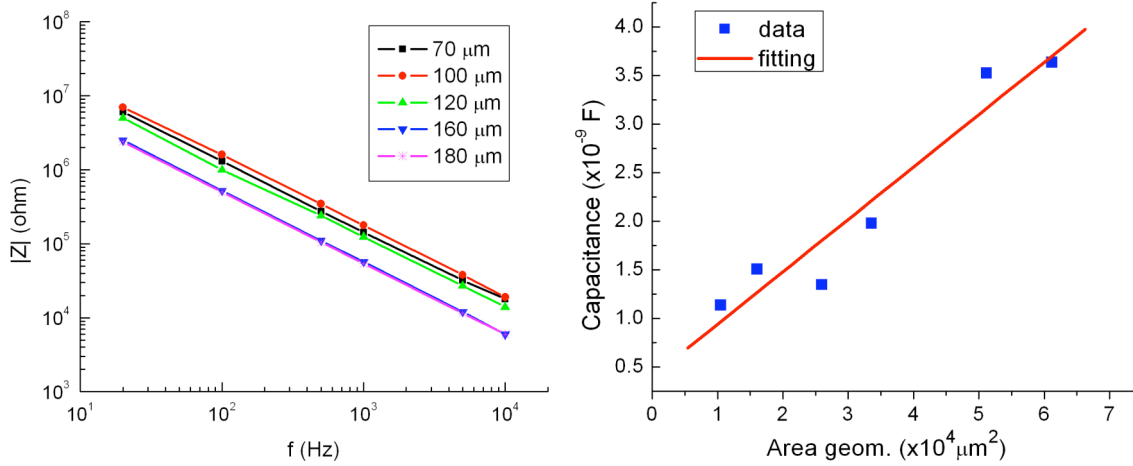


Figure 3.14 Left: Bode plot of untreated CNT electrodes of different sizes. Right: The total capacitance increases linearly with the total geometrical area for these untreated electrodes.

For modified CNT electrodes (the thermally oxidized shown as example), the capacitance was calculated from the linear part of the EIS spectra, and then plotted versus the size of the electrodes (a , the edge width of the base) (Figure 3.15). The relation between C_d and a can be written as:

$$C_d = C_d^*(R_1 a^2 + R_2 \cdot 4ah) \quad (3.23)$$

where C_d^* represents the specific capacitance (real surface area), which is 5-10 $\mu\text{F}/\text{cm}^2$ for the graphite basal plane. Oxidized CNTs may have a higher C_d^* because of the increased number of surface oxide groups on both the tip and the wall. The height of the pillar, h , equals to 40 μm in this device, and is uniform for different electrode sizes; R_1 and R_2 are the roughness factors of the top and the sidewall of the CNT pillar, respectively. A parabolic fitting of the plot resulted in $R_1 = 250\text{-}500$, and $R_2 = 50\text{-}100$. Unlike hydrophobic electrodes, the surface area of the top and the sidewall of modified CNT pillars contributed to the capacitance with different weighing factors. From SEM images (Figure 3.16), we can see that the top of the pillar has indeed a rougher surface morphology than the sidewall. Another reason that may have contributed to this

inequality is the abundance of CNT tips at the top surface of the pillar. The fullerene-like tip of a nanotube is known to be more reactive than the wall, therefore probably has a higher specific double-layer capacitance. For the hydrophilic electrodes, the water molecules are closer to the electrode surface and these inequalities can be manifested in the electrochemical data.

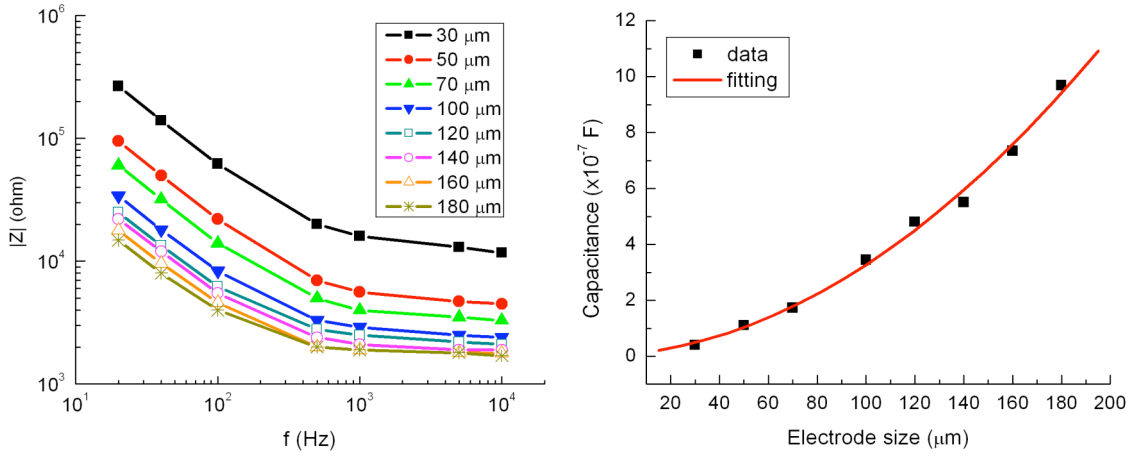


Figure 3.15 Thermally oxidized CNT electrodes of different sizes. Left: Bode plot of the EIS data. Right: parabolic dependence of the capacitance on the electrode size.

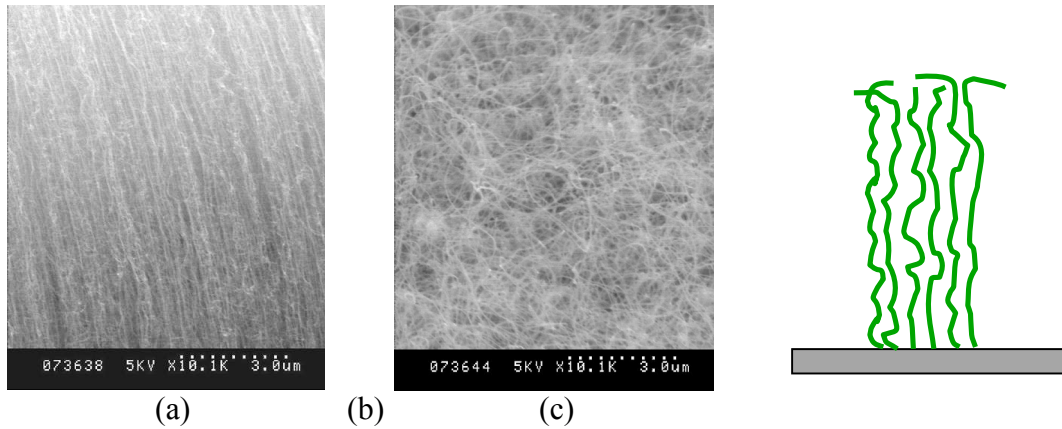


Figure 3.16 The sidewall (a) and the top (b) of a CNT pillar. The nanotubes in a pillar are only quasi-aligned. Instead of an array of needle-like sharp tips, the top surface is a mixture of interlaced nanotube ends and walls at all orientations (c).

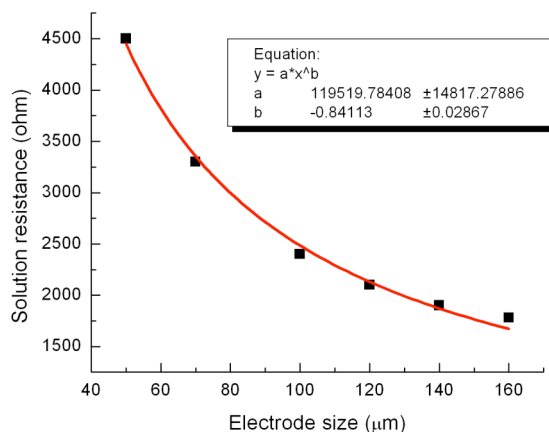


Figure 3.17 Spreading resistance for electrodes of different sizes.

The resistive impedance at 10 kHz is also plotted versus the electrode size (Figure 3.17). From the calculations in Chapter 2, the resistance of the poly-silicon leads should be only about 200 Ω (the traces are all of a uniform size). The impedance is thus primarily the spreading resistance, R_s , of the solution. The curve can be fit to:

$$R_s = \frac{1.2 \times 10^5}{a^{0.84}} \quad (3.24)$$

with a in micrometers. The resistivity of PBS is on the order of $10^5 \Omega \cdot \mu\text{m}$. Since the geometrical area $A = a^2 + 4ah$, R_s is approximately proportional to \sqrt{A} . Hence the fitting is in good agreement with the theoretical model (Section 3.1.3).

3.6 Potential Transient Measurement

The charge injection limit is defined as the maximum quantity of charge that an electrode can inject before reaching the water electrolysis potentials. It directly determines the minimal size of the electrode that can be used safely. The charge injection limit was determined experimentally by potential transient measurements. A symmetric biphasic current pulse was applied between a CNT electrode and an Ag/AgCl coil in PBS. The

electrode potential excursion was monitored on a digital oscilloscope with a 10× probe. The injected charge was increased gradually (by increasing the amplitude and/or the duration of the current pulse) until the electrode potential reached the hydrolysis limit.

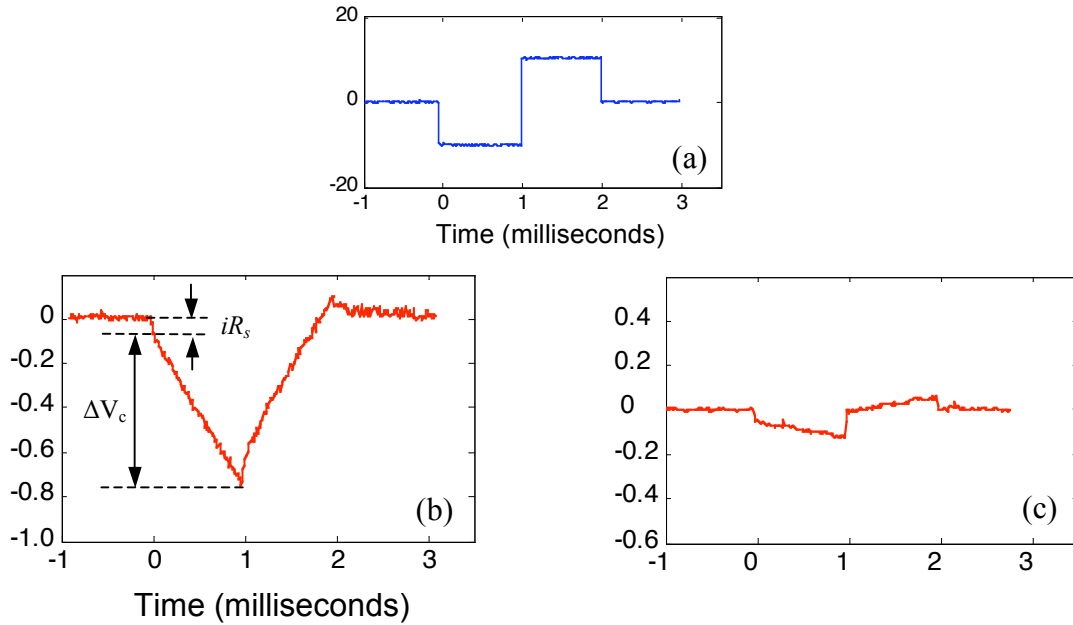


Figure 3.18 Potential transient of a CNT electrode (geom. area = $5 \times 10^{-4} \text{cm}^2$) under a $10 \mu\text{A}$, 1 ms biphasic current pulse (a), before (b) and after (c) surface modification.

The voltage transient of a CNT electrode (geom. area = $5 \times 10^{-4} \text{cm}^2$) in response to a $10 \mu\text{A}$, 1 ms symmetric biphasic current step is shown in Figure 3.18. The initial voltage step is due to the ohmic resistance of the solution: $\Delta V_R = iR_s$. Then the potential changes almost linearly with time, reflecting the charging and discharging of the double layer capacitor: $\Delta V_c = \frac{it}{C_d}$. This provides another method to estimate the double-layer capacitance, although C_d is actually a variable of the potential and a more precise description should be: $\int idt = \int C_d(V)dV$. Figure 3.18c is the voltage transient of the same electrode under the same current pulse, but after surface modification. Since C_d is

much larger for hydrophilic CNT electrodes, ΔV_c is much smaller than the untreated case. In other words, the electrode can inject the same amount of charge at a much lower potential. This means that more charge can now be injected safely.

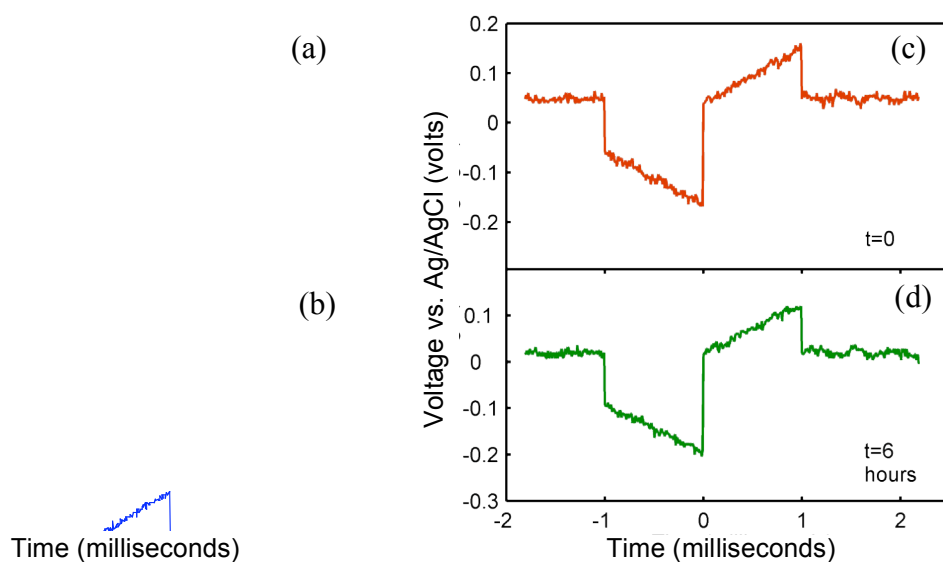


Figure 3.19 Charge injection limit and durability. (a) Voltage excursion of a functionalized CNT electrode (geom. area = $5.7 \times 10^{-5} \text{ cm}^2$), under anodic-first symmetric biphasic current pulses ($80 \mu\text{A}$, 1 ms) and (b) with R_s subtracted. (c) and (d): the same electrode under continuous 10 Hz pulsing ($20 \mu\text{A}$, 1 ms, biphasic) for 6 hours. There was no change in the potential transient curve.

The charge injection limit of a functionalized CNT electrode (geom. area = $5.7 \times 10^{-5} \text{ cm}^2$) can be determined from Figure 3.19. The ohmic voltage drop ΔV_R does not occur at the electrode surface and does not need to be taken into consideration for electrochemical safety. After subtracting ΔV_R , the resulting saw tooth curve (Figure 3.19b) presents the potential at the electrode surface. When the current pulse was increased to $80 \mu\text{A}$, the potential reached the hydrolysis limit ($+1.0\text{V}$ vs. Ag/AgCl for oxygen evolution). This defined the charge injection limit of this functionalized CNT electrode to be 1.6 mC/cm^2 geom.

To test the durability of the CNT device, the microelectrodes were pulsed (20 μ A, 1ms, biphasic) at 10Hz continuously for 6 hours. No change was observed in the potential transient curves (Figure 3.19c and d).

Table 3-2 Electrochemical properties of several neural electrode materials

	CNT	Bare Pt	IrOx
Potential window (volts)	2.5	1.5	1.5
Charge injection limit (mC/cm ²)	1-1.6	0.1-0.3	2-3
Charge injection mechanism	capacitive	faradaic pseudo-capacitive	faradaic

A summary of the electrochemical properties of CNT, bare Pt and IrOx is listed in Table 3-2. The charge injection ability of treated CNT electrodes is much higher than bare platinum (0.1-0.3 mC/cm²), but still not as high as iridium oxide (2-3 mC/cm²). However, the large surface area of CNTs has not yet been fully exploited. For an aqueous electrolyte, pores as small as 0.5 nm should be sufficient to contribute to double-layer capacitance [49]. If the entire surface of each nanotube could be accessed, the theoretical limit of roughness factor should exceed 10³, much higher than the current values (~10²). By tailoring the synthesis and surface modification techniques, we believe that a higher charge injection limit can be reached. On the other hand, since the damage threshold for biological tissues is around 1 mC/cm² [9], practically it is not necessary to increase the electrode charge injection limit much further. The stimulation threshold for retinal ganglion cell is below 1 nC when the electrode is in good proximity [50, 51]. So the minimal size for a CNT electrode can be reduced below 10 μ m, while enough current can still be injected without adverse electrochemical effects. This is approximately the size of the retinal ganglion cell soma, and is considered a preferable size for stimulating electrodes in retinal prostheses, one of the most demanding neural prosthetic fields.

3.7 Summary

- A theoretical model of processes at the electrode-electrolyte interface was described. Charge can be injected either through faradic reactions or capacitively between the two phases. Capacitive current is preferred for neural stimulation.
- The electrochemical properties of the CNT microelectrode array were characterized using cyclic voltammetry, impedance spectroscopy and potential transient measurements.
- The CNT microelectrodes have a wide electrochemical operational window (2.5 volts), and they operate mainly capacitively. The equivalent circuit of the system is simply a double-layer capacitor in series with the solution resistance.
- CNTs are highly hydrophobic. However, the surface can be modified to improve the hydrophilicity. Both thermal oxidation and non-covalent functionalization (adsorption of phospholipids or proteins) can be used to modify the CNT microelectrodes. The latter is a preferred treatment that better preserves the device structure.
- The ac impedance of CNT electrodes was reduced by two orders of magnitude after surface modification. The interfacial capacitance was $5.4 \mu\text{F}/\text{cm}^2$ geom. for as-grown hydrophobic CNT electrodes, and reached a value as high as $1600 \mu\text{F}/\text{cm}^2$ geom. after surface treatment.
- Both the top and sidewall of CNT electrodes contributes to the capacitive current injection. For hydrophilic electrodes, the surface area of the top and sidewall should be counted with different weighing factors.
- The charge injection limit of treated CNT electrodes was $1\text{-}1.6 \text{ mC}/\text{cm}^2$, far better than bare Pt and comparable to iridium oxide.

Chapter 4

In Vitro Neuronal Culture on CNT

In recent years, there has been an increasing interest in the toxicological study of CNTs, primarily driven by their potential applications in drug delivery [20, 52-54]. Nevertheless, the understanding of how CNTs interact with biological systems on a cellular level is still at its beginning stage. Most of these studies focus on single-walled CNTs dispersed in water, reporting different opinions on their cytotoxicity and biocompatibility [55-58]. In comparison, less work has been done on the interaction between cells and multi-walled CNTs, or CNTs immobilized on substrates [59, 60].

As described in Chapter 2, the surface of as-grown CNTs has been analyzed by X-ray photoelectron spectroscopy. It was shown to be chemically non-toxic, consisting primarily of carbon and only traces of oxygen. In order to further evaluate the biocompatibility of these assembled CNTs, an in vitro neuronal culture was performed as a primary investigation.

4.1 Overview of Adherent Neuronal Culture

After being isolated from tissues, animal cells can continue to grow if supplied with appropriate nutrients and conditions (such as temperature, humidity, pH, O₂ and CO₂ concentrations). Mammalian cells can be grown either in an unattached suspension culture or attached to a solid surface. There are two basic requirements for the survival and proper growth of adherent neuronal cultures: substrates and neurotrophic factors [61].

Neurotrophic factors are a family of polypeptide growth factors that promote neuronal survival, growth, and especially differentiation. NGF (Nerve Growth Factor), BDNF (Brain-Derived Neurotrophic Factor), CNTF (Ciliary Neurotrophic Factor) are among the most well-known ones. Neurotrophic factors are usually added to the cell culture media as supplements. Without them, the neurons will degenerate or fail to fully differentiate.

Traditional substrates used for cell culture are glass (“in vitro” literally means “in glass”) and plastic (polystyrene or polypropylene). The substrates are usually treated to attract, or at least allow the cells to adhere and grow on the surface. In fact, cells directly interact with a thin layer (a few hundred of angstroms thick) of adsorbed proteins and macromolecules on the surface, instead of with the materials of the bulk substrate. A widely used coating for neuronal culture is polylysine, a synthetic peptide polymer. One of the mechanisms through which polylysine promotes neural adhesion and growth is electrostatic interaction. The natural surface of glass or tissue culture plastic is negatively charged, and the net charge on the cell membrane is also negative. Therefore, the positively-charged amine group of polylysine can bond onto the substrate and attract the cells to adhere. Polylysine can also promote cell growth by enhancing protein adsorption. Some disadvantages of polylysine include: cytotoxicity at high concentrations [62] and being nonphysiological.

Besides polylysine, many other biomolecules are often used to prepare the surface for neuronal culture. Cells adhere to the substrate surface in a similar way as they adhere to other cells in the tissue, involving receptor-based binding to the extracellular matrix (ECM). Transmembrane adhesion proteins (known as integrins) bind to both the cytoskeleton in the intracellular space, and ligands in the ECM such as fibronectin, vitronectin and laminin. After binding, specific adhesion sites known as *focal contacts* or *adhesion plaques* are formed. The coupling between integrins and ECM is critical to adherent neuronal culture. It not only enables the cells to attach to the substrate, but also supplies the cell with signals from the surrounding environment and modulates cellular behavior including attachment, movement, differentiation and death. Therefore, if the

cells can not synthesize their own ECM molecules in a relatively short time, it is often essential to coat the substrates with these proteins. [63]

Artificial surface conditions can also be created using techniques such as self-assembled monolayers (SAM) [64]. This is beyond the scope of this thesis and will not be discussed here.

4.2 Cell Preparation

A major criterion in the cell type selection for this work is the electrical excitability. Because of their rapid proliferation rate and ease of culture, cell lines were first considered. Unfortunately, very few cell lines are electrically excitable. One of them is a neuroblastoma × glioma hybrid (NG108-15), which has some neuron-like behavior and expresses voltage-sensitive ion channels including Na^+ , K^+ and Ca^{2+} . The NG108-15 cells (ATCC, VA) proliferate well when cultured in a serum-containing medium (Figure 4.1a). But if they are cultured in a serum-free medium, supplemented with HAT (Invitrogen, CA), the cells stop proliferation and start to differentiate (Figure 4.1b). Along with the significant change in morphology, the electrophysiological properties of the cells are also different. The cells can fire action potentials when stimulated electrically or chemically (by acetylcholine or bradykinin). However, even under optimized culture conditions, the percentage of cells which can fire action potentials under electrical stimulation is still quite low. In experiments with the purpose of testing the CNT electrodes, it will be difficult to identify whether the lack of response originates from a problem in the electrode or from the poor activity of the cell. Therefore, cell lines like NG108-15 are inappropriate for this work, and primary neurons (cells freshly isolated from animal tissues) are needed.

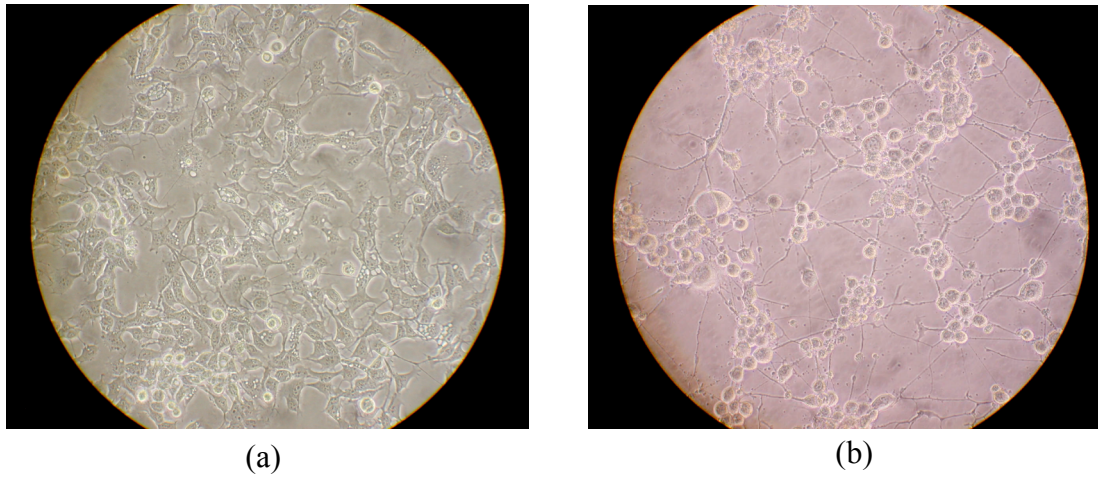


Figure 4.1 NG108-15 cells cultured on Petri dishes. (a) Cells cultured in serum-containing media. (b) Cells stop proliferation and start to differentiate when cultured in serum-free medium with HAT supplement (Invitrogen, CA).

4.2.1.1 Retinal Ganglion Cell

Since retinal prosthesis is one of the major target applications of this work, retinal ganglion cells (RGCs) were chosen as a model for in vitro tests. RGCs from P7 Sprague-Dawley rats (Simonsen Laboratories, CA) were isolated and purified, based on methods previously described [65, 66]. Using sequential antibody mediated plate adhesion (“panning”), RGCs were isolated to > 99.5% purity. Detailed protocol is listed in Appendix B.

The primary antibody is T11D7, an IgM antibody against the Thy-1 antigen expressed by rat RGCs. However, RGC is not the only retinal cell type that expresses Thy-1. Therefore, a two-step panning needs to be used, in which other Thy-1-positive cell types (mostly macrophages) are first removed by a secondary antibody: affinity-purified goat anti-rabbit IgG.

Freshly dissected retinas were enzymatically digested in a papain solution. After incubation, the retinas were dissociated by trituration in a solution containing rabbit anti-

rat-macrophage antiserum. The retinal suspension was further incubated in this solution to allow the antimacrophage antibodies to bind the macrophages and was then centrifuged. The cells were suspended and then incubated on an anti-rabbit IgG panning plate to allow the labeled macrophages to bind onto the plate. The non-adherent cells were transferred to a second anti-rabbit IgG panning plate and incubated again. Next, the suspension was transferred to a monoclonal T11D7 panning plate, to separate RGCs from the rest of the cells.

The adherent RGCs were released from the panning dish by incubation in trypsin. A fetal calf serum solution was used to inactivate the trypsin, and the cells were dislodged by gently pipetting the solution around the plate. The cells were then centrifuged and resuspended in RGC growth medium for plating.

4.2.1.2 Hippocampal Neuron

The preparation of RGCs is complex, expensive and very time-consuming. There is also large variation in the cell condition from different preparations, as an inevitable result of the harvest process, which is as much of an art as a science. A convenient, cost-effective substitute is the hippocampal neuron. Embryonic rat hippocampus tissue can be purchased (Brainbits, Springfield, IL) and shipped in Hibernate™, a modified Neurobasal medium that can keep neural tissues alive for up to a week in ambient carbon dioxide under refrigeration [67]. Both the preparation and the culture are much less complex than the RGCs (see Appendix C). The preparation involves only dissociating (by trituration), centrifuging and suspending. Hippocampal neurons can be harvested from the tissue in less than 20 minutes. Cells are then cultured in a serum-free medium supplemented with B27, in which the glial growth is minimized [68]. The only drawback is that the cell viability is usually lower than RGCs harvested from fresh retinas.

4.3 Substrate Preparation

Both unpatterned CNT mats (Figure 4.2a and b) and patterned CNT pillars were used as substrates in the cell culture experiments. Since as-grown CNT mats were highly hydrophobic and tended to float when immersed in water, the chips were first glued to Petri dishes with cured PDMS. To conserve cells and culture media, an acrylic ring was also glued to form a small chamber around each chip. Each Petri dish contained several such chambers (Figure 4.2c), so results on different substrates could be compared when all other conditions were identical. Conventional multi-well plates were not used because their wells were too deep for the working distance of the upright microscope used to examine cell growth.

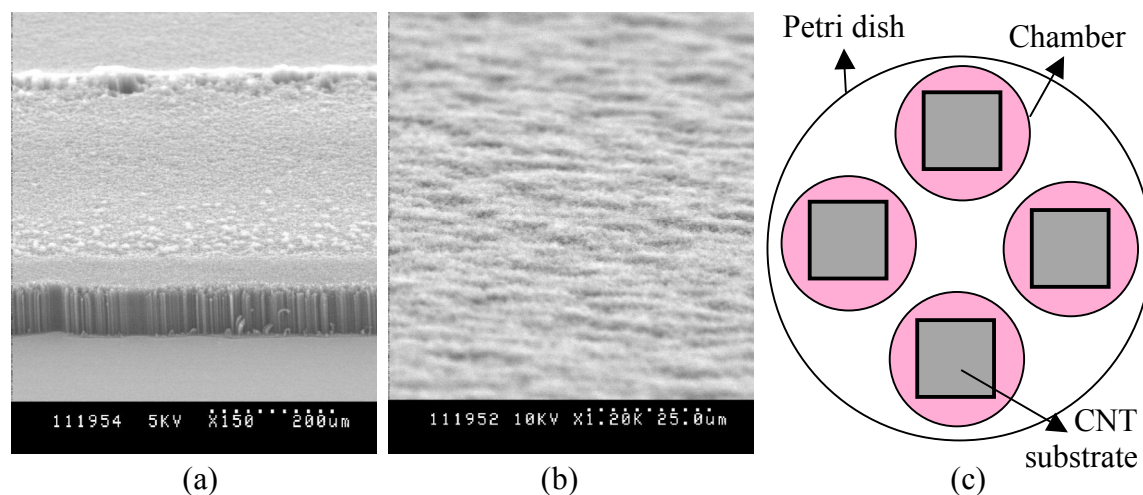


Figure 4.2 CNT substrates for in vitro cell culture. (a) SEM image of a CNT mat. (b) A close-up view of the top surface of the CNT mat. (c) An illustration of the multiple cell culture chambers in a Petri dish.

4.3.1.1 Sterilization

The CNT substrates were first sterilized by soaking in 70% ethanol. The ethanol soak served two purposes in one step: sterilization and improvement in hydrophilicity (see Section 3.4). However, it was noticed that the cell viability dropped significantly on

CNT mats grown at lower temperature, as well as on thermally oxidized CNT mats. It was suspected that ethanol residues might have been trapped in the pores of the CNTs, even after extensive rinsing. The quasi-planar structure grown at low temperature (see Figure 2.13) and the heated samples were more porous than untreated CNTs grown at 700°C, thus more ethanol was trapped in these samples and caused cell death. The suspicion was proved by an increase in cell viability when the CNT substrates were sterilized by UV exposure instead. The results are shown in Section 4.4. Therefore, UV exposure is a more suitable method to sterilize the CNT substrates.

4.3.1.2 Surface modification

As stated in Chapter 3, a number of biomolecules can spontaneously adsorb onto the CNT surface through non-covalent interactions. This non-specific adsorption provides the possibility of designing the surface to meet specific surface requirements, such as promoting cell adhesion and growth, in addition to improving hydrophilicity. Tests were performed to understand whether commonly used adhesion factors and extracellular matrix molecules could be used to make CNT a more supportive substrate for neuronal growth.

To examine their adsorption, poly-D-lysine (Sigma), laminin (Invitrogen) and fibronectin (Sigma) were first tagged with FITC (see Appendix A) and then incubated with the CNT pillar arrays. Final incubation concentration was 10-50 nM in PBS, overnight at 37°C except for poly-D-lysine (room temperature). The CNT samples were then well rinsed and examined with confocal microscopy as described in Chapter 3. The results are shown in Figure 4.3. Because of the various mechanisms involved, these molecules also adsorbed to the silicon dioxide surface, increasing the background fluorescence level.

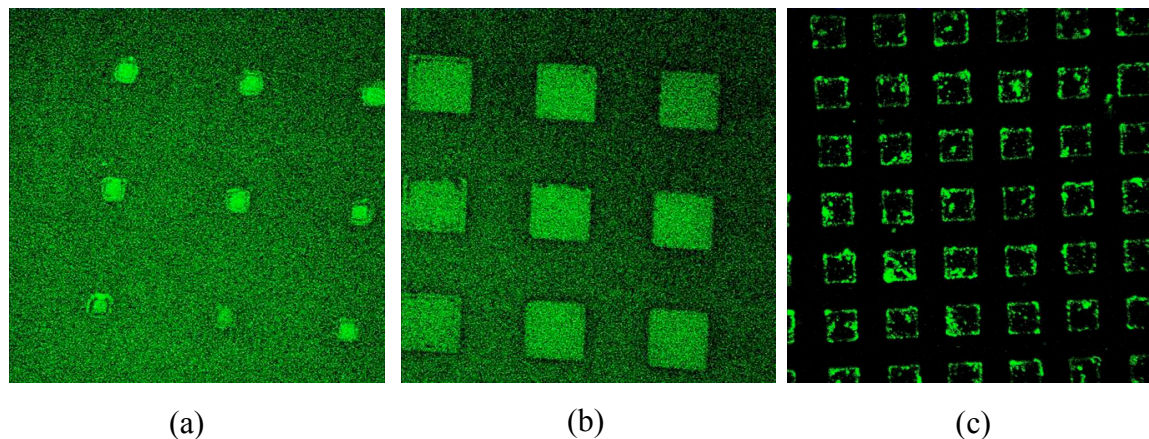


Figure 4.3 Confocal images of CNT pillars after incubation with FITC-labeled molecules. (a) as-grown pillars with laminin; (b) as-grown pillars with fibronectin; (c) thermal-oxidized pillars with poly-D-lysine.

Both laminin and fibronectin adhered uniformly on the CNT pillars. The bonding remained stable for at least several days. Poly-D-lysine did not adsorb onto as-grown CNT pillars, while some adsorption did occur on oxidized CNTs. This may be explained by the electrostatic nature of poly-lysine adsorption (Section 4.1). As-grown CNTs are electrically neutral, while oxidized ones have a net negative charge and may better attract poly-lysine to adsorb.

After surface modification, the CNT substrates were incubated in Neurobasal media (without supplements) overnight before cells were plated. The incubation further conditioned and outgassed the surface, releasing any substance entrapped during the fabrication processes.

In summary, the preparation of unpatterned CNT mat substrates is:

1. Glue the CNT substrates to Petri dishes with cured PDMS.
2. Sterilize by overnight UV exposure.
3. Rinse two to three times with sterile DI water.

4. Incubate the substrates with desired biomolecules.
5. Rinse with water or PBS.
6. Soak the substrate in Neurobasal overnight at 37°C before plating the cells.

4.4 Results

Since CNTs are neither transparent nor reflective in the visible wavelengths, conventional upright or inverted light microscopy can not be used to assess the cell growth on these substrates. Instead, fluorescence assays were employed, complemented by electron micrographs. Like most primary neuronal culture, the RGCs and hippocampal neurons have a limited life span. They differentiate, but do not divide. Their viability was evaluated by their ability to adhere, to grow neurotic processes, as well as their intracellular enzymatic reactions and physiological activities (Section 5.4.1).

4.4.1.1 Live/Dead Stain

Cell viability can be visualized by a two-color fluorescence assay called LIVE/DEAD (Invitrogen, Molecular Probes, CA), which contains two dyes: calcein AM and ethidium homodimer (EthD-1). When incubated with the cells, the hydrophobic AM ester groups diffuse into the membrane and bring the calcein molecules inside the cell. In live cells, the non-fluorescent calcein AM is converted to the intensely fluorescent calcein by the ubiquitous intracellular esterase activity. Without the AM ester group, the calcein is far less membrane-permeant and is well retained within the cell. Therefore both the somas and neurites of live cells are stained by an intense uniform green fluorescence (ex/em ~494 nm/~517 nm). EthD-1 is excluded by intact plasma membrane, but enters damaged membrane and the fluorescence (ex/em ~528 nm/~617 nm) increases 40 times upon binding with the nucleic acids. Thereby the nuclei of the dead cells are stained bright red.

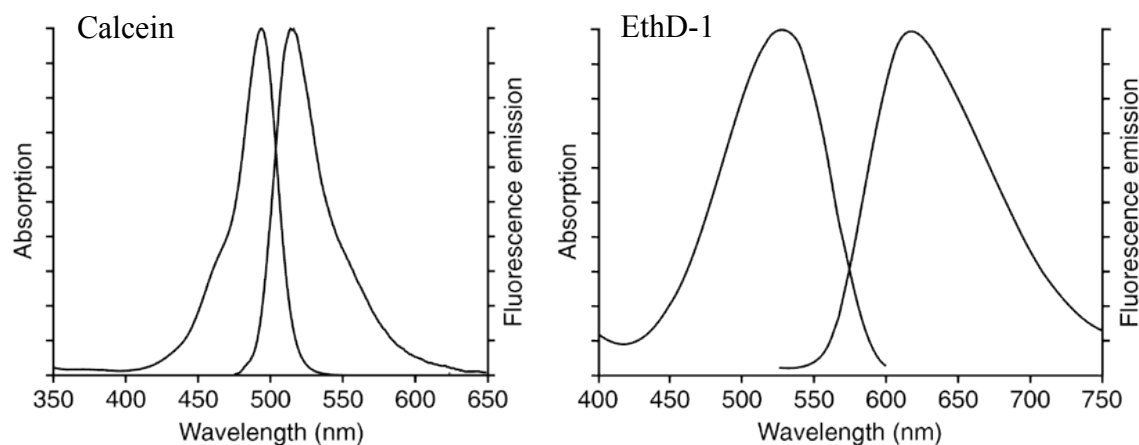


Figure 4.4 The absorption and emission spectra of LIVE/DEAD dyes. Left: Calcein. Right: EthD-1. *Source: Molecular Probes.*

LIVE/DEAD assay is a powerful tool for cell viability assessment with excellent signal-to-noise ratio. Background fluorescence level is very low since both dyes are virtually non-fluorescent before interacting with the cells. However, the determination of cell viability depends on the enzymatic esterase activity of cells. Therefore, cytotoxic events that do not affect these cell properties may not be accurately assessed using this method.

The loading process is described in Appendix D. After loading, fluorescence images were taken with an upright confocal microscope, consisting of a Nikon E800 (objectives: x10 with 0.30 numerical aperture, or x40 with 0.80 aperture) and a Nikon PCM 2000 confocal unit. A 488 nm argon laser was used to excite both dyes, and two-color images were simultaneously sampled by using two photomultiplier tubes (515/30 bandpass and 605/32 bandpass filters) (see the spectra for both dyes in Figure 4.4). The images were acquired and analyzed with SIMPLEPCI software (Compix, Cranberry Township, PA).

Figure 4.5 shows the LIVE/DEAD stain of hippocampal neuron growth on unpatterned CNT mats with different sterilization methods, but with no pre-coating of any protein or other molecules. The substrates were either soaked in 70% ethanol overnight followed

by repeated rinsing in sterile DI water, or exposed under UV light overnight. Afterwards, the substrates were soaked in Neurobasal overnight, and then hippocampal neurons were plated. As shown in Figure 4.5, almost no cells survived on the ethanol-sterilized CNT substrates, while cells could adhere and grow on ethanol treated Petri dish controls (image not shown here). In comparison, the cell viability was much higher on UV-sterilized CNT substrates, with continual neurite outgrowth. These results confirmed the concern that ethanol could be trapped between the porous CNTs, even after extensive rinsing, and be detrimental to the cells. It also indicated that UV exposure was an effective way to sterilize the CNT substrates.

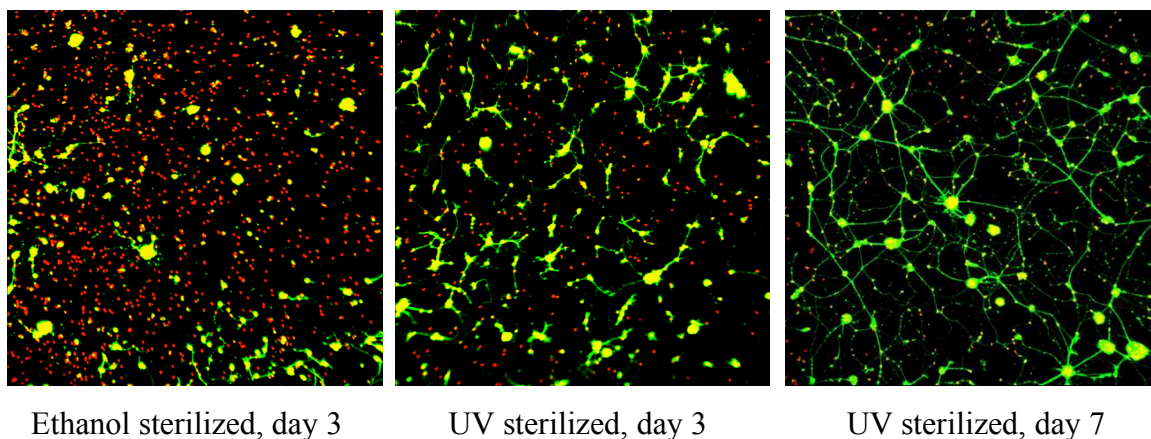


Figure 4.5 Live/dead stain of hippocampal neuronal culture on CNT mats sterilized with ethanol and UV exposure. The substrates were not coated with any protein or other molecules.

Although there was a considerable improvement in cell viability for UV-sterilized CNT substrates, the neurite outgrowth (characterized by the length and the number of the neurites) was still relatively slow. This slow growth was also observed in Petri dish control cultures with no coating. Significant increase in cell adherence and neurite outgrowth was obtained on CNT substrates coated with PEG-PL, laminin and fibronectin (Figure 4.6). Laminin and fibronectin are both ECM proteins, and are

known to promote neurite outgrowth. Thus it was expected that the cells would develop extensive neural network on substrates coated with these molecules. But surprisingly, excellent cell adherence and differentiation were also observed on CNT substrates coated with PEG-PL, despite that the PEG tail was known to repel protein adsorption [69]. One feasible explanation was that the cell adhesion and growth was promoted by the improved hydrophilicity of CNT after PEG-PL coating. It was also possible that the large number of nanotubes on the rough surface provided more adhesion sites for the cells.

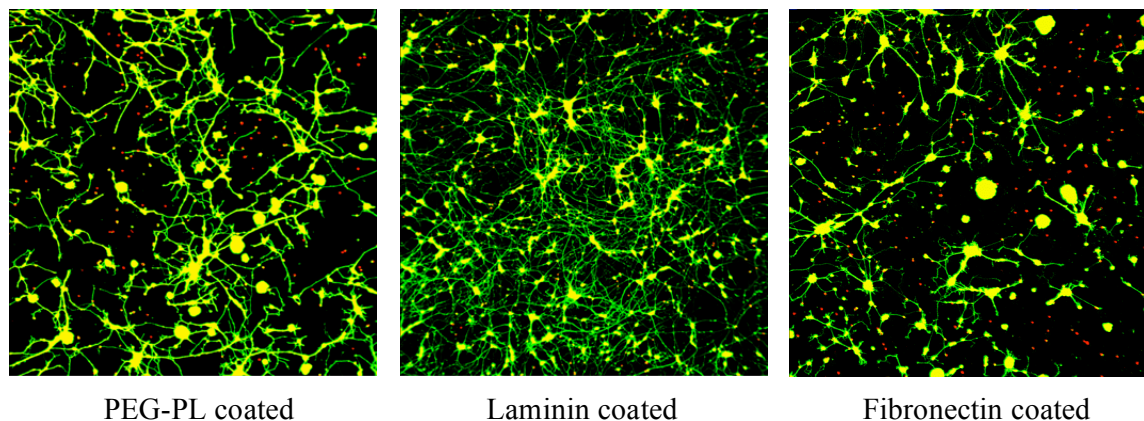


Figure 4.6 Live/dead stain of hippocampal neuronal cultures (day 3) on CNT substrates with different pre-treatments.

The continual growth of RGC on laminin coated CNT substrates over a 9-day period was recorded in Figure 4.7, imaged every three days. The cells started differentiation as early as day 1, and continued to grow during the entire observational period. An interesting phenomenon was that when the cells were cultured on silicon substrates with patterned CNT pillars, many of the pillars were “outlined” in the fluorescence image (Figure 4.8). The origin of this “outlining” would become more clear in the next Section.

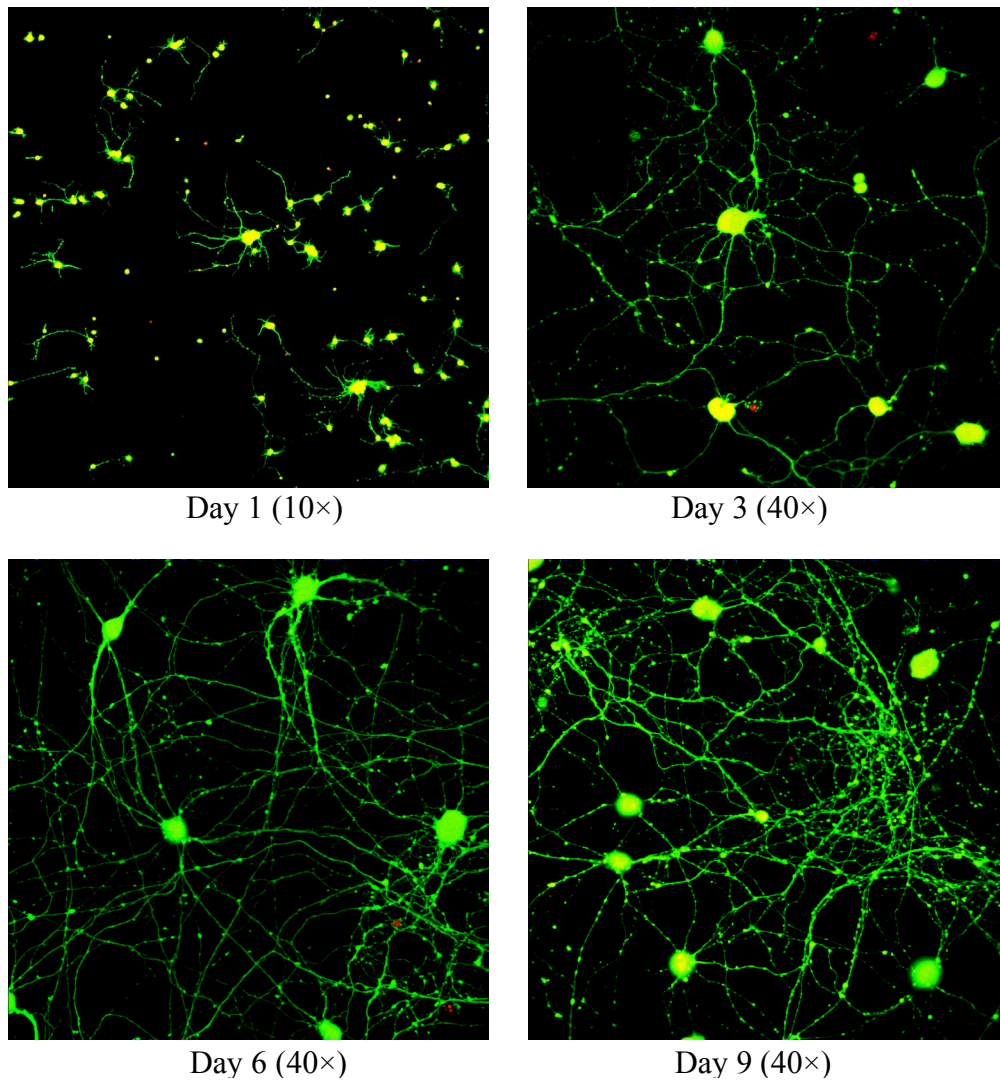


Figure 4.7 Continual growth of RGCs on unpatterned CNT substrates over a 9-day period, imaged every three days. LIVE/DEAD stain.

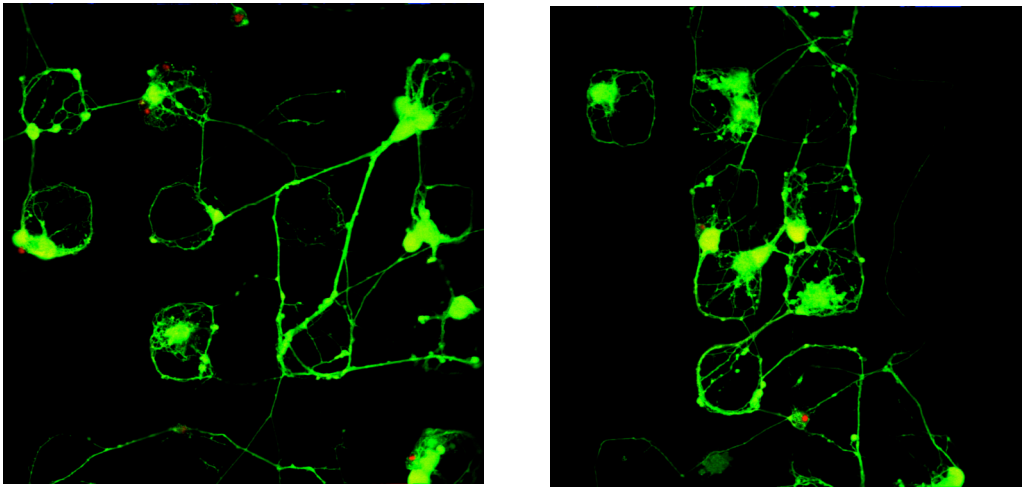


Figure 4.8 RGCs cultured on a silicon substrate with a CNT pillar array. Many of the CNT pillars were “outlined” by stained neurites in the fluorescence images. Day 3, 40 \times , LIVE/DEAD stain.

4.4.1.2 SEM Images

After confocal imaging, the cells were immediately fixed and prepared for SEM imaging (see Appendix E for detailed protocol). Some of the SEM images are displayed in Figure 4.9. The cells could grow and differentiate on the top of CNT pillars or unpatterned CNT mats. Another interesting observation was that many cells had their neurites climbing like ivies along the sidewalls of the CNT pillars (Figure 4.9d and e). This proved that the “outlining” in Figure 4.8 was caused by neurites growing along and around the CNT pillars. It also suggested that both the top and the sidewall of these pillars could support neuronal growth. In some cultures on CNT pillar arrays, the cells grew into a 3D matrix (Figure 4.9f), closer to their natural status in the tissue than the usual monolayer cultured on a smooth planar substrate (such as a Petri dish). Therefore, there are possibilities that the CNT pillars may be used as scaffolds in tissue engineering, to restore or reinforce damaged or weakened tissues.

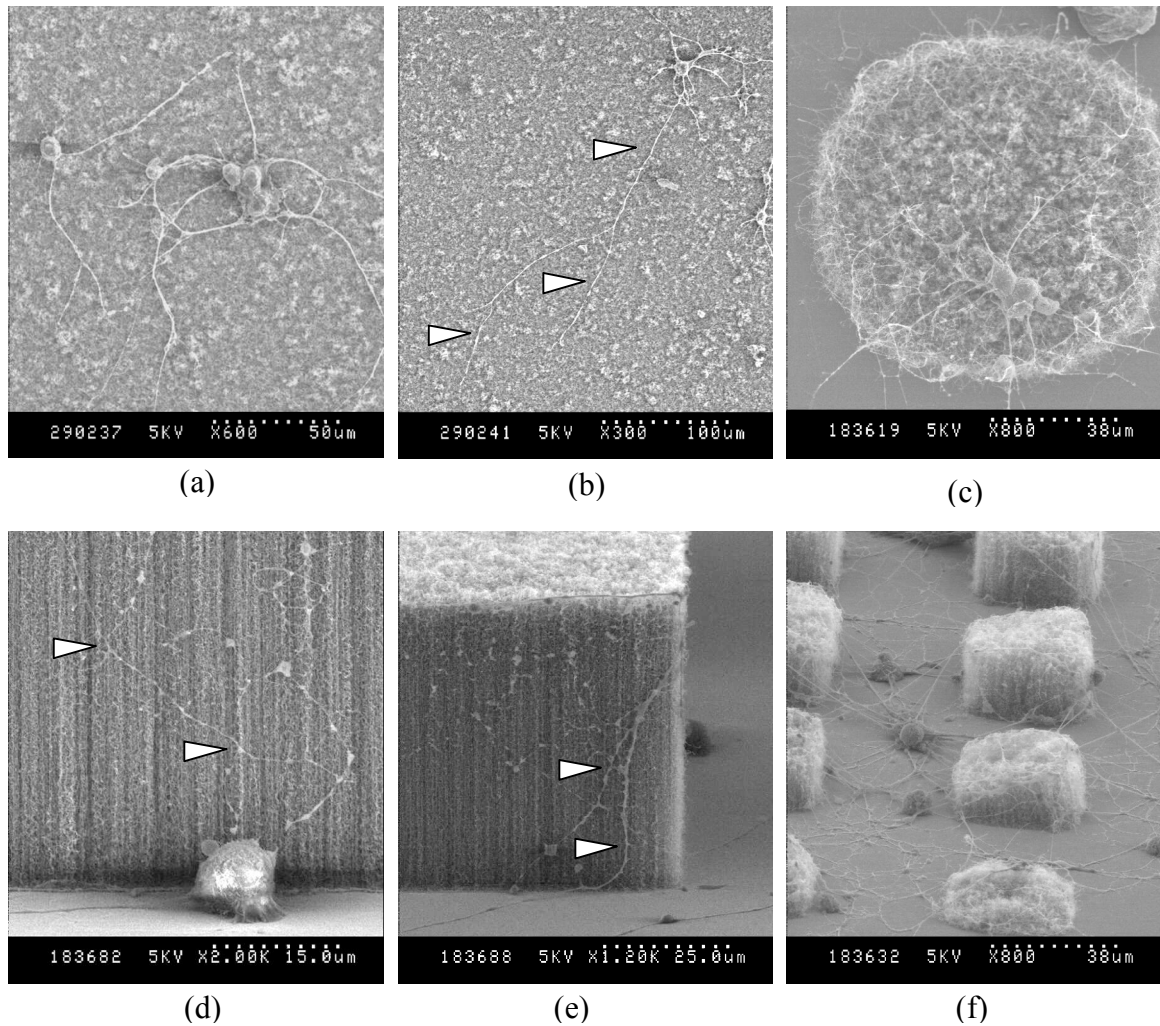


Figure 4.9 SEM images of RGC cultures on CNT substrates. (a) and (b): cells on top of unpatterned CNT mats, day 1. (c)-(f): cells on silicon substrates with CNT pillars, day 3. The arrowheads point to some of the neurites. (b): a very long neurite growing out from a cell. (c): cells growing on the top of a CNT pillar. (d) and (e): cells and neurites growing on the sidewalls of CNT pillars. (f): cells growing into a 3D matrix with an array of CNT pillars.

4.4.1.3 Statistical Results

In order to analyze the cell culture results in a more quantitative way, cell counting and measuring were performed with the LIVE/DEAD fluorescence images using MetaMorph

software (Molecular Devices, Sunnyvale, CA). Three key parameters were calculated: the cell viability, the average neurite length, and the average number of neurites per cell. The results of the hippocampal cells are presented in Figure 4.10. Each column is an average of results from three different culture samples. For each sample, three neighboring but not overlapping regions were imaged and included in the calculation.

The cell viability was defined as:

$$\text{Viability} = \frac{\text{\# of live cells}}{\text{\# of live cells} + \text{\# of dead cells}} \times 100\% \quad (4.1)$$

The viability of the hippocampal neurons was generally low, presumably because the cells were not harvested until a day or two (time needed for shipping and handling) after the dissection. Hemocytometer counting was performed immediately after the preparation, and the viability of the harvested cells was already lower than 60% at that stage. Both live and dead cells were plated, and some of the dead cells (percentage unknown) would also adhere to the substrate. Those not adhered were usually washed away during either dye loading or media change processes. Therefore, the absolute value of the cell viability obtained from LIVE/DEAD assay was not an accurate evaluation of the culturing conditions, such as the relative biocompatibility of the substrate. A more reasonable approach was to compare cultures on the CNT substrates to Petri dish controls with identical treatments.

The data showed that there was little difference in cell growth between laminin-coated CNT substrates and Petri dishes. In both cases, cell viability was very high and there was extensive neurite outgrowth. The cell growth on Petri dishes were not significantly affected whether the dishes were sterilized with ethanol or UV, and coated with PEG-PL or not. This was likely due to the low adsorption of PEG-PL on Petri dishes. However, these surface treatments had an appreciable impact on cultures on the CNT substrates. In fact, cells on either uncoated or PEG-PL coated CNT substrates (with UV sterilization)

showed even better viability and outgrowth than their counterparts cultured on the Petri dishes.

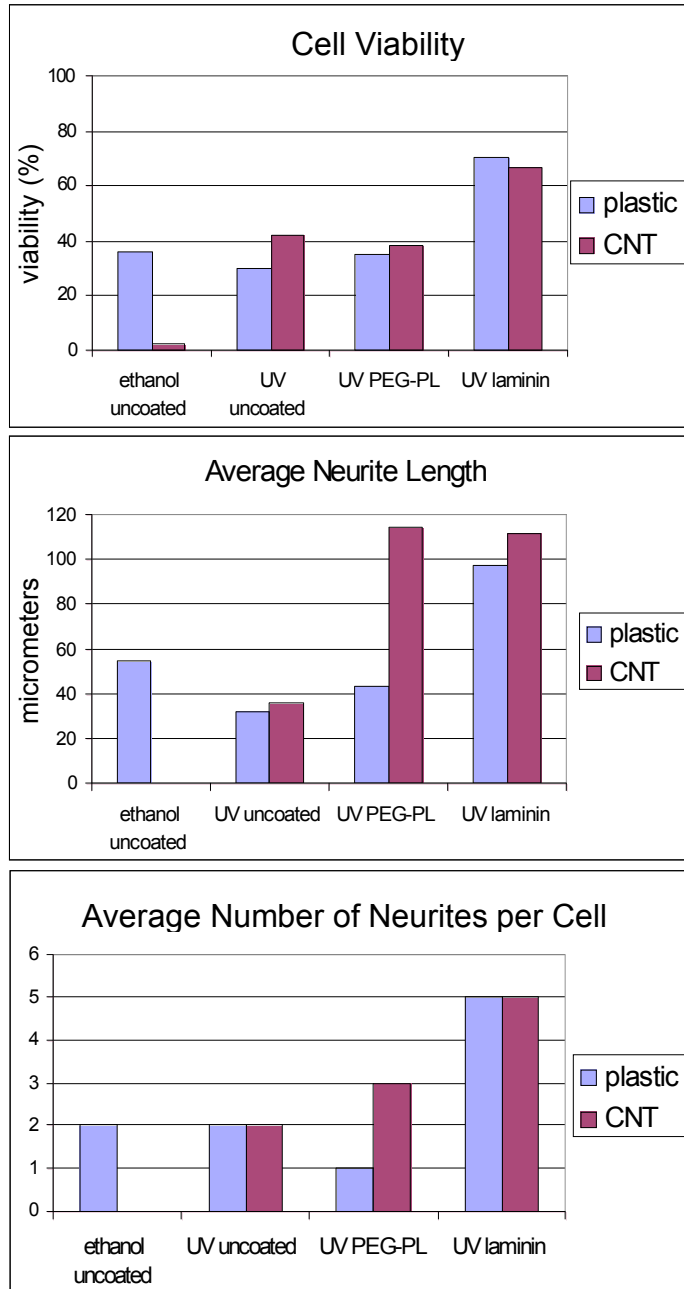


Figure 4.10 Statistics of hippocampal neuronal culture on unpatterned CNT mats with different treatments, compared to culture on Petri dish controls.

4.5 Summary

- In vitro neuronal culture on unpatterned CNT mat substrates is assessed as an investigation of the CNT biocompatibility.
- Retinal ganglion cells (RGCs) and hippocampal neurons are chosen as cell models for this work. NG108-15, a neuroblastoma × glioma hybrid cell line, is not suitable because of its relatively low electrical excitability.
- UV exposure is a more suitable sterilization method than ethanol soaking for the CNT substrates. Ethanol may be trapped in the porous nanotube structures and cause neuron death.
- Cell growth on uncoated or phospholipids-coated CNT substrates is comparable, if not superior, to cultures on Petri dishes under the same conditions.
- Traditional extracellular matrix proteins, including laminin and fibronectin, can adsorb onto the nanotubes. They can be used to improve cell adhesion and differentiation on the CNT substrates.

Chapter 5

Neural Stimulation

This chapter describes in vitro stimulation of nerve cells by the CNT microelectrode arrays. The stimulation experiments were performed as a proof of concept, with the objective to demonstrate that the CNT electrodes are able to stimulate the neurons, rather than to simulate the situation in real prosthetic applications. The chapter will start with the basic theory of action potential and extracellular stimulation, and then proceed to the details of the experiment.

5.1 Neural Stimulation Theory

The intracellular voltage of a neuron is more negative than the extracellular space when no stimulus is applied (“at rest”). When a neuron is properly stimulated (by either inputs from other neurons, or artificial stimuli placed upon by a researcher), the intracellular voltage will go through a rapid rise-and-fall cycle called action potential (or “spike”), and the neuron is said to be “excited”. The task of stimulating neural electrodes is to initiate action potentials in the target neurons in a controlled manner.

The resting potential and action potential of a neuron can be explained by the ion movement across its plasma membrane following basic physics laws. They are among the few biological subjects that can be precisely described and predicted in a quantitative way. Only the fundamentals of the ionic basis will be provided here. A more in-depth

explanation of membrane potentials can be found in most neuroscience textbooks [70, 71].

5.1.1 Ionic basis

The cell membrane is a fluidic mosaic of lipid and proteins. The lipid bilayer is about 6 nm thick. It is sparingly permeable to water, and impermeable to ions. The embedded cell membrane proteins are mainly ion channels for sodium, potassium, calcium and chloride. Some of the channels are very specific and only allow certain types of ions to pass. The ion channels can open and close in response to change in membrane potential (voltage-gated), mechanical pressure (stretch-gated), or ligand binding (ligand-gated). Voltage-gated ion channels open in an all-or-none fashion. An individual open channel allows a current of constant amplitude to flow through passively, driven by the concentration gradient and electrical force. Other membrane proteins include pumps and transporters, which move ions across the membrane against their electrochemical gradients.

Consider two ionic solutions of different concentrations separated by a semi-permeable membrane. At the beginning, the ion will start to diffuse across the membrane because of the concentration difference. Consequently, an electrical field will build up with this diffusion, and will oppose a driving force of the opposite direction upon the ions. When the electrical force is strong enough to balance the driving force of diffusion, the system reaches equilibrium, and the net ionic flow is zero. The equilibrium electrical potential across the membrane can be related to the solution concentration by the Nernst equation:

$$\Delta E = E_1 - E_2 = \frac{RT}{zF} \ln \frac{[A]_2}{[A]_1} \quad (5.1)$$

where $[A]_1$, $[A]_2$ are the concentrations of ion A in the two solutions, R is the thermodynamic gas constant ($8.315 \text{ J}\cdot\text{K}^{-1}\cdot\text{mol}^{-1}$), F is the Faraday's constant (9.648×10^4

C·mol⁻¹), T is the absolute temperature, and z is the valence of the ion. RT/zF has the dimension of volts, and equals to 25 mV at room temperature for ions with valence +1.

5.1.1.1 Resting Potential

Table 5-1 lists the physiological intracellular and extracellular concentrations of the major ion species in mammalian tissue, and the Nernst potential if the membrane is only permeable to that ion specie. At resting state, all excitable cells have far more open K⁺ and Cl⁻ channels than Na⁺ or Ca²⁺ channels on the membrane. So the membrane potential is largely determined by the Nernst potential of K⁺ and Cl⁻, with the intracellular potential more negative with respect to the extracellular space. However, there are also a small number of Na⁺ channels open, making the membrane potential less negative. The resulting membrane potential can be calculated by the modified Nernst equation:

$$E = \frac{RT}{F} \ln \frac{p_K [K]_o + p_{Na} [Na]_o + p_{Cl} [Cl]_o}{p_K [K]_i + p_{Na} [Na]_i + p_{Cl} [Cl]_i} \quad (5.2)$$

where $[K]_o$, $[Na]_o$, $[Cl]_o$ are ion concentrations outside of the cell, $[K]_i$, $[Na]_i$, $[Cl]_i$ are concentrations inside the cell, p_K , p_{Na} , p_{Cl} are membrane permeability to the ions.

Table 5-1 Ionic concentrations in mammalian skeletal muscle (after [71])

	Extracellular concentration (mM)	Intracellular concentration (mM)	Nernst potential (at 37°C) (mV)
Na ⁺	145	12	+67
K ⁺	4	155	-98
Cl ⁻	123	4.2	-90
Ca ²⁺	1.5	10 ⁻⁴	+120

In order to keep the intracellular sodium and potassium concentrations constant, there are sodium-potassium pumps on the cell membrane that constantly transport Na⁺ outwards and K⁺ inwards against their electrochemical gradients. To predict the resting membrane potential precisely, these pumps also need to be considered. The resting potentials of

different nerve cells vary slightly, but generally are about -70 mV. In some cells, it can be as large as -90 mV, and in others as small as -40 mV.

5.1.1.2 Action Potential

The nerves use electrical and chemical signals to interpret and transmit information. A most important electrical signal is the action potential. It is the universal digital code used in the brain, in the muscle, in the heart, and the sensory systems. As illustrated in Figure 5.1, the action potential is a momentary membrane potential impulse, which includes depolarization (the membrane potential E rises from negative to positive), repolarization (E falls back to negative), refractory period (E becomes even more negative than the resting potential, and then recovers to resting state). The action potential is ~ 100 mV in amplitude, and lasts a few milliseconds. The action potential is an “all-or-none” digital signal. If a stimulus exceeds the threshold, the cell fires an action potential; otherwise, the cell remains in resting state. The amplitude and duration of action potentials in a neuron are fixed, and do not change with the stimulus. It is essential for the nerves to use action potentials because they can propagate rapidly (sometimes as fast as 120 m/s!) over long distance without attenuation or distortion.

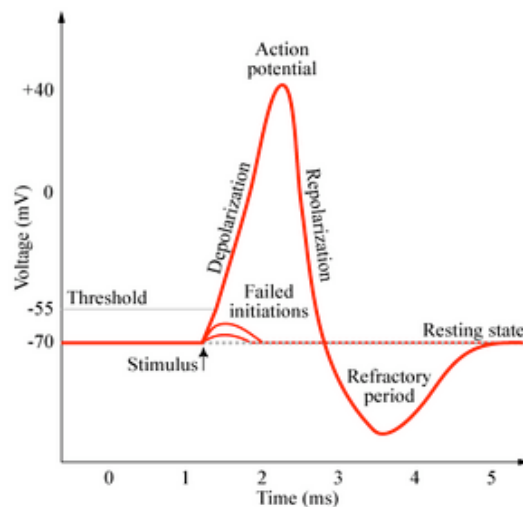


Figure 5.1 Schematic of an action potential showing different phases.

The ionic basis of action potentials was first quantitatively explained by Hodgkin and Huxley in 1952 [72-76]. Voltage-gated ion channels do not stay open. Instead, they constantly open and close in a random fashion. Both the voltage-gated sodium channels and potassium channels have a higher probability to be in the open state under depolarization. For sodium channels, an increased number of open channels will result in inward flow of Na^+ , further depolarizing the membrane, causing more channels to open. This is a process with positive feedback. On the other hand, the potassium channels work as a negative feedback system: if more potassium channels are open, then K^+ flows out, the membrane repolarizes, and K^+ conductance returns to its resting level.

The time courses of sodium and potassium conductance (g_{Na} and g_{K}) are very different:

$$\begin{aligned}
 g_{\text{Na}} &= g_{\text{Na}(\text{max})} m^3 h \\
 g_{\text{K}} &= g_{\text{K}(\text{max})} n^4 \\
 n &= 1 - e^{-t/\tau_n} \\
 m &= 1 - e^{-t/\tau_m} \\
 h &= 1 - e^{-t/\tau_h}
 \end{aligned} \tag{5.3}$$

where τ_m (0.2-0.6 ms) and τ_n (1-4 ms) are activation time constants for sodium and potassium respectively, and τ_h (a few milliseconds) is the sodium inactivation time constant. Therefore g_{Na} rises much faster than g_{K} , driving the membrane potential sharply towards the sodium equilibrium potential. Then the inactivation of sodium channels and activation of potassium channels together cause the repolarization of the membrane. Threshold is a depolarization potential at which the inward and outward currents reach an unstable balance. Any further depolarization will increase g_{Na} sufficiently for the generation of an action potential. Any subthreshold depolarization will fail to increase g_{Na} sufficiently, and the membrane will repolarize to its resting state.

It has been found that the mechanism of action potential generation is universal in all neurons. However, excitability properties do vary among neurons, as well as within

different regions of a neuron. This is mainly due to the large variance in the type and distribution of voltage-gated ion channels.

5.1.2 Extracellular stimulation

Action potentials are generally initiated by localized graded potentials, which are generated by extrinsic stimuli such as light, sound and touch. They then spread from cell to cell via either synaptic transmission (release of neurotransmitters) or electrical transmission (gap junctions formed by connexons). It has long been known that action potentials could be artificially induced by intracellular voltage clamp or current clamp techniques, in which a sharp glass physiological microelectrode connected to electronics is inserted into cells. It either resets the transmembrane potential or applies a known current to depolarize the cell. Intracellular stimulation offers precise control of the potential or current across the cell membrane, thus is widely used in basic neuroscience studies. However, intracellular stimulation is impractical for applications such as neural prostheses, where arrays of microelectrodes are needed to stimulate many cells *in-vivo* for an extended period. In these applications, extracellular stimulation is used instead, in which the electrodes are placed outside, but in the vicinity of the cells.

5.1.2.1 Cell Response in an Electrical Field

How cells respond to extracellular electrical stimulation is not a straightforward question. The response is a two-stage process that consists of a rapid initial polarization ($< 1 \mu\text{s}$), and the much slower change of the physiological state (several milliseconds) [77]. The polarization of cells in an electrical field has been studied extensively. A precise description will depend strongly on the cell geometry and electrical field, and in many cases, only a numerical solution can be obtained. However, many basic behaviors can be analytically explained with a simple model of a spherical cell in a uniform field [78].

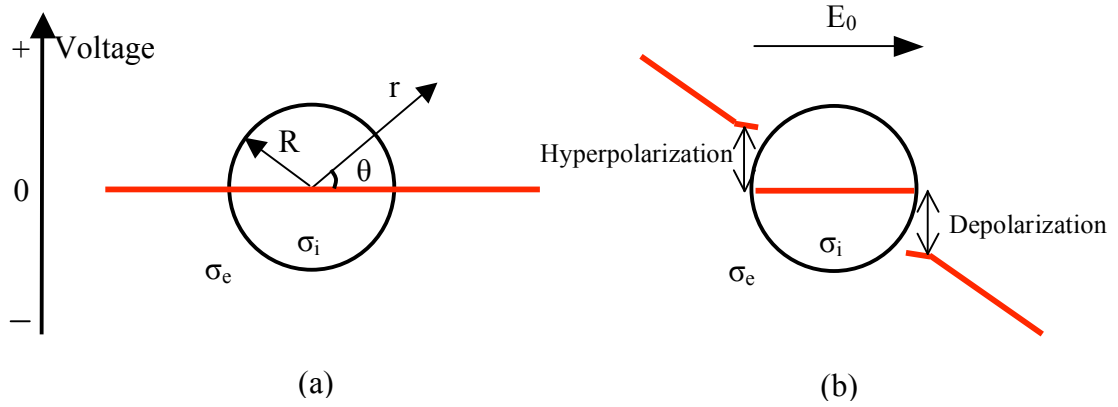


Figure 5.2 Extracellular and intracellular potential distribution. (a): cell at resting state, (b): cell polarization under a uniform electrical field.

Consider a cell of radius R in an ionic solution (Figure 5.2a). The cell cytoplasm conductivity is σ_i , and the conductivity of the extracellular solution is σ_e . For simplicity, we first neglect the resting membrane potential and define the initial potential to be zero everywhere. At time $t = 0$, a uniform extracellular electrical field \vec{E}_0 is applied. The intracellular potential Φ_i and extracellular potential Φ_e satisfy the Laplace's equation:

$$\begin{aligned}\nabla^2 \Phi_i &= 0 \\ \nabla^2 \Phi_e &= 0\end{aligned}\tag{5.4}$$

Φ_e is the sum of both applied field \vec{E}_0 and the induced field by the presence of the cell.

The solution of Laplace's equation in spherical coordinates is:

$$\Phi(r, \theta, t) = \sum_{m=0}^{\infty} (A_m(t)r^m + B_m(t)\frac{1}{r^{m+1}})P_m(\cos\theta)\tag{5.5}$$

where $P_m(x)$ is the Legendre function. Applying boundary conditions that $\Phi \neq \infty$ at $r = 0$, and $\Phi = -E_0 r \cos \theta$ at $r = \infty$, the solution can be written as:

$$\begin{aligned}\Phi_i &= A(t)r \cos \theta \\ \Phi_e &= (-E_0 r + \frac{B(t)}{r^2}) \cos \theta\end{aligned}\tag{5.6}$$

The other two boundary conditions at $r = R$ are:

$$\begin{aligned}\vec{j}_i &= \vec{j}_e \\ \vec{j} &= \vec{j}_R + \vec{j}_C = \frac{\Phi_m}{R_m} + C_m \frac{d\Phi_m}{dt}\end{aligned}\tag{5.7}$$

where $\vec{j} = \sigma \vec{E} = -\sigma \nabla \Phi$ is the current density, $\Phi_m = \Phi_i(R) - \Phi_e(R)$ is the transmembrane potential, R_m is the cell membrane resistance, and C_m the membrane capacitance. Solving the equations, we obtain the solution for the membrane potential:

$$\Phi_m = \frac{3\sigma_i \sigma_e R_m E_0 R \cos \theta}{\sigma_i R + 2\sigma_e R + 2\sigma_i \sigma_e R_m} (1 - e^{-t/\tau})\tag{5.8}$$

where τ is the time constant of cell response:

$$\frac{1}{\tau} = \frac{1}{R_m C_m} + \frac{2\sigma_e \sigma_i}{RC_m(\sigma_i + 2\sigma_e)}\tag{5.9}$$

Although this model is over-simplified, it provides some useful insight into how cells will respond to an electrical field (Figure 5.2b):

- *The potential of the intracellular space is approximately constant.* When the cell reaches a steady state ($t \gg \tau$), the intracellular potential is:

$$\Phi_i(t \gg \tau) = -E_0 r \cos\theta \frac{3R\sigma_e}{2R\sigma_e + R\sigma_i + 2R_m\sigma_e\sigma_i} \quad (5.10)$$

Applying the typical values from Table 5-2, $\Phi_i(t \gg \tau) = -10^{-5} E_0 r \cos\theta$. The variance of Φ_i is negligible, and can be treated as constant.

Table 5-2 Typical values of the physiological parameters of a neuron

Symbol	Definition	Unit	Typical value
R_m	Specific membrane resistance	$k\Omega \text{ cm}^2$	10
C_m	Specific membrane capacitance	$\mu\text{F cm}^{-2}$	1
σ_e	Extracellular conductivity	S cm^{-1}	0.02
σ_i	Cytoplasm conductivity	C cm^{-1}	0.005
R	Cell radius	μm	10

- *Half of the cell is depolarized, and the other is hyperpolarized.* There is a $\cos\theta$ term in equation (5.8). So at $z > 0$, $\Phi_m > 0$, the membrane is depolarized; at $z < 0$, $\Phi_m > 0$, the membrane is hyperpolarized. This is an important difference from intracellular stimulation, in which the entire cell is depolarized.
- *Cell polarizes much faster than the membrane time constant.* $1/\tau$ has two terms, and the first is the inverse of membrane constant. With the values in Table 5-2:

$$\begin{aligned} \frac{1}{\tau_m} &= \frac{1}{R_m C_m} = 10^2 \text{ sec}^{-1} \\ \frac{2\sigma_e\sigma_i}{RC_m(\sigma_i + 2\sigma_e)} &= 4.5 \times 10^6 \text{ sec}^{-1} \end{aligned} \quad (5.11)$$

Obviously, $1/\tau$ is dominated by the second term. So the polarization time constant τ ($< 1 \mu\text{s}$) is substantially shorter than the membrane constant ($\sim 10^1 \text{ ms}$). This fast response is critical for the nervous system.

- *The induced extracellular field is localized to the cell surface.*

$$\Phi_{induced} = \frac{B(t)\cos\theta}{r^2} \quad (5.12)$$

When $t \gg \tau$, using the values in Table 5-2:

$$\frac{\Phi_{induced}}{\Phi_{applied}} = \frac{B(t)}{E_0 r^3} = \frac{5 \times 10^{-10}}{r^3} \quad (5.13)$$

r is the distance in cm from the center of the cell. The induced field drops rapidly away from the cell surface.

- *Polarization strongly depends on the cell size and field strength.* Larger cells polarize more easily.

In real extracellular stimulation, the electrical field is usually non-uniform, and the cell deviates from a perfect sphere. Analytic and numerical calculations show that non-uniform field results in asymmetrical polarization of the cell, and larger depolarization. However, with increasing electrode-cell distance, depolarization in a non-uniform field quickly approaches the uniform field scenario [79].

The steady-state solutions of the polarization serve as the initial conditions for the second stage: change in physiological state as explained in Section 5.1.1.2. This process is much slower (milliseconds) due to the relatively slow kinetics of the voltage-gated ion channels.

5.1.2.2 Field Distribution of Cylindrical Electrodes

Now consider a cylindrical electrode of radius a and height h placed in a homogenous conductive medium of conductivity σ_e . In cell stimulation, typically a current i of known amplitude is injected from the electrode into the media. In the bulk media, the Ohm's law and steady-current condition give:

$$\begin{aligned}\vec{j} &= \sigma_e \vec{E} = -\sigma_e \nabla \Phi \\ \nabla \cdot \vec{j} &= 0\end{aligned}\tag{5.14}$$

So the electrical potential in bulk media satisfies the Laplace's equation:

$$\nabla^2 \Phi(r, z) = 0\tag{5.15}$$

When the returning electrode is placed at infinity, the boundary conditions are:

$$\begin{aligned}\frac{\partial \Phi}{\partial r} &= -\frac{j_s}{\sigma_e} \quad (\text{at } r = a) \\ \frac{\partial \Phi}{\partial z} &= -\frac{j_t}{\sigma_e} \quad (\text{at } z = h) \\ \Phi &= 0 \quad (\text{at } r = \infty \text{ or } z = \infty)\end{aligned}\tag{5.16}$$

where j_s and j_t is the current density at the sidewall and the top of the electrode, respectively.

Under steady current, neither the electrical field nor the potential in the bulk media changes with time. Based on equations (5.15) and (5.16), the electrical field of a cylindrical electrode in a homogeneous conductive medium can be simulated (FEMLAB, COSMOL Inc.). In the *in vitro* stimulation experiments performed in this work, the nerve cells are cultured on the CNT microelectrode array (as will be described in Section 5.3). The simulated electrical field on the substrate surface is shown in Figure 5.3. Regardless of its size, each electrode injects a total of 10 μA current. In Figure 5.3B, the fields of electrodes with 40 μm in height, and different diameters (20, 50, 100 μm) are plotted versus distance from the edge of the electrode. The field increases considerably when the electrode scales down, because of the higher local current density. In other words, for smaller electrodes, less current will be needed for excitation. Nonetheless, the field falls rapidly with increasing distance from the electrode. More than 100 μm from

the electrode, the fields of different-sized electrodes are almost the same. In Figure 5.3C, different contributions from the pillar top and sidewall are considered. As described in Chapter 3, the top of the CNT pillar has a higher roughness factor than the sidewall, hence so does the current density. But again, it becomes an insignificant factor at a distance away from the electrode.

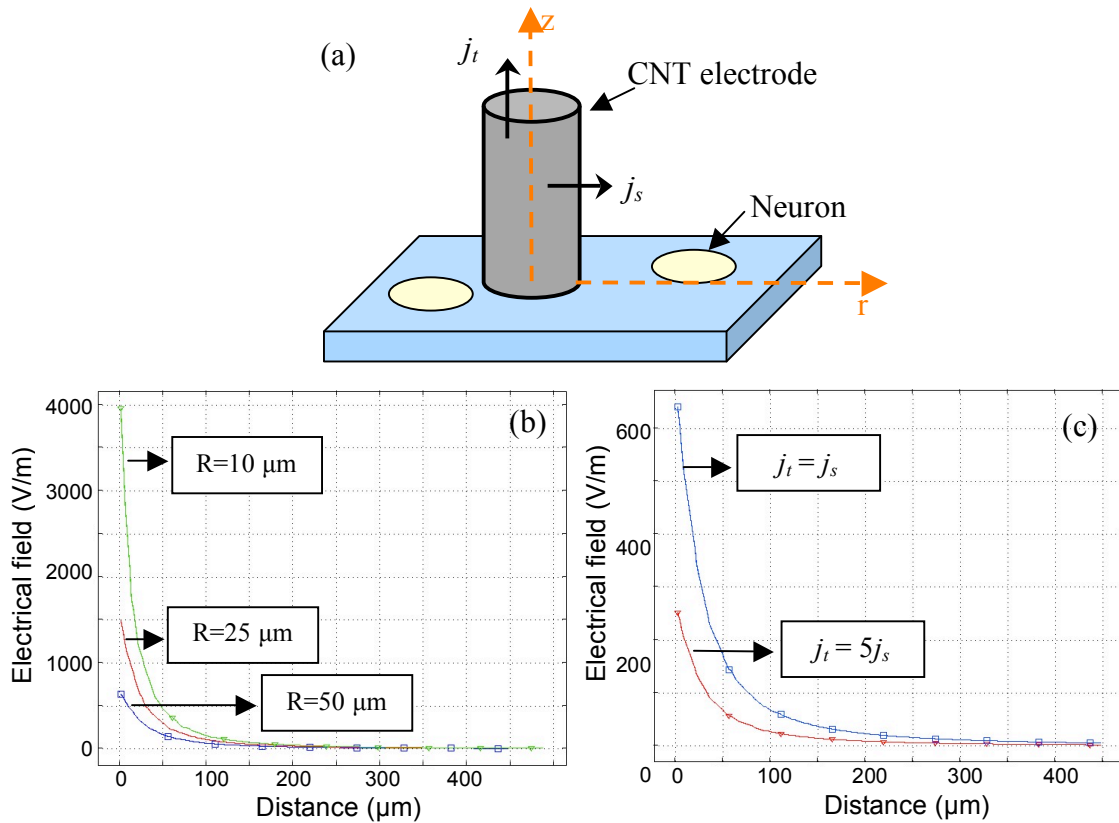


Figure 5.3 Electrical field of a cylindrical electrode. (b) and (c) are FEMLAB simulation, in which the field strength is plotted over distance r (at $z = 5 \mu\text{m}$). r starts from the edge of the electrode. (b) plots the result for electrodes of different diameter, assuming $j_t = j_s$. (c) is a 100 μm -diameter electrode with different current density distribution.

5.2 Detection of the Action Potential

The action potential can be recorded electrically, with either intracellular or extracellular electrodes. Intracellular recording allows study of the details in membrane potential change, including both the amplitude and the time course. However, it requires selection and impalement of a specific cell that is expected to fire. It is difficult to perform, and unnecessary for the proof-of-concept purpose. Extracellular recording has a low signal-to-noise ratio, and signals from multiples neurons, as well as the electrical stimuli, are often coupled.

An alternative solution is optical recording. The cells can be loaded with either voltage-sensitive or ion-sensitive fluorescent molecules. Upon an action potential, the fluorescence intensity changes with the intracellular potential or ion concentration, thus gives a visual “map” of excited cells. Since electrical stimulation is used, there is no coupling between the stimulus and the signal.

Voltage sensor probes are based on Fluorescence Resonance Energy Transfer (FRET) [80]. They usually consist of two fluorescent parts: a donor that is bound to the exterior of the cell membrane, and an acceptor that is mobile within the bilipid membrane in response to the membrane potential. In the resting state, both the donor and the acceptor are associated with the exterior side of the membrane, generating a strong FRET signal from the acceptor probe. When the cell is depolarized, the acceptor translocates to the interior side of the membrane and the FRET pair is separated. The fluorescent signal now is solely from the donor, which is at a different wavelength. Therefore the membrane potential change can be detected by measuring the emission ratio (donor: acceptor). Voltage sensor probes measure directly the membrane potential and do not depend on any ion channel activity. The emission ratio is quantitatively related to the potential (1% change in emission ration per mV). But unfortunately, change in the emission ratio needs to be decided from data analysis, instead of visual judgment of the fluorescent images. In stimulation experiments, the conclusion of whether an action

potential has been induced needs to be made instantaneously. In addition, the time response for the fastest available acceptor is still ~ 20 ms, much longer than the time course of an action potential. Because of these reasons, voltage sensor probes were not chosen for this experiment.

Instead, calcium imaging was used for the optical detection of action potentials. Almost all excitable cells have voltage-gated Ca^{2+} channels, which open with depolarization and shut with repolarization in a steeply voltage-dependent manner. Similar to sodium ions, Ca^{2+} influx contributes to the rising phase of an action potential. Calcium is also released from intracellular stores regulated by G-proteins. Since the intracellular free calcium level is kept extremely low (10-100 nM) at the resting level, the Ca^{2+} influx/release during the action potential results in an appreciable increase the local calcium concentration (in comparison, $[\text{Na}^+]_i$ is barely altered by an individual action potential). After the action potential, calcium ions are removed from the cytoplasm to the extracellular space and the intracellular compartments by Ca^{2+} pumps and $\text{Na}^+\text{-Ca}^{2+}$ exchange systems. Therefore, the intracellular free calcium concentration follows the rise and fall of membrane potential, and can serve as an indirect indicator of the action potential.

Change in the intracellular calcium level can be detected by Fluo-4 (Invitrogen, Molecular Probes, CA), a calcium indicator which exhibits a large fluorescence intensity increase on binding of free Ca^{2+} [81]. The concentration of free calcium ions is related to the fluorescence intensity through the following relation:

$$[\text{Ca}^{2+}]_{free} = K_d \frac{F - F_{min}}{F_{max} - F} \quad (5.17)$$

where K_d is the dissociation constant, F is the signal fluorescence intensity, F_{min} is the fluorescence intensity of Fluo-4 in absence of calcium, and F_{max} is its intensity in calcium-saturated solutions. The dissociation constant of Fluo-4 is 345 nM, setting the

detection range to be from 35 nM to 3.5 μ M. This is optimal for measuring intracellular $[Ca^{2+}]$ level before and during an action potential.

In order to load the Fluo-4 probes into cells, an AM (acetoxymethyl) ester form of Fluo-4 was used. The hydrophobic AM ester group can diffuse into the plasma membrane, bringing the indicator molecules inside the cell. Once inside, acetyl esterases hydrolyzes the acetyl ester linkage, releasing the free indicator, which leaks out of cells far more slowly than its AM ester form. This loading method is non-disruptive, and allows large populations of cells to be loaded simultaneously. The AM ester form is insensitive to Ca^{2+} , therefore the background fluorescence level of the loading solution is very low.

After the action potential, unbound Ca^{2+} ions are pumped out of the cell, breaking the $[Fluo-4][Ca^{2+}] \rightleftharpoons [Fluo-4-Ca^{2+}]$ equilibrium, forcing the reaction to go towards the left until most of the free Ca^{2+} are removed from cytoplasm, and the cell returns to resting state. This process is limited by the dissociation rate, hence limiting the temporal resolution of calcium imaging. However, the detection speed is still fast enough for most applications. Resolution of action potentials at high frequency (up to 50Hz) has been reported [82].

5.3 Experimental Methods

For the stimulation experiments, hippocampal neurons were cultured on the CNT microelectrode arrays, and then loaded with Fluo-4 calcium indicators shortly before imaging. Action potentials were detected with inverted fluorescence microscopy.

5.3.1 Device treatment

The CNT microelectrode arrays were sterilized by UV exposure (see Section 4.3.1.1). To promote cell adhesion on the silicon dioxide surface, the devices were first coated with poly-D-lysine, as recommended by the standard hippocampal neuron culture protocols [67, 68]. New devices were then soaked in complete cell culture medium for 1-2 days to condition the surface. This incubation allowed proteins in the medium to adsorb onto the

CNT surface and improve its hydrophilicity (Section 3.4.2), as well as allowing any substance entrapped during the fabrication process to degas. The devices were rinsed once with fresh Neurobasal before the cells were plated. Care was taken that once wetted, the CNT device should never be left dry in air. Otherwise the CNT pillars might collapse, due to the lateral cohesive capillary force during the drying process. When not in use, the chamber of the CNT device was filled with (sterile) water, and sealed tightly to avoid evaporation for long-term storage.

The steps of device treatment are listed as following:

1. Sterilize by overnight UV exposure
2. Rinse two to three times with sterile DI water.
3. Incubate the device with poly-D-lysine (50 μ g/ml in water) for 2-10 hours at room temperature.
4. Rinse once with sterile DI water.
5. Soak new devices in complete cell culture medium (Neurobasal supplemented with B27/glutamine/glutamate) for 1-2 days at 37°C.
6. Rinse once with fresh Neurobasal before plating the cells.

5.3.2 Cell Culture on the Device

Hippocampal neurons were used for stimulation experiments because of their availability (Brainbits, Springfield, IL), ease of culture, and high electrical excitability. Cells were harvested from embryonic rat hippocampus tissue with standard protocols (Appendix C). Cells were diluted in the culture medium and then plated onto the devices, typically at a density of about 100 cells per mm². This cell plating density was high enough to obtain reasonably good viability, while low enough to have isolated individual cells. Highest viability was achieved when the plating density was between 160 and 400 cells per mm².

However, cells cultured at these densities formed extensive neural networks, which caused difficulty in identifying direct excitation by the electrode from indirect excitation through synaptic connection with other neurons.

Cells showed good adhesion and growth on the CNT microelectrode arrays. Cells were usually well differentiated after four days of culture (Figure 5.4). Stimulation experiments were usually carried out between day 4 and day 8.

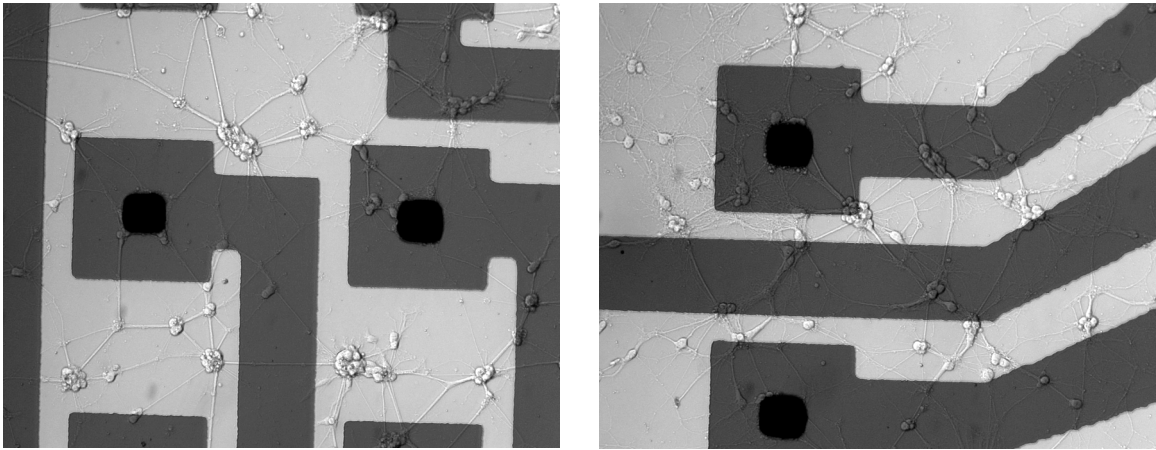


Figure 5.4 Hippocampal neurons cultured on a CNT microelectrode array. Day 4.

5.3.3 Fluorescent Dye Loading

Prior to stimulation, cells were incubated with 2 μ M Fluo-4 AM ester (reconstituted in DMSO at 1mM) in pre-warmed Ringer's solution (2.5 mM CaCl₂/1.3 mM MgCl₂/10 mM HEPES in Hank's Balanced Salt Solution, pH adjusted to 7.4) in the dark at room temperature for 30 minutes. Cells were then rinsed thoroughly with indicator-free Ringer's solution, and further incubated for another 30 minutes at 37°C. The devices were then mounted onto the connector (see Section 2.3.2) and stimulation was usually carried out within an hour after loading.

5.3.4 Microscopy and imaging

Optical recording was done using an inverted microscope (Nikon Eclipse TE300) with a xenon source (75W), connected to a digital camera (Hamamatsu ORCA-ER) (see Figure 5.5). The absorbance spectrum of Fluo-4 peaks at 494nm, and emission peaks at 516nm. A FITC filter set (Chroma Technology Corp, Brattleboro, VT) was used. The dichroic mirror is highly reflective at the excitation wavelength, and highly transmissive at the emission wavelength (Figure 5.6). Data acquisition was automated by a computer and MetaMorph software (Molecular Devices, Sunnyvale, CA). Data were processed and analyzed with the same software. The ambient temperature was controlled at 35°C with a home-built thermostat.

After locating the electrode and the cells, the dynamic range was adjusted by reducing the digital contrast and brightness until the cells were barely visible, insuring that any increase in the fluorescence level could be detected. To record stimulation, images were captured at 3 frames per second. To avoid photobleaching of the dyes, the excitation light was switched on and off at the same rate by a computer controlled Uniblitz[®] shutter driver (Vicent Associates, VMM-D1, NY).

The fluorescence intensity of the cells was measured utilizing MetaMorph software.

Fluorescence intensity change was calculated as $\frac{(F'-B')-(F_0-B_0)}{(F_0-B_0)} \times 100\%$, where F_0

and F' represented the cell fluorescence intensity in the resting state and upon stimulation, respectively. B_0 and B' stood for the background fluorescence level before and after stimulation.

After recording, the cells were removed from the device by overnight incubation in trypsin-EDTA at 37°C. The devices were then well rinsed and refilled with sterile DI water, sealed tightly for future use. The devices can be stored in this way for at least a few months.

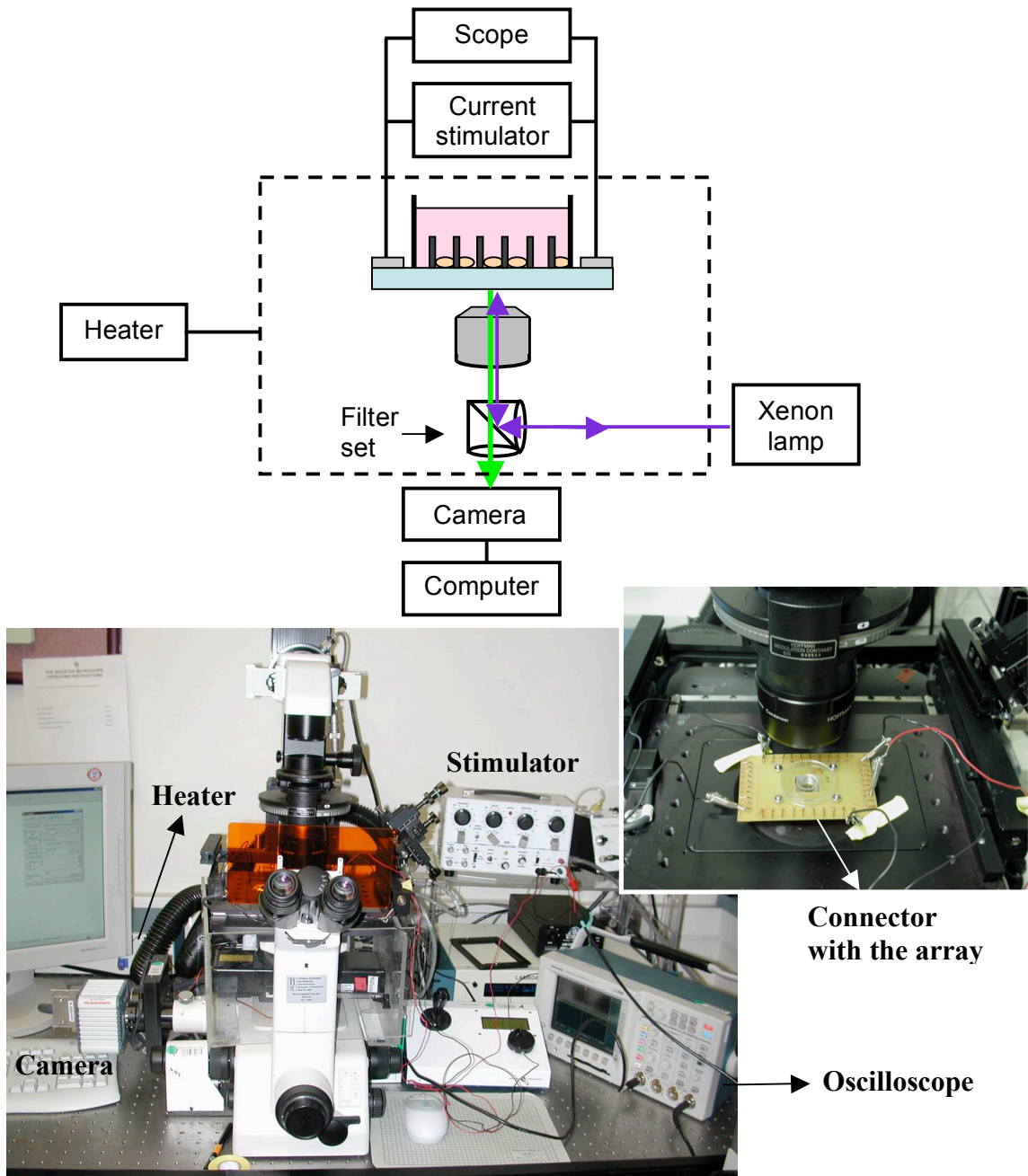


Figure 5.5 Experimental setup for cell stimulation and detection.

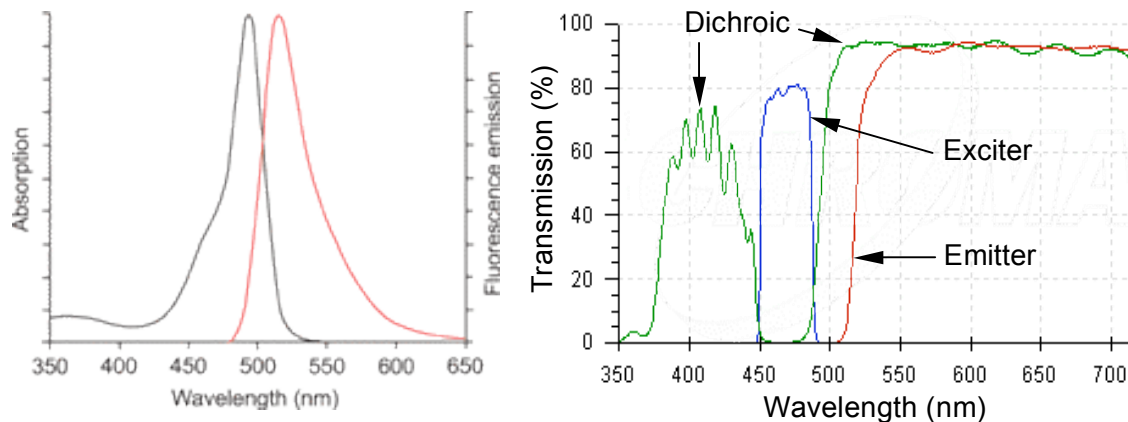


Figure 5.6 The spectra of Fluo-4 and the filter set. *Image source: Molecular Probes, and Chroma Technology.*

5.4 Stimulation Results

Action potentials in the hippocampal neurons can be induced either electrically or chemically. In this work, chemical stimulation was used as a control test to ensure that cell preparation, dye loading and optical recording were properly done. The cultured cells on the CNT devices were then stimulated electrically.

5.4.1 Chemical Stimulation

Besides morphology and intracellular enzymatic reactions (LIVE/DEAD stain), the health of the cultured cells was also evaluated by their electrophysiological activities, i.e., whether the cells can fire action potentials in response to chemical stimulants called neurotransmitters. There are over 60 identified neurotransmitters and for the hippocampal neurons in our experiment, glutamate was used as the stimulant. Glutamate is the most important and abundant excitatory neurotransmitter in the central nervous system, and is believed to be involved in cognitive functions, such as learning and memory [70]. Hippocampal neurons express a variety of glutamate receptors. For excitation, 10 μ l of prewarmed 10 mM glutamate (in the Ringer's solution) was added

into the bath solution near the target cells. The Fluo-4 fluorescence intensity change in the cells before and after stimulation are shown in Figure 5.7.

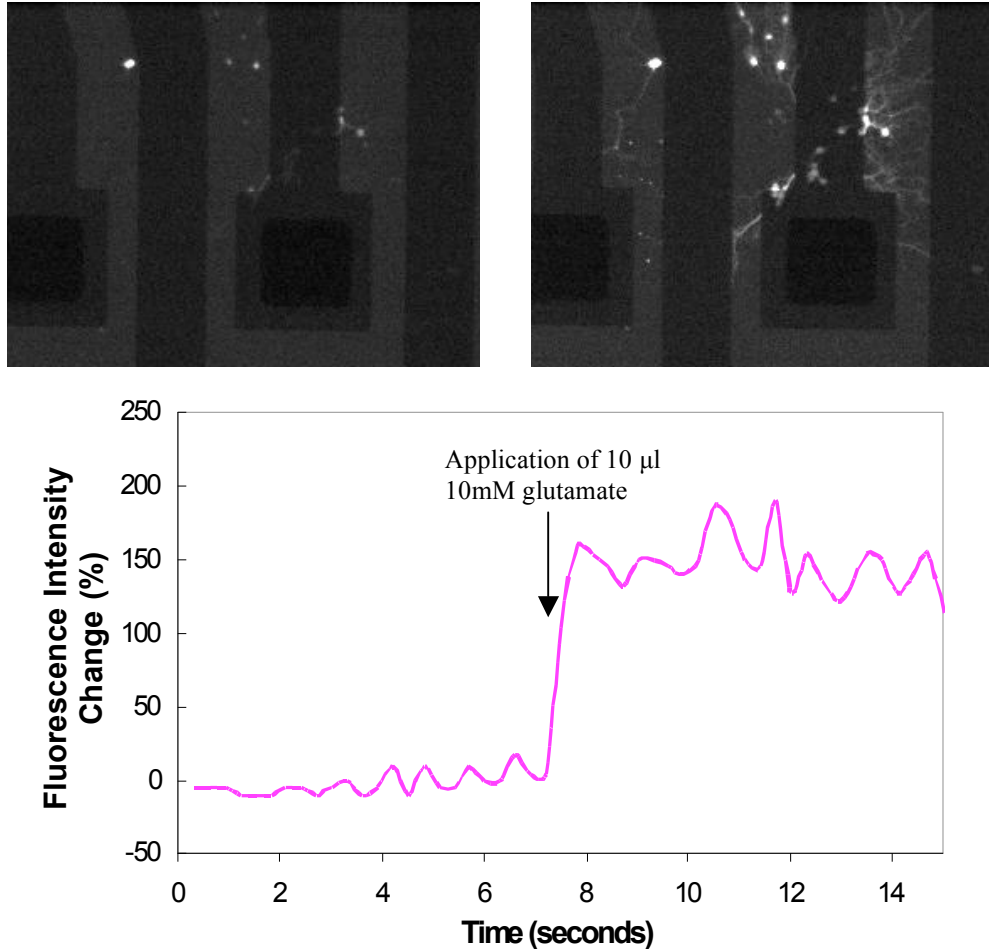


Figure 5.7 Fluoro-4 fluorescence intensity change in hippocampal cells stimulated with glutamate. Fluorescence intensity change was calculated as $((F'-B')-(F_0-B_0))/(F_0-B_0)$, where F stands for fluorescence intensity of the cell, and B for background noise.

Glutamate is removed from the extracellular space by glutamate transporters existent in neuronal and glial membranes. Excess glutamic acid triggers a process called excitotoxicity, causing neuronal damage and eventual cell death [83]. The dose used in our experiment far exceeded the removal ability of the transporters. The cells were

intoxicated by excessive activation and could not be used for stimulation again. (As shown in Figure 5.7, the fluorescence level did not return to its resting level after excitation.) Therefore, chemical stimulation was only used on three occasions in our experiments. Prior to electrical stimulation, some cells cultured on Petri dishes were first chemically stimulated as an initial control test. It was also used for trouble-shooting if no electrical excitation was obtained, or to examine the condition of the cells after electrical stimulation.

5.4.2 Electrical Stimulation

The complete setup for the optical recording of electrical stimulation was illustrated in Figure 5.5. Current pulses were applied between a CNT electrode and four returning electrodes placed at the corners of the chip. The resulting voltage excursion was monitored by a digital oscilloscope to ensure that the electrode potential did not exceed the electrochemical safety limits (see Section 3.6). Either a single current pulse, or a short train of pulses was used as the stimulus. Since the CNT electrodes operated primarily through capacitive current, theoretically charge-unbalanced stimulation protocols could also be used, if enough time was given for the capacitor electrode to discharge.

CNT microelectrodes of $50\ \mu\text{m} \times 50\ \mu\text{m}$ and $100\ \mu\text{m} \times 100\ \mu\text{m}$ were used for stimulation tests. Among 9 different devices tested, 7 successfully excited the neurons in a reliable way. Figure 5.8 shows the fluorescence level increase in the hippocampal cells after a stimulus was applied. More importantly, the neurons could be stimulated repeatedly with the CNT electrodes. An example is shown in Figure 5.9. A series of one-millisecond monophasic cathodic pulses were applied with intervals of 4-5 seconds, to ensure that the cells returned to their resting state and the electrode discharged completely after each pulse. Each fluorescence intensity peak represented one or a few action potentials. The multiple peaks showed that the cell responded consistently to the stimulating pulses. The stimulation was repeated over 100 times. This repeated excitability indicated good cell

physiological condition and normal CNT electrode functioning, even under prolonged, charge-unbalanced stimulation. A dose of glutamate was applied after the electrical stimulation and the cells were still able to be excited chemically.

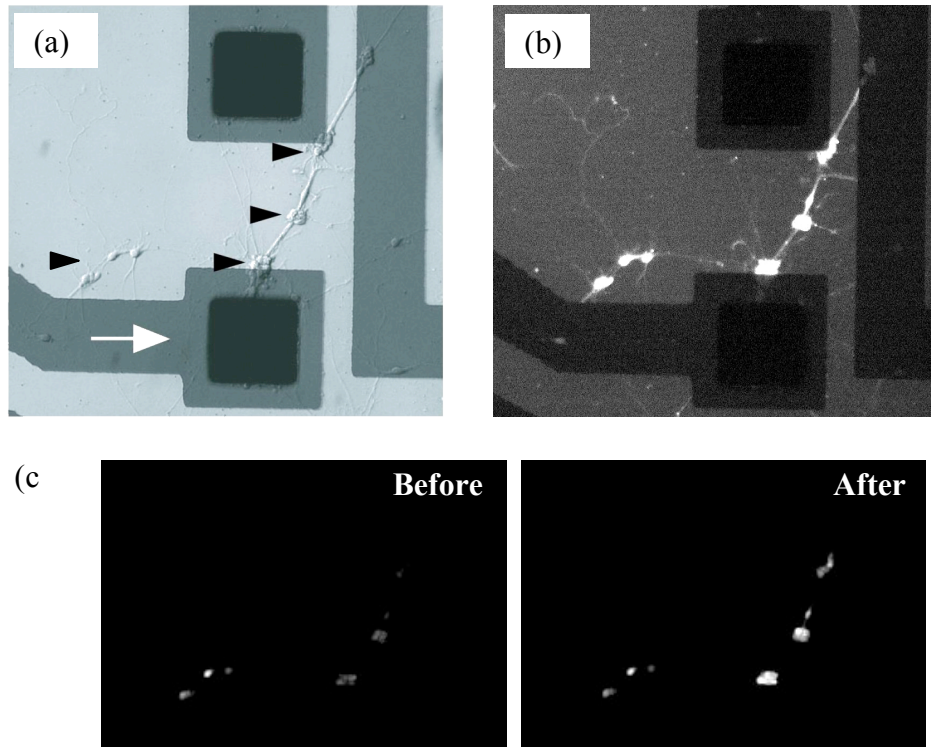


Figure 5.8 Representative plot of hippocampal cell stimulation with CNT microelectrode arrays. (a) Light microscopy image. The arrow points to the CNT electrode to which current pulses were applied. The arrowheads point to cells that are shown in (c). (b): Fluorescent image of the cells loaded with Fluo-4 (resting state). (c): Fluo-4 images before and after a stimulus. The brightness and contrast in (c) was reduced until the cells were barely visible before the stimulus.

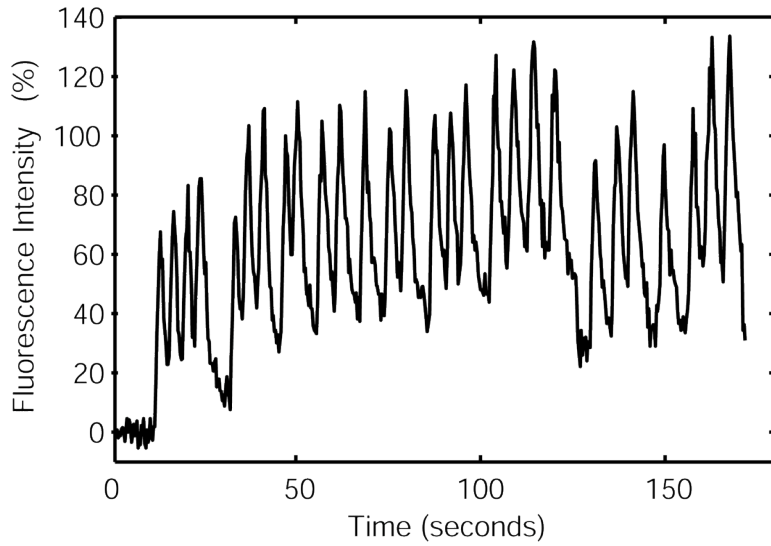


Figure 5.9 Repeated cell stimulation with a CNT electrode. The cell generated over 100 spikes during a continuous, charge-unbalanced stimulation.

Incomplete discharging of the capacitive CNT electrodes can build up the potential and lead to electrochemical hazards, such as hydrolysis, in successive stimulations. The time constant of the CNT electrodes can be estimated from the equivalent RC circuit:

$$\tau = R_s C_d \quad (5.18)$$

From the calculations in Chapter 3, R_s is about 1-10 k Ω , C_d is 0.05-0.5 μ F for the size of electrodes used in the experiment. So the time constant τ for a charged CNT electrode is estimated to be 0.05-5 ms, on the same order of an action potential. When an oscilloscope is connected, the resistance of the scope R_o must be included to the time constant:

$$\tau' = (R_s + R_o)C_d \quad (5.19)$$

R_o is 1 M Ω , so the time constant is now 50-500 ms. Figure 5.10 shows the measured voltage decay trace after a monophasic cathodic current pulse of 1 ms is applied at $t = 0$.

The curve fitting gives a time constant of about 100 ms. Therefore, an interval of a few seconds between the monophasic stimuli should have allowed sufficient time for the CNT electrode to discharge completely. In applications where high-frequency stimulation is needed, the capacitive electrode time constant (~ 1 ms, if the oscilloscope is not used) should still not be a limiting factor.

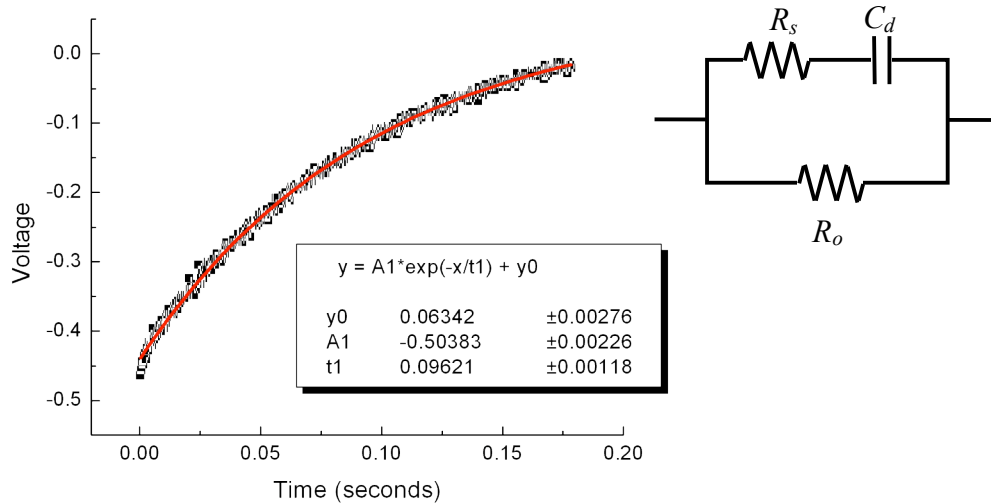


Figure 5.10 Discharge of a CNT electrode, traced by an oscilloscope. The equivalent RC circuit includes the spreading resistance R_s , the interfacial capacitance C_d , and the oscilloscope resistance R_o .

To determine the stimulation threshold, one-minute intervals were given between the stimuli. Fluorescent imaging was also paused during the interval to avoid photobleaching the Fluo-4 molecules. Imaging then resumed and a current pulse of slightly higher amplitude (or duration) was applied. These procedures were repeated until a transient increase in cell fluorescence level was identified by the observer, and confirmed with quantitative analysis of the fluorescence intensity. The stimulation threshold was 10-20 μA for 1 ms single cathodic pulses. Similar thresholds were obtained from control tests with commercial platinum-black microelectrode arrays (50 μm \times 50 μm , MED64 Systems). The range of the threshold agreed well with theoretical modeling results for

extracellular stimulation of hippocampal neurons [84]. The cell-electrode distance was relatively large in this experimental setup using inverted fluorescence microscopy. The poly-silicon pad underlying each CNT pillar was less transmissive at the working wavelength of Fluo-4, so virtually no fluorescent signal could be detected within that region. CNTs were also non-transparent, hence only cells 50 μm or further from the electrode edge could be studied. As depicted in Figure 5.3, we could expect that the stimulation threshold would drop significantly for cells closer to the electrodes.

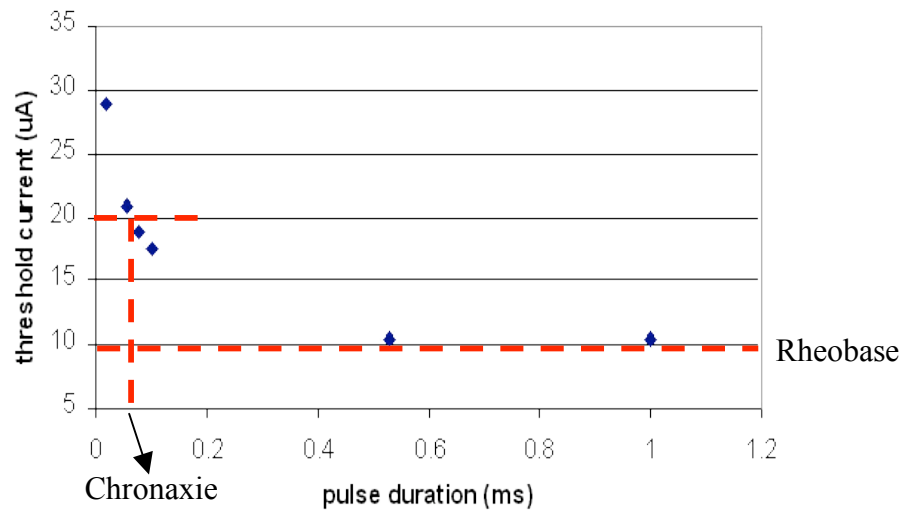


Figure 5.11 Strength-duration curve of the stimulation threshold of a hippocampal neuron with single monophasic cathodic pulses.

The stimulation threshold was measured for pulses ranging from 20 μs to 1 ms. The threshold current increased with decreasing pulse duration (Figure 5.11), known as the strength-duration relation. The relation is usually described by two parameters: *rheobase*, which is the minimum stimulus strength that will produce an action potential, and *chronaxie*, which is the stimulus duration that yields a response when the stimulus strength is set to twice of the rheobase. The strength-duration curve is well-known though often misunderstood. The duration dependence is commonly attributed to the charging of the cell membrane capacitor [85], whose time constant is on the order of 10

ms (Section 5.1.2.1). Although maybe valid for intracellular stimulation, the capacitor theory cannot explain the much shorter chronaxie (typically less than 1 ms) measured in most extracellular neural stimulation experiments (Figure 5.11, and [86]).

The strength-duration relation of extracellular stimulation can be better explained by the properties of the ion channel conductivity [84]. The probability of a voltage-sensitive sodium ion channel to be in an open state increases with membrane depolarization. When a stimulating current pulse is applied, part of the cell membrane is depolarized instantaneously (within microseconds, see Section 5.1.2.1). This initial depolarization results in more open sodium channels and this positive feed-back system further depolarizes the cell membrane. If the stimulus lasts long enough so that this dynamic process can continue on by itself even after the stimulus is turned off, then the cell will fire an action potential. On the other hand, if the stimulus is too short, the sodium conductance is still not sufficient to override the resting potassium conductance and the cell will not spike. In this case, higher initial depolarization (current pulses of larger amplitude) must be used for stimulation. If the stimulation current is too low (below the rheobase), then it will not generate action potential no matter how long the pulse duration is. This is caused by the eventual dominance of slower processes including the inactivation of the sodium channels and the activation of the potassium channels. The time constants of these processes are about 1-4 ms, in good agreement with the measured stimulus duration when the rheobase is reached. In other words, extracellular stimuli with durations longer than these time constants will not contribute to the depolarization.

5.5 Summary

- The ionic basis of the action potential was described. The mechanism of extracellular electrical stimulation was explained analytically.
- In vitro stimulation of hippocampal neurons by the CNT microelectrode array was demonstrated. The action potentials were optically detected by a calcium indicator Fluo-4.
- The cells cultured on the CNT devices showed good viability, neurite outgrowth and physiological activity. Repeated excitation was obtained, even under charge-unbalanced stimulation protocols.
- The stimulation threshold for 1 ms single cathodic pulses was about 10-20 μA .
- The strength-duration curve of the threshold current was also measured. The origin of the strength-duration relation was discussed.

Chapter 6

Conclusions and Future Perspectives

Microelectrode arrays can induce action potentials in nerve cells and modulate their behavior. They are essential for prosthetic and therapeutic applications, to either restore a lost neural function (for example, vision or hearing), or treat neurological disorders such as the Parkinson's disease. There is also an increasing need for stimulating and recording microelectrode arrays in basic neuroscience research.

An ideal stimulating neural microelectrode array needs to be both efficacious and safe. While the electrode size continues to scale down, conflicts have arisen between these two requirements, and efficacy often has to be compromised. Such problems can be solved, or at least alleviated through proper design of the electrodes. This work focused on the development of a protruding microelectrode array using carbon nanotubes as the electrode material, with the objective to enhance the efficacy while satisfying the safety requirements. Fundamental properties of the device, including its electrochemical performance and biocompatibility, were investigated, followed by a demonstration of neural stimulation.

Prototype CNT microelectrode arrays were fabricated on quartz substrates, using conventional silicon-based micro-fabrication processes. Multi-walled CNT pillars were synthesized using a catalytic thermal chemical vapor deposition system and integrated onto pre-patterned circuits as electrodes. Both the synthesis and fabrication processes had very high yield and repeatability.

As-grown CNTs are highly hydrophobic. However, hydrophilicity of the CNT microelectrodes can be improved by surface modification, such as non-covalent binding of phospholipids and proteins. As a consequence, both the electrochemical performance and the biocompatibility have been significantly enhanced. The CNT microelectrodes have superior electrochemical properties compared to traditional metal and metal alloy neural electrodes. They operate predominantly with capacitive current, which is an ideal charge injection mechanism for neural stimulation, while offering a competitive charge injection ability of 1-1.6 mC/cm². Primary nerve cells cultured on CNT substrates and microelectrode arrays show comparable (or in some cases, even better) viability and neurite outgrowth to cultures on the Petri dish controls. An interesting 3D growth pattern has been observed in neurons cultured with CNT pillar arrays, suggesting their potential application as scaffolds in tissue engineering.

In vitro neural stimulation with the CNT microelectrode array has been demonstrated as a proof of concept. Hippocampal neurons cultured on the device can be repeatedly excited over 100 times, even with charge-unbalanced stimulation protocols, indicating good cell physiological condition and normal CNT electrode functioning under prolonged stimulation.

The advantageous electrochemical, mechanical, and chemical properties of CNTs suggest that they are capable of providing a safer and more efficacious solution for neural stimulation than previous metal electrode approaches. The protruding geometry is designed to bring the electrode into proximity with the target neurons in layered tissues and further reduce the required stimulation current, thus allowing the use of smaller electrodes at higher density, reducing tissue damage, as well as lowering power consumption and heat dissipation. Besides stimulation, the CNT electrodes may also act as recording electrodes to sense electrical activities in the nervous system.

The CNT microelectrode arrays used in this work were designed and fabricated for in vitro experiments. For in vivo tests in the future, especially long-term implants,

significant reduction in the chip size will be required. For example, a retinal implant normally should not exceed 3 mm in diameter. Fortunately, this dimension is still well within the limits of standard UV-lithography based fabrication capability, therefore, except for mask design, most of the other processing steps should still be applicable. In addition to size reduction, some other future work include the insulation of the CNT pillar sidewalls, integration with soft substrates, design of optimal surface modification, and in vivo biocompatibility tests.

Sidewall Insulation

As described in Chapter 3, current is injected from both the top and the sidewall of the CNT pillar electrodes. For in vivo applications, it will be necessary to insulate the sidewall of the pillar, leaving only the tip exposed (Figure 6.1).

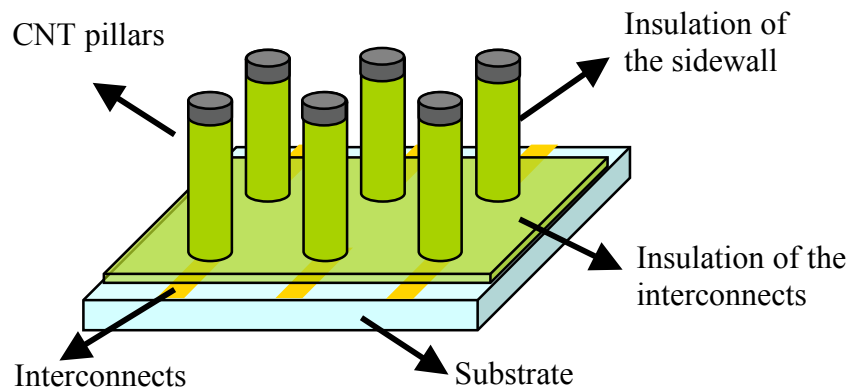


Figure 6.1 Schematic drawing of a CNT microelectrode array with sidewall insulation.

Realization of such a structure may not be a trivial task. In one of the initial tests, a silicon nitride layer was deposited onto the CNT pillars. In another, the pillars were spin-coated with polymers (photoresist and polyimide). Both silicon nitride and polymer seemed to adhere onto the nanotubes in SEM images and did reduce the current flow.

However, the interaction between these layers and the CNT surface needs to be better understood, including the strength of adhesion and the conformality of the coating. A noteworthy technique is hot-filament CVD (HFCVD), which can create a thin, conformal coating on the nanotubes [87].

Integration with Soft Materials

Although silicon substrates are widely used in current implants, it is highly desirable to substitute them with soft and flexible polymer substrates. For instance, a flexible retinal implant will be advantageous because of the curvature of the eyeball. The implants also often need to be very thin (10-30 μm for the retina), which is difficult to accomplish with silicon substrates. Another advantage of polymer substrates is that they can be permeable to water and nutrient flow, hence will better preserve the tissue around the implant. With an increasing interest in polymer-based electronics and microfluidic devices, significant progress has been made in fabricating microstructures with soft materials, such as PDMS and polyimide [88-90].

Nonetheless, integration of CNTs with soft substrates is still challenging, since virtually all polymers fail at the CNT growth temperature (700°C). Here we propose two possible approaches towards the integration. One is direct growth of CNTs on polymer substrates at low temperature, using plasma-enhanced CVD (PECVD) techniques. CNT synthesis at as low as 120°C has been reported [91], although both the growth rate and the tube quality fall considerably with decreasing growth temperature. Another possibility is to transfer CNTs from silicon to polymer substrates after the growth. Some preliminary trials have been made to transfer CNT mats (aligned and entangled), lines and pillars onto thin PDMS membranes. Two methods were used: one uses HF to lift CNTs off from a silicon dioxide substrate, and then transfer the free-standing CNTs onto a PDMS film; the other is “stamps” CNTs onto semi-cured PDMS, and then fully cure the film. The first method can be used to transfer CNT mats (Figure 6.2a and b), and the second can be used for CNTs of any pattern (Figure 6.2c and d). The detailed methodology is described in

Appendix F. For future work, CNT mats can be transferred onto polymer substrates with pre-defined microcircuitry, and then patterned by (for example, oxygen plasma) etching. Alternatively, CNT pillars can be transferred with alignment to the substrate. In either case, it is important to make reliable electrical contact between the CNTs and the underlying circuits.

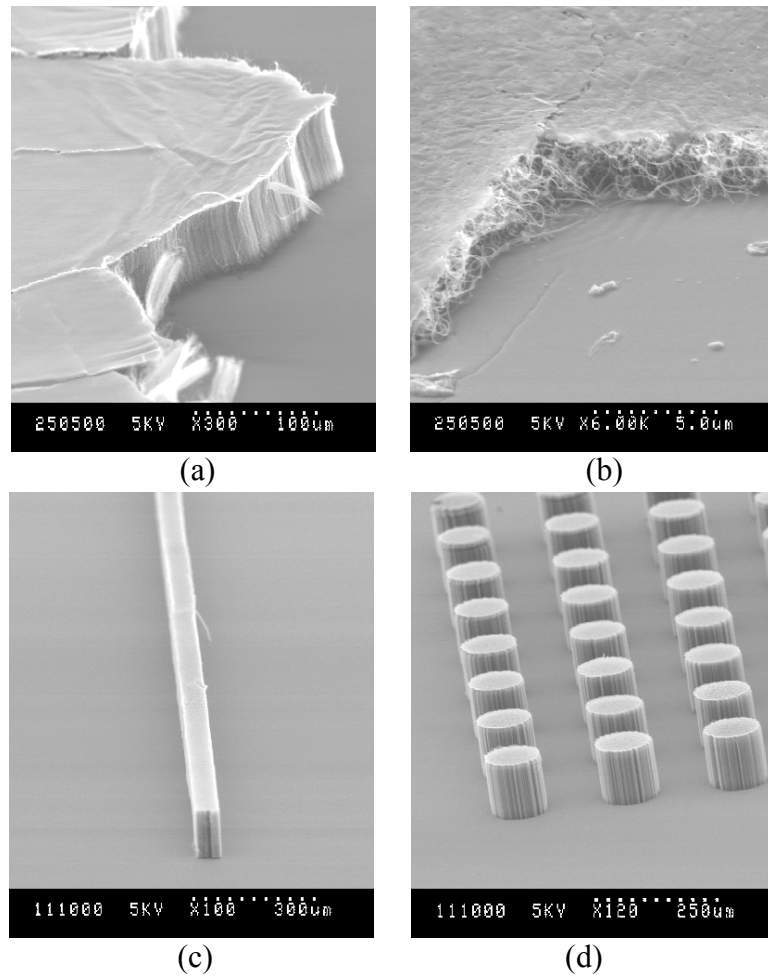


Figure 6.2 SEM images of CNTs transferred onto a thin PDMS membrane. (a) Aligned and (b) entangled CNT mats. The mats were first lifted off from the silicon substrate, and then transferred onto PDMS. (c) and (d): patterned CNT structures “stamped” onto PDMS films.

Optimization of Synthesis and Surface Modification

Charge injection ability and biocompatibility are the two most important aspects of stimulating neural electrodes. Surface modification is the key to enhance both properties of the CNT microelectrodes. To maximize the accessible surface area, the functional group needs to adhere strongly to the nanotube surface and should be smaller in size than the inter-nanotube space. The requirement for the biological properties of the surface can vary from one application to another. For implants, it may even be desirable to have the outer surface repellent to cell adhesion in order to minimize scar tissue formation. On the other hand, the diameter and density of the nanotubes in a pillar can also be optimized to maximize the active surface area. This may be achieved by better control of the catalyst particles and the synthesis process.

In vivo Biocompatibility

Although CNT substrates have been shown to be capable of supporting neuronal growth in vitro, their in vivo biocompatibility still largely remains unknown. Current in vivo tests focus on pulmonary and intravenous exposure to SWCNTs and MWCNTs dispersed in solutions [92, 93]. However, tissue response to CNTs immobilized on a substrate implanted in other parts of the body can be very different. CNT structures on thin polymers, such as those shown in Figure 6.2 can be implanted (for example, on the retina or the cortex), so that the immune response and foreign body response, such as inflammation and scar tissue formation, can be studied.

Appendix A. Fluorescein Tagging

Fluorescein (FITC) molecules binds to the primary amine group, thus can be tagged onto various proteins and the PEG-PL-NH₂ chains. The procedures are listed below, using laminin as an example. They are also applicable to other proteins.

1. Add fluorescein isothiocyanate (“FITC isomer”, MW=390) to DMSO to a concentration of 5mM. (For example, add 1 mg FITC isomer to 500 μ l DMSO.)
2. Add the FITC/DMSO mixture to 1mg/ml laminin (Invitrogen #23017-015, MW=850 kD), so that the final concentration ratio of FITC:laminin is 25:1. (For example, add 0.5 μ l FITC/DMSO to 100 μ l laminin.)
3. Wrap with aluminum foil. Let it mix well on a shaker for 2 hours at room temperature.
4. To remove unbound FITC, transfer the 100 μ l FITC-laminin mixture to a 500 μ l filtration tube (300kD pore size in this case). Add 350ul PBS.
5. Centrifuge at 10,000 rpm for 5 minutes.
6. Discard the filtered solution at the bottom of the tube (FITC+PBS). Add more PBS to the top part, and spin again for 3 minutes.
7. Repeat step 6 for several times.

Appendix B. RGC Panning Protocol

Methods are based on Barres, B.A., et al., (1988) *Neuron*, 1(9): p. 791-803; the protocol is prepared by Neville Mehenti.

Chemicals used:

N-acetyl cysteine	Sigma	A-8199
B-27 supplement (50×)	Gibco	17504-044
Bovine albumin, lyophilized	Sigma	A-4161
Bovine albumin, fatty acid free	Sigma	A-8806
Braine derived neurotrophic factor (BDNF)	Peprotech	450-02
Ciliary neurotrophic factor (CNTF)	Peprotech	450-50
L-cysteine	Sigma	C-7352
Dimethyl sulfoxide (DMSO), sterile	Sigma	D2650
DNase	Worthington	LS002007
Dulbecco's phosphate buffered saline (DPBS)	Gibco	14287-080
Earle's balanced salt solution (EBSS)	Gibco	14155-063
Fetal calf serum (FCS), heat inactivated	Gibco	10082-139
Forskolin	Sigma	F6886
L-glutamine (100×)	Gibco	25030-149
Goat anti mouse IgM	Jackson	115-005-020
Goat anti rabbit IgG	Jackson	111-005-003
Hydrochloric acid	Sigma Diag.	251-2
Insulin	Sigma	I6634
MEM sodium pyruvate (100×)	Gibco	11360-070
Neurobasal A medium	Gibco	10888-022
Papain	Worthington	LS003126
Penicillin/Streptomycin (Pen-Strep)	Gibco	15140-122
Phenol red solution, 0.5% in DPBS	Sigma	P0290
Poly-D-lysine HBr (PDL)	Sigma	P-6407
Progesterone	Sigma	P-8783

Putrescine	Sigma	P-7505
Rabbit anti-rat macrophage Ab	Accurate	A51240
Sodium hydroxide, 1N	Sigma	S2770
Sodium selenite	Sigma	S-5261
Apo-Transferrin	Sigma	T-1147
T11D7	From Dr. Barres	
Triiodothyronine	Sigma	T6397
Trizma base	Sigma	T-6791
Trypsin	Sigma	T4665
Tyrosin inhibitor	Roche	109878

Stock solutions:

Solution	Chemical	Amount	Unit	Storage (°C)
NAC (1000×)	N-acetyl cysteine	50	mg	-30
	Neurobasal A	10	ml	
BDNF (1000×)	BDNF	50	µg	-80
	0.4% BSA/DPBS	1	ml	
BSA, 4% (20×)	BSA	2	g	-30
	DPBS	50	ml	
CNTF (1000×)	CNTF	10	µg	-80
	0.4% BSA/DPBS	1	ml	
DNase soln.	DNase	12500	units	-30
	EBSS	1	ml	
Forskolin (1000×)	Forskolin	10	mg	-80
	DMSO	2.4	ml	
Hi Ovomuroid (6×)	BSA	600	mg	-30
	Trypsin inhibitor	600	mg	
	DPBS	20	ml	
Insulin (100×)	Insulin	10	mg	-30
	Sterile water	20	ml	
	1N HCl	100	µl	
Lo Ovomuroid (Lo Ovo) (10×)	BSA	600	mg	-30
	Trypsin inhibitor	600	mg	
	DPBS	40	ml	
Poly-D-lysine (PDL) (100×)	Poly-D-lysine	5	mg	-30
	Sterile water	5	ml	
Progesterone	Progesterone	2.5	mg	25
	Ethanol	100	µl	
Sato (100×)	Transferrin	400	mg	-30
	BSA	400	mg	
	Progesterone soln.	10	µl	

	Putrescine	64	mg	
	Na selenite soln.	400	μl	
	Neurobasal A	40	ml	
Sodium selenite	Sodium selenite	4	mg	25
	0.1N NaOH	100	μl	
	Neurobasal A	10	ml	
T3 (100×)	Triiogothonine	3.2	mg	-30
	0.1N NaOH	400	μl	
	DPBS			
Tris HCl (10×)	Trizma base	12.1	g	4
	Sterile water	200	ml	
Trypsin	Trypsin	30000	units	-80
	EBSS	1	ml	

Solutions used for panning:

Hi Ovo	DPBS	5ml
	Hi Ovomuroid stock	1ml
	1N NaOH	2μl
Lo Ovo	DPBS	9ml
	Lo Ovomuroid stock	1ml
	0.4% DNase stock	100μl
Lo-MΦ	Lo Ovo soln.	6ml
	Anti-macrophage serum	80μl
Papain	DPBS	10ml
	papain	165 units
	L-cystein (filter)	2mg
	0.4% DNase stock	100μl
	1N NaOH	10μl
Insulin Solution	insulin	10mg
	1N HCl	100μl
	sterile water	20ml
Panning Buffer	0.2% BSA	2ml
	DPBS	18ml
	insulin solution	200μl
Trypsin Solution	trypsin stock	200μl
	pre-equilibrated EBSS	4ml
0.2% BSA	4% BSA	2ml
	DPBS	40ml
FCS	FCS	6ml
	Neurobasal	14ml

RGC cell culture media:

Neurobasal	20 ml
Pen/Strep (100×)	200 µl
Insulin (100×)	200 µl
Sodium pyruvate (100×)	200 µl
Sato stock (100×)	200 µl
T3 (100×)	200 µl
L-glutamine (100×)	200 µl
NAC (1000×)	20 µl
B27 ((50×)	400 µl

Mix well and filter through 0.22 µm. Before use, add:

BDNF	20 µl
CNTF	20 µl
Forskolin	20 µl

Day Before

Coat panning dishes:

1. Get two 150 mm Petri dishes. Dilute 4 ml 10× Tris-HCl solution with 36 ml sterile water. Add 20 ml diluted Tris-HCl solution (50mM, pH=9.5) and 50 µl affinity purified goat anti-rabbit IgG to each of the 150 mm Petri dish.
2. Dilute 1.2 ml 10× Tris-HCl solution with 10.8 ml sterile water. Add 12 ml diluted Tris-HCl and 40 µl goat anti-mouse IgM to a 100 mm Petri dish.
3. Mark all dishes. Mix well to make sure the entire plate is covered. Incubate all three dishes at 4°C overnight.

Coat substrates (CNTs or Petri dish controls):

1. Add 200 µl PDL stock solution to 20 ml sterile water. Wash the substrates first with sterile water, and then add the diluted PDL solution.
2. Leave at room temperature for at least 30 minutes (2 hours for CNT substrates). Aspirate PDL and wash twice with sterile water.
3. Dilute 25 µl (1 mg/ml) laminin with 15 ml Neurobasal. Add to the substrates and incubate at 37°C overnight in an incubator.

Day of Preparation

I. Prepare all the solutions

1. First add 0.5 ml phenol red solution to both EBSS and DPBS 500 ml bottles.
2. Prepare all the solutions needed for panning.

3. In addition, equilibrate two tubes of EBSS at 37°C in incubator. One with 4 ml of EBSS, the other with 6 ml.

II. Finish preparing the panning dishes

1. Rinse 150 mm dishes three times with PBS. Never leave the dish dry. After rinsing, add 10 ml 0.2% BSA solution to each dish, carefully avoid bubbles. Set aside at room temperature outside the hood.
2. Rinse the small dish three times with PBS. Add 8ml of T11D7 solution. Set aside at room temperature outside the hood.

III. Harvest the retina

IV. Digestion of the retina

1. Transfer the retinas by pouring about half of pre-warmed papain solutions into the retinas and then pouring the retinas into a new empty 15 ml tube. Repeat until all retinas have been transferred, then add the remaining papain solution.
2. Turn the tube until level very slowly once. Incubate at 37C for 30min. Turn level slowly again after 15min.

V. Dissociation of the retina

1. After 30 minutes of digestion, aspirate papain solution from the tube. Add Lo Ovo solution, let it sit for 1 minute so that retinas can settle, aspirate again.
2. Add 1.5 ml of Lo-MΦ. Triturate very gently with P1000: on the first pass, very slowly suck up all retinas and then release them (do it just once). Allow remaining chunks to settle, then transfer 1.0 ml of supernatant to a new empty 15 ml tube marked “digestion”.

3. Add another 1ml of Lo-MΦ, triturate, settle, and transfer again. Repeat this four times in total. The last pass, transfer all supernatant. Trituration can be a bit more vigorous each cycle.
4. Incubate at room temperature for 10 minutes outside the hood, to allow the antibody to bind to the cells.
5. Centrifuge cells at 1000 rpm for 12 minutes.
6. Aspirate off supernatant and add Hi Ovo slowly. Triturate gently until they resuspend. Centrifuge again at 1000 rpm for 12 min. (Hi Ovo is toxic to RGCs if left too long).

VI. Panning

1. Aspirate Hi Ovo, add 1 ml Panning Buffer slowly, triturate slowing to resuspend. Then add the other 9 ml Panning buffer to bring volume up to 10 ml.
2. Remove DPBS/BSA from first 150mm dish. Add 10ml of cell suspension to dish. Locate on flat surface at room temperature outside the hood for 25-30 minutes. Shake vigorously halfway to ensure that all cells that do not bind to macrophage come off (including RGCs). At the end of the incubation, the plate should be covered with adhered cells.
3. Shake first dish vigorously again at the end of incubation. Use a 10 ml pipette, pipette out all cell suspension, empty the second dish, and add the suspension. Use P1000 to transfer all solutions. Incubate at room temperature outside for another 25-30 minutes. Shake halfway vigorously.
4. Rinse the 100 mm dish with DPBS three times, and then add the cell suspension. Incubate at room temperature outside of the hood for 45 minutes. Shake gently halfway. RGCs should be seen adhering to the panning plate.

VII. Releasing the cells

1. Take out the tubes with 4 ml and 6 ml EBSS from the incubator. Add 200 μ l trypsin stock to the 4 ml tube.
2. Wash the 100 mm panning dish 8 times with DPBS to remove all nonadherent cells.
3. Add 6ml equilibrated EBSS (from the other tube) to the 100 mm dish. Quickly swirl and discard.
4. Add 4ml trypsin solution. Set the dish outside the hood at room temperature. Incubate about 7 minutes. Check under microscope, some cells should start to come off (float when swirled gently).
5. Add 2ml FCS solution slowly to the dish.
6. Use P1000 to squirt cells off the dish. Pipette very gently toward the edge of dish, moving around the dish one revolution. Then squirt a few times at the center. Do not scrape plate with pipette and avoid bubbles
7. Transfer cells to a new empty tube.
8. Add 5ml FCS to dish, repeat releasing. Check under microscope that most of the cells have been dislodged. Transfer to the cell tube.
9. Centrifuge at 1000 rpm for 15 min.
10. Aspirate out supernatant until there is about 0.3ml left in tube. Add 0.5ml complete media, resuspend the cells.

The cells are ready for seeding.

Appendix C. Preparation of Rat Hippocampal Neurons

Primary hippocampal neurons were harvested from embryonic day 18 Sprague/Dawley rat hippocampus in Hibernate (Brainbits, LLC). Tissue can be stored in Hibernate at 4-8°C for one week. The methods are provided by Brainbits, based on *Brewer et al. (1993) J. Neurosci. Res. 35:567-576* and *Brewer & Price (1996) Neuroreport 7:1509-1512*.

Cell culture media for day 0 to day 4:

20ml	Neurobasal (Gibco, 21103-049)
200 µl	B27 (50x, Gibco, #17504-044)
200 µl	L-glutamine (100x, Gibco, #25030-149)
73.5 µg	L-glutamic acid (Sigma, #128430)

Filter sterilize. After day 4, replace with media without glutamate (only Neurobasal/B27/glutamine).

Cell preparation protocol:

1. Rat hippocampus pair arrives in a 2 ml tube containing B27/Hibernate. From the tube with the brain tissue, remove 1 ml medium and save for step 3.

2. With 1 ml pipettor with sterile blue plastic tip, suck the tissue with medium into the pipet and immediately dispense the contents back into the same container. Take care not to create bubbles. Repeat this trituration step about 10 times or until most all pieces of tissue are dispersed.
3. Add back 1 ml medium that was removed in step 1 and mix.
4. Let undispersed pieces settle by gravity for 1 min.
5. Transfer supernatant to a new sterile 15 ml tube. Spin at 1100 rpm for 1 min. Discard supernatant.
6. Flick the tube to disperse the pellet of cells. Resuspend pellet in 1 ml culture medium (with glutamate).
7. Aliquot 10 μ l and mix with 10 μ l 0.4% trypan blue. Count cells in a hemacytometer.
8. Dilute cells with culture medium to 3×10^4 cells/ml (equivalent to about 100 cells/cm²), or any other desired concentration. Plate the cells.
9. Incubate 37°C, with 5% CO₂.

After 4 days, neurons are well differentiated. If further culture is desired, change one half of the medium with fresh, warm B27/Neurobasal/glutamine without glutamate. Change one half every 3 or 4 days.

Appendix D. Loading Fluorescent Dyes

Ringer's solution:

1000ml Hank's Balanced Salt Solution (HBSS) without calcium or magnesium

0.37 g $\text{CaCl}_2 \cdot 2\text{H}_2\text{O}$

0.26 g $\text{MgCl}_2 \cdot 6\text{H}_2\text{O}$

2.38 g HEPES

Adjust pH to 7.4 with 1M NaOH

Filter sterilize. Store at 4°C.

Live/Dead (Molecular Probes, #L-3224):

1. Prepare two tubes of ringer's solution. One with the volume for loading, the other with three times as much of solution for rinsing. Warm up to 37°C.
2. To make the loading solution, add 0.5 μl calcein ("LIVE") and 2 μl EthD-1 ("DEAD") to every 1 ml of ringer. Mix well.
3. Rinse the cells once with warm ringer.
4. Add the loading solution. Incubate at room temperature outside the hood for 20 minutes in dark.

5. Rinse the cells two to three times with warm ringer.

The cells are ready for imaging.

Fluo-4 (Molecular Probes, #F-14201):

1. Fluo-4 AM ester comes in 50 µg aliquots. To make stock solution, add 50 µl DMSO to the 50 µg Fluo-4. Mix well and store at -20°C, avoid light.
2. Prepare two tubes of ringer's solution. One with the volume for loading, the other with four times as much of solution for rinsing. Warm up to 37°C.
3. Add 2 µl Fluo-4 stock solution to every 1 ml of ringer to make the loading solution. Mix well.
4. Rinse the cells once with warm ringer.
5. Add the loading solution. Incubate at room temperature outside the hood for 30 minutes in dark.
6. Rinse the cells two to three times with warm ringer. Incubate at 37°C in dark for another 30 minutes.

The cells are ready for imaging.

Appendix E. Preparing Cell Culture Samples for SEM

Biological samples (such as cells cultured on a CNT substrate) need to be fixed and completely dehydrated before SEM imaging. The sample preparation is very time-consuming, so it is highly recommended to process a large number of samples together.

1. Prepare the fixative in the following ratio: 95ml SEM fixative, plus 5ml 25% gluteraldehyde. Replace the cell culture media or recording solution with the mixed fixative. Leave the sample in the fixative for 3 hours at room temperature, or overnight at 4°C.
2. Prepare the buffer: mix sodium cacodylate buffer with DI water in 1:1 ratio. Rinse the sample three times with the buffer. For each rinse, leave the sample in the buffer for about 15 minutes.
3. Dilute 1% osmium tetroxide in sodium cacodylate buffer (1:1). Add to the sample and leave for 2 hours at room temperature.
4. Rinse three times with buffer (same as step 2).
5. Dehydrate the sample in alcohols. Soak the sample sequentially in 50%, 70%, 80%, 95% and absolute ethanol, two to three times for about 10-15 minutes for each concentration.

6. After absolute ethanol, add acetone to the sample (make sure the sample is not in a plastic container, such as a Petri dish).
7. Dry the sample in a critical point dryer.

Notes:

1. The sample can be left in the first buffer rinse (step 2), or in 70% ethanol in the fridge for as long as desired. Good chances to take a break from this long baby-sitting task!
2. Never leave the sample completely dry when switching solutions.
3. Critical point drying is a method of drying tissue without collapsing or deforming the structure of wet, fragile specimens.

Appendix F. Integrating CNTs with PDMS

PDMS spinning:

PDMS thin membranes are formed by spin coating PDMS on a silicon substrate. The substrate was coated with fluorosilane in advance to help peeling off the PDMS film.

1. Leave one bare silicon wafer with fluorosilane (100 μ l aliquot, leave lid open) in a desiccator for 90 minutes.
2. Mix well PDMS base and the curing agent at 10:1 ratio (by weight). Degas in a desiccator.
3. The viscosity of the PDMS mixture increases with time, even at room temperature. Therefore, it should be used as soon as possible (within an hour). The curing process can be slowed down by storing the mixture at 4°C.
4. Spin first at 300 rpm and pour PDMS slowly onto the treated substrate, until it is all covered. Then increase to desired spin speed. To get thinner films, PDMS can be diluted with isopropyl alcohol (1:1 volume). The spin curve is shown in Figure F-1.
5. Cure PDMS films on a hotplate at 70°C for 10-20 minutes, depending on the film thickness.
6. Cured PDMS film can be easily scraped off from the substrate with a razor blade if needed.

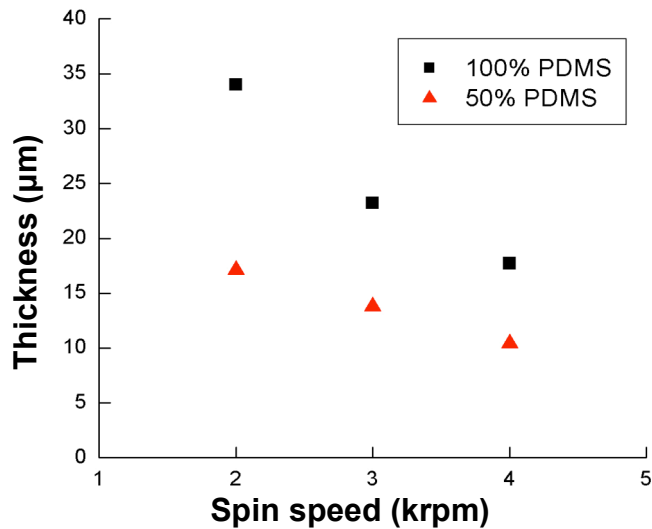


Figure F-1 PDMS spin curve.

Two methods were used for transferring CNT onto PDMS films. The first uses HF to lifting CNTs off from a silicon dioxide substrate, and then transfer free-standing CNTs onto PDMS. This method can only be used to transfer CNT mats. The other is by “stamping” CNT onto semi-cured PDMS, and can be used for CNTs with any pattern.

CNT lift-off and transfer:

1. Grow CNT mats on silicon substrates with 5000 Å silicon dioxide layer.
2. Dip the CNT sample in ethanol to wet the surface.
3. Prepare 1% HF/10% ethanol/89% water. Hold the CNT sample with a Teflon tweezer and dip it in for 2-3 minutes.
4. Carefully lower the CNT chip with an angle into a clean water bath. The CNT film is lifted off from the silicon substrate and float on the water.
5. Spoon the CNT film to a second water bath. Pick it up with a PDMS coated silicon chip. Take care to keep the CNT film flat.

6. Dry the sample in an oven at 100°C. CNT mats adhere strongly to polymer after drying. PDMS can then be scraped off from the silicon substrate.

CNT “stamping”:

1. Grow patterned or unpatterned CNTs on silicon substrates (do not use silicon dioxide layer). The taller the CNTs, the better the transfer.
2. Glue the back side of the chip onto a Z-axis micromanipulator. The CNT side faces downwards.
3. Half cure a thin PDMS film ($\sim 20 \mu\text{m}$) on a hotplate. Lower the micrometer until the CNTs are just in touch with the PDMS surface. Keep this distance and fully cure the PDMS.
4. Lift the micromanipulator. CNTs are transferred onto the PDMS film with their original patterns.

References

1. Agnew, W. and D.B. McCreery, eds. *Neural Prostheses: Fundamental Studies*. Biophysics and Bioengineering Series, Prentice Hall: New Jersey.
2. Wilson, B.S., et al., *Cochlear implants: Some likely next steps*. Annual Review of Biomedical Engineering, 2003. **5**: p. 207-249.
3. Weiland, J.D., W. Liu, and M.S. Humayun, *Retinal prosthesis*. Annu Rev Biomed Eng, 2005. **7**: p. 361-401.
4. Navarro, X., et al., *A critical review of interfaces with the peripheral nervous system for the control of neuroprostheses and hybrid bionic systems*. J Peripher Nerv Syst, 2005. **10**(3): p. 229-58.
5. Benabid, A.L., *Deep brain stimulation for Parkinson's disease*. Current Opinion in Neurobiology, 2003. **13**(6): p. 696-706.
6. Santos, A., et al., *Preservation of the inner retina in retinitis pigmentosa. A morphometric analysis*. Arch Ophthalmol, 1997. **115**(4): p. 511-5.
7. Brindley, G.S. and W.S. Lewin, *The sensations produced by electrical stimulation of the visual cortex*. J Physiol, 1968. **196**(2): p. 479-93.
8. Dobbelle, W.H., M.G. Mladejovsky, and J.P. Girvin, *Artificial vision for the blind: electrical stimulation of visual cortex offers hope for a functional prosthesis*. Science, 1974. **183**(4233): p. 440-4.

9. McCreery, D.B., et al., *Charge density and charge per phase as cofactors in neural injury induced by electrical stimulation*. IEEE Trans Biomed Eng, 1990. **37**(10): p. 996-1001.
10. Rose, T.L. and L.S. Robblee, *Electrical stimulation with Pt electrodes. VIII. Electrochemically safe charge injection limits with 0.2 ms pulses*. IEEE Trans Biomed Eng, 1990. **37**(11): p. 1118-20.
11. Brummer, S.B., L.S. Robblee, and F.T. Hambrecht, *Criteria for selecting electrodes for electrical stimulation: theoretical and practical considerations*. Ann N Y Acad Sci, 1983. **405**: p. 159-71.
12. Cogan, S.F., et al., *Over-pulsing degrades activated iridium oxide films used for intracortical neural stimulation*. J Neurosci Methods, 2004. **137**(2): p. 141-50.
13. Rose, T.L., E.M. Kelliher, and L.S. Robblee, *Assessment of capacitor electrodes for intracortical neural stimulation*. J Neurosci Methods, 1985. **12**(3): p. 181-93.
14. Fromherz, P. and A. Stett, *Silicon-Neuron Junction: Capacitive Stimulation of an Individual Neuron on a Silicon Chip*. Physical Review Letters, 1995. **75**(8): p. 1670-1673.
15. IJIMA, S., *Helical microtubules of graphitic carbon*. Nature, 1991. **354**(6348): p. 56-8.
16. IJIMA, S. and T. ICHIHASHI, *Single-shell carbon nanotubes of 1-nm diameter*. Nature, 1993. **363**(6430): p. 603-15.
17. Krishnan, A., et al., *Young's modulus of single-walled nanotubes*. Physical Review B (Condensed Matter), 1998. **58**(20): p. 14013-19.
18. Falvo, M.R., et al., *Bending and buckling of carbon nanotubes under large strain*. Nature, 1997. **389**(6651): p. 582-4.

19. Iijima, S., et al., *Structural flexibility of carbon nanotubes*. Journal of Chemical Physics, 1996. **104**(5): p. 2089-92.
20. Kam, N.W., et al., *Carbon nanotubes as multifunctional biological transporters and near-infrared agents for selective cancer cell destruction*. Proc Natl Acad Sci U S A, 2005. **102**(33): p. 11600-5.
21. Zrenner, E., *Will retinal implants restore vision?* Science, 2002. **295**(5557): p. 1022-5.
22. Palanker, D., et al., *Migration of retinal cells through a perforated membrane: implications for a high-resolution prosthesis*. Invest Ophthalmol Vis Sci, 2004. **45**(9): p. 3266-70.
23. Mehenti, N.Z., Tsien, G. S., Leng, T., Fishman, H.A., Bent, S. F., *A model retinal interface based on directed neuronal growth for single cell stimulation*. Biomedical Microdevices.
24. GUO, T., et al., *Catalytic growth of single-walled nanotubes by laser vaporization*. Chemical Physics Letters, 1995. **243**(1/2): p. 49-54.
25. Fan, S., et al., *Self-oriented regular arrays of carbon nanotubes and their field emission properties*. Science, 1999. **283**(5401): p. 512-4.
26. Sohn, J. and Y.H. Yoon, *Iron-induced cytotoxicity in cultured rat retinal neurons*. Korean J Ophthalmol, 1998. **12**(2): p. 77-84.
27. Rouault, T.A., *Iron on the brain*. Nat Genet, 2001. **28**(4): p. 299-300.
28. Sakurai, T. and K. Tamaru, *Simple formulas for two- and three- dimensional capacitances*. IEEE Trans. on Electron Devices, 1983. **ED-30**: p. 183-185.
29. de Pablo, P.J., et al., *A simple, reliable technique for making electrical contact to multiwalled carbon nanotubes*. Applied Physics Letters, 1999. **74**(2): p. 323-5.

30. Li, J., et al., *Electronic properties of multiwalled carbon nanotubes in an embedded vertical array*. Applied Physics Letters, 2002. **81**(5): p. 910-912.
31. Martel, R., et al., *Single- and multi-wall carbon nanotube field-effect transistors*. Applied Physics Letters, 1998. **73**(17): p. 2447-9.
32. Bard, A.J. and L.R. Faulkner, *Electrochemical Methods: Fundamentals and Applications, 2nd ed.* 2004: John Wiley & Sons, Inc.
33. Bockris, J.O.M. and A.K.N. Reddy, *Modern Electrochemistry*. Vol. 2. 1970, New York: Plenum.
34. Kinoshita, K., *Carbon: Electrochemical and Physicochemical Properties*. 1988: John Wiley & Sons, Inc.
35. RANDIN, J.P. and E. YEAGER, *Differential capacitance study of stress-annealed pyrolytic graphite electrodes*. Journal of the Electrochemical Society, 1971. **118**(5): p. 711-14.
36. RANDIN, J.P. and E. YEAGER, *DIFFERENTIAL CAPACITANCE STUDY ON BASAL PLANE OF STRESS-ANNEALED PYROLYTIC-GRAPHITE*. Journal of Electroanalytical Chemistry, 1972. **36**(2): p. 257-&.
37. Kovacs, G.T.A., *Introduction to the Theory, Design, and Modeling of Thin-Film Microelectrodes for Neural Interfaces*, in *Enabling Technologies for Cultured Neural Networks*, T.M. McKenna, Editor. 1994, Academic Press.
38. Newman, J., *Resistance for flow of current to a disk*. Journal of Electrochemical Society, 1966. **113**(5): p. 501-502.
39. Robblee, L.S. and T.L. Rose, *Electrochemical guidelines for selection of protocols and electrode materials for neural stimulation*, in *Neural Prostheses: fundamental studies*, McCreery, Editor, Prentice Hall.

40. Brummer, S.B. and M.J. Turner, *Electrochemical considerations for safe electrical stimulation of the nervous system with platinum electrodes*. IEEE Trans Biomed Eng, 1977. **24**(1): p. 59-63.
41. Barisci, J.N., G.G. Wallace, and R.H. Baughman, *Electrochemical studies of single-wall carbon nanotubes in aqueous solutions*. Journal of Electroanalytical Chemistry, 2000. **488**(2): p. 92-98.
42. Frackowiak, E. and F. Beguin, *Electrochemical storage of energy in carbon nanotubes and nanostructured carbons*. Carbon, 2002. **40**(10): p. 1775-87.
43. An, K.H., et al., *Supercapacitors using single-walled carbon nanotube electrodes*. Advanced Materials, 2001. **13**(7): p. 497-+.
44. Gao, B., et al., *Enhanced saturation lithium composition in ball-milled single-walled carbon nanotubes*. Chemical Physics Letters, 2000. **327**(1/2): p. 69-75.
45. Cheng, H.M., Q.H. Yang, and C. Liu, *Hydrogen storage in carbon nanotubes*. Carbon, 2001. **39**(10): p. 1447-1454.
46. Lin, T., et al., *Chemistry of carbon nanotubes*. Australian Journal of Chemistry, 2003. **56**(7): p. 635-651.
47. Kam, N.W., Z. Liu, and H. Dai, *Functionalization of carbon nanotubes via cleavable disulfide bonds for efficient intracellular delivery of siRNA and potent gene silencing*. J Am Chem Soc, 2005. **127**(36): p. 12492-3.
48. Kong, J. and H.J. Dai, *Full and modulated chemical gating of individual carbon nanotubes by organic amine compounds*. Journal of Physical Chemistry B, 2001. **105**(15): p. 2890-2893.
49. Chmiola, J., et al., *Double-layer capacitance of carbide derived carbons in sulfuric acid*. Electrochemical and Solid-State Letters, 2005. **8**(7): p. A357-60.

50. Jensen, R.J., et al., *Thresholds for activation of rabbit retinal ganglion cells with an ultrafine, extracellular microelectrode*. Invest Ophthalmol Vis Sci, 2003. **44**(8): p. 3533-43.
51. Jensen, R.J., O.R. Ziv, and J.F. Rizzo, 3rd, *Thresholds for activation of rabbit retinal ganglion cells with relatively large, extracellular microelectrodes*. Invest Ophthalmol Vis Sci, 2005. **46**(4): p. 1486-96.
52. Kam, N.W. and H. Dai, *Carbon nanotubes as intracellular protein transporters: generality and biological functionality*. J Am Chem Soc, 2005. **127**(16): p. 6021-6.
53. Shi Kam, N.W., et al., *Nanotube molecular transporters: internalization of carbon nanotube-protein conjugates into Mammalian cells*. J Am Chem Soc, 2004. **126**(22): p. 6850-1.
54. Fiorito, S., et al., *Toxicity and biocompatibility of carbon nanoparticles*. J Nanosci Nanotechnol, 2006. **6**(3): p. 591-9.
55. Ni, Y., et al., *Chemically functionalized water soluble single-walled carbon nanotubes modulate neurite outgrowth*. J Nanosci Nanotechnol, 2005. **5**(10): p. 1707-12.
56. Cui, D., et al., *Effect of single wall carbon nanotubes on human HEK293 cells*. Toxicol Lett, 2005. **155**(1): p. 73-85.
57. Jia, G., et al., *Cytotoxicity of carbon nanomaterials: single-wall nanotube, multi-wall nanotube, and fullerene*. Environ Sci Technol, 2005. **39**(5): p. 1378-83.
58. Nimmagadda, A., et al., *Chemical modification of SWNT alters in vitro cell-SWNT interactions*. J Biomed Mater Res A, 2006. **76**(3): p. 614-25.
59. Mattson, M.P., R.C. Haddon, and A.M. Rao, *Molecular functionalization of carbon nanotubes and use as substrates for neuronal growth*. J Mol Neurosci, 2000. **14**(3): p. 175-82.

60. Lovat, V., et al., *Carbon nanotube substrates boost neuronal electrical signaling*. Nano Lett, 2005. **5**(6): p. 1107-10.
61. Stenger, D.A. and T.M. McKenna, *Enabling technologies for cultured neural networks*. 1994: Academic Press.
62. Arnold, L.J., Jr., et al., *Antineoplastic activity of poly(L-lysine) with some ascites tumor cells*. Proc Natl Acad Sci U S A, 1979. **76**(7): p. 3246-50.
63. Bacakova, L., et al., *Cell adhesion on artificial materials for tissue engineering*. Physiol Res, 2004. **53 Suppl 1**: p. S35-45.
64. Kleinfeld, D., K.H. Kahler, and P.E. Hockberger, *Controlled outgrowth of dissociated neurons on patterned substrates*. J Neurosci, 1988. **8**(11): p. 4098-120.
65. Barres, B.A., et al., *Immunological, morphological, and electrophysiological variation among retinal ganglion cells purified by panning*. Neuron, 1988. **1**(9): p. 791-803.
66. Peterman, M.C., et al., *The Artificial Synapse Chip: a flexible retinal interface based on directed retinal cell growth and neurotransmitter stimulation*. Artif Organs, 2003. **27**(11): p. 975-85.
67. Brewer, G.J. and P.J. Price, *Viable cultured neurons in ambient carbon dioxide and hibernation storage for a month*. Neuroreport, 1996. **7**(9): p. 1509-12.
68. Brewer, G.J., et al., *Optimized survival of hippocampal neurons in B27-supplemented Neurobasal, a new serum-free medium combination*. J Neurosci Res, 1993. **35**(5): p. 567-76.
69. Bergstrom, K., et al., *Reduction of fibrinogen adsorption on PEG-coated polystyrene surfaces*. J Biomed Mater Res, 1992. **26**(6): p. 779-90.
70. Nicholls, J.G., et al., *From neuron to brain*. 4th ed. 2001, Sunderland: Sinauer Associates, Inc.

71. Hille, B., *Ionic channels of excitable membranes*. 1992.
72. Hodgkin, A.L. and A.F. Huxley, *A quantitative description of membrane current and its application to conduction and excitation in nerve*. J Physiol, 1952. **117**(4): p. 500-44.
73. Hodgkin, A.L. and A.F. Huxley, *The dual effect of membrane potential on sodium conductance in the giant axon of Loligo*. J Physiol, 1952. **116**(4): p. 497-506.
74. Hodgkin, A.L. and A.F. Huxley, *The components of membrane conductance in the giant axon of Loligo*. J Physiol, 1952. **116**(4): p. 473-96.
75. Hodgkin, A.L. and A.F. Huxley, *Currents carried by sodium and potassium ions through the membrane of the giant axon of Loligo*. J Physiol, 1952. **116**(4): p. 449-72.
76. Hodgkin, A.L., A.F. Huxley, and B. Katz, *Measurement of current-voltage relations in the membrane of the giant axon of Loligo*. J Physiol, 1952. **116**(4): p. 424-48.
77. Krassowska, W. and J.C. Neu, *Response of a single cell to an external electric field*. Biophys J, 1994. **66**(6): p. 1768-76.
78. Cartee, L.A. and R. Plonsey, *The transient subthreshold response of spherical and cylindrical cell models to extracellular stimulation*. IEEE Trans Biomed Eng, 1992. **39**(1): p. 76-85.
79. Lee, D.C. and W.M. Grill, *Polarization of a spherical cell in a nonuniform extracellular electric field*. Ann Biomed Eng, 2005. **33**(5): p. 603-15.
80. Invitrogen, *Voltage sensor probes user guide*.
81. Minta, A., J.P. Kao, and R.Y. Tsien, *Fluorescent indicators for cytosolic calcium based on rhodamine and fluorescein chromophores*. J Biol Chem, 1989. **264**(14): p. 8171-8.
82. Smetters, D., A. Majewska, and R. Yuste, *Detecting action potentials in neuronal populations with calcium imaging*. Methods, 1999. **18**(2): p. 215-21.

83. Rothstein, J.D., et al., *Knockout of glutamate transporters reveals a major role for astroglial transport in excitotoxicity and clearance of glutamate*. *Neuron*, 1996. **16**(3): p. 675-86.
84. Palanker, D., *Personal communication*. 2006.
85. Aidley, D.J., *The physiology of excitable cells*. 4th ed. 1998: Cambridge University Press.
86. Mortimer, J.T., *Motor Prostheses*, in *Handbook of Physiology, Section 1: The Nervous System. Motor Control Part I*. 1981. p. 155-87.
87. Lau, K.K.S., et al., *Superhydrophobic carbon nanotube forests*. *Nano Letters*, 2003. **3**(12): p. 1701-5.
88. Ng, J.M.K., et al., *Components for integrated poly(dimethylsiloxane) microfluidic systems*. *Electrophoresis*, 2002. **23**(20): p. 3461-73.
89. BOPPART, S.A., B.C. WHEELER, and C.S. WALLACE, *A flexible perforated microelectrode array for extended neural recordings*. *IEEE Transactions on Biomedical Engineering*, 1992. **39**(1): p. 37-42.
90. Gonzalez, C. and M. Rodriguez, *A flexible perforated microelectrode array probe for action potential recording in nerve and muscle tissues*. *Journal of Neuroscience Methods*, 1997. **72**(2): p. 189-95.
91. Hofmann, S., et al., *Low-temperature growth of carbon nanotubes by plasma-enhanced chemical vapor deposition*. *Applied Physics Letters*, 2003. **83**(1): p. 135-7.
92. Lam, C.-W., et al., *Pulmonary Toxicity of Single-Wall Carbon Nanotubes in Mice 7 and 90 Days After Intratracheal Instillation*. *Toxicol. Sci.*, 2004. **77**(1): p. 126-134.
93. Singh, R., et al., *Tissue biodistribution and blood clearance rates of intravenously administered carbon nanotube radiotracers*. *Proc Natl Acad Sci U S A*, 2006. **103**(9): p. 3357-62.